ALICJA STANISŁAWSKA

ADVANCED CHARACTERIZATION OF ENGINEERING MATERIALS USING INDENTATION TECHNIQUES

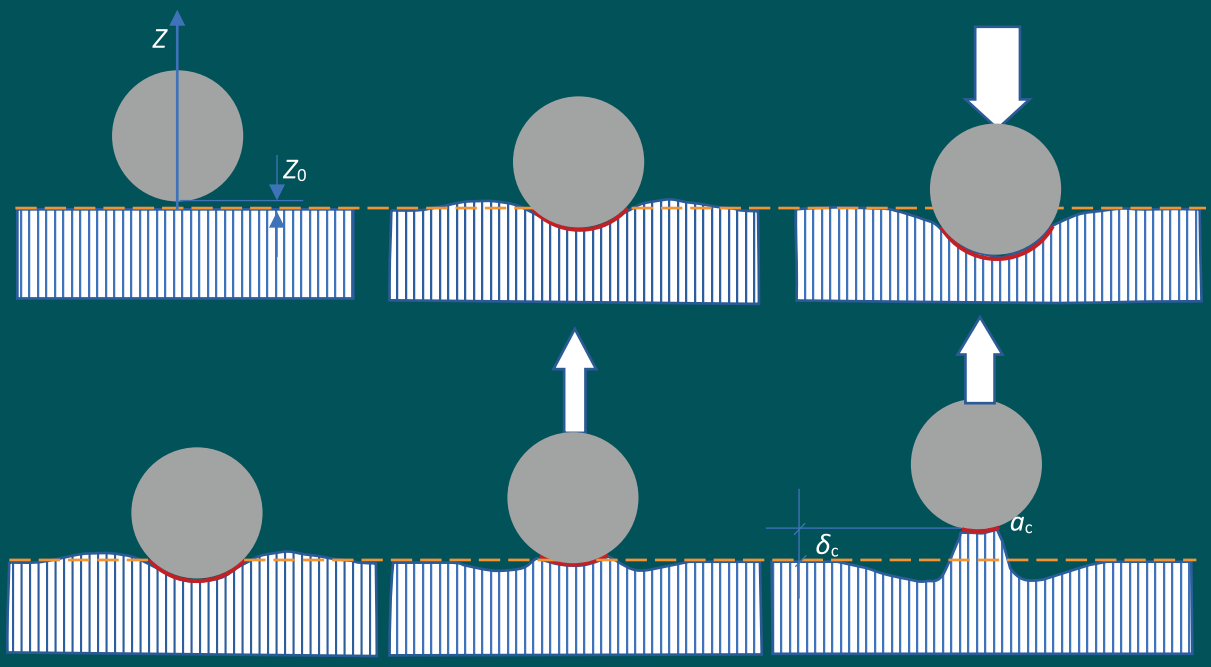

Gdańsk University of Technology Publishing House

GDAŃSK UNIVERSITY OF TECHNOLOGY PUBLISHERS
CHAIRMAN OF EDITORIAL BOARD
Dariusz Mikielewicz

EDITOR OF SCIENTIFIC PUBLICATIONS
Michał Szydłowski

REVIEWERS
Maciej Motyka
Paweł Pyrzanowski

LAYOUT AND COVER DESIGN
Wioleta Lipska-Kamińska

Published under the permission
of the Rector of Gdańsk University of Technology

Gdańsk University of Technology publications may be purchased at
https://sklep.pg.edu.pl.

ISBN 978-83-7348-938-7

Gdańsk University of Technology Publishing House

Edition I. Ark. ed. 9,79, ark. print 6,0, 292/1273

Contents

List of Important Symbols

a – contact radius or geometric dimension
a_c – contact radius considering adhesion forces
a_{pz} – radius of the plastic zone
$\bar{a}$ – contact radius between the sphere and substrate considering adhesion forces
A – contact area between the bodies or the plastically deformed impression area, or the cross-sectional area of the scratch path in the scratch test
A_a – total expected contact area or actual contact area
A_p – impression area projected onto the material surface
A_s – lateral surface area of the indenter corresponding to its maximum displacement
$\bar{A}$ – contact area between the sphere and substrate considering adhesion forces
b – Burgers vector magnitude
c – crack length in glass or geometric dimension
C – constraint factor
C_e, C_p – constants depending on the material and indenter shape
d – diameter of the spherical cap of the impression
D – diameter of the spherical indenter
$erfc(z)$ – complementary error function
E – stiffness, longitudinal elastic modulus
E', E^*, E_r – reduced longitudinal elastic modulus
f – coefficient defining the ratio of the radius of the plastic zone to the contact radius
$F_n(h)$ – statistical function fitting the Gaussian distribution of irregularities
$F_n(\lambda)$ – statistical function fitting roughness distribution to Gaussian distribution
G – shear modulus
G^* – complex shear modulus
G' – real component of the complex shear modulus
G'' – imaginary component of the complex shear modulus
h – normalized distance between planes or indenter displacement, or the height of the pile-up ridge
h_0 – distance at which stresses occur due to the Lennard-Jones potential, or maximum indenter displacement
h_a – depth at which the indenter has lost contact with the material
h_c – contact depth corresponding to the contact radius
h_i – initial indenter penetration at load Pi
h_i' – initial indenter penetration obtained by extrapolation
h_{max} – maximum indenter displacement
h_r – residual depth of the impression at its axis after unloading
h_x – additional indenter displacement depth
h' – root mean square deviation from the mean line of the rough surface
$h(c)$ – distance between contacting bodies
$h(c)^D$ – distance between contacting bodies considering Dugdale stresses
$h(c)^H$ – distance between contacting bodies according to Hertz
H – hardness
H_0 – macroscopic hardness

H_{fr} – hardness due to lattice friction
H_{ISE} – hardness with scale effect
H_{ss} – hardness due to solid solution strengthening
k – constant in Meyer's equation or calibration coefficient, or spring constant
$K_v(z)$ – modified Bessel function of the second kind
l – geometric dimension
L_0 – indenter load causing its displacement h_c in glass without residual stresses
L_c – critical load in the scratch test causing coating delamination
L_t – indenter load causing its displacement h_c in glass with residual stresses
m – coefficient equal to a/c or a constant depending on the material and indenter shape
M – Taylor coefficient
n – expected number of contacts between the rough surface and flat surface, or constant in Meyer's equation, or calibration coefficient, or number of radial cracks
N – number of irregularities on the surface
p – pressure exerted by a spherical indenter
p_0 – pressure in the symmetry axis of the system
p_{av} – average pressure
p_m – mean pressure exerted by the indenter
$p(r)$ – pressure distribution profile
$p(r)^H$ – pressure distribution profile according to Hertz
$p(r)^D$ – pressure distribution profile due to Dugdale stresses
P – indenter load or indenter load causing cracks of length c in glass without residual stresses
P_c – force needed to overcome adhesion forces or critical load at which the transition between elastic and plastic deformation occurs
P_i – minimum indenter load in the initial loading phase
P_t – load greater than the critical load P_c
P^* – load causing cracks of length c in glass with residual stresses
$\overline{P}$ – area of the sphere considering adhesion forces
R – radius of the spherical indenter or radius of curvature of the apex of an irregularity, or radius of curvature of the apex of a sharp indenter
R^2 – Pearson correlation coefficient
R_e – material yield strength
S – contact stiffness
t – time or coating thickness
$u(r)$ – deflection profile
Up – plastic deformation energy of the material in the indentation test
Us – elastic deformation energy of the material in the indentation test
Ut – total deformation energy of the material in the indentation test
V – volume of the material
w_{el} – elastic deformation energy per unit volume
W – work done on the loss of adhesion between the coating and substrate
W_{el} – total elastic deformation energy
x – strain hardening coefficient
z – height of surface roughness
z_0 – distance between the indenter and substrate where adhesion forces act
α – coefficient accounting for adhesion forces, or half-apex angle of a sharp indenter, or parameter describing the effect of roughness on the indentation test results, or coefficient dependent on dislocation structure
α' – half-apex angle of the impression after unloading
β – average radius of peaks of contacting rough surfaces or angle between the indenter and material surface
γ – surface energy per unit contact area
δ – displacement of the spherical indenter
δ_c – critical penetration depth at the failure of the adhesive bond
$\overline{\delta}$ – displacement of the sphere into the substrate considering adhesion forces
$\Delta\gamma$ – work required to overcome adhesion forces
ε – strain or constant dependent on the indenter shape in the Oliver-Pharr method

$\dot{\bar{\varepsilon}}$ – creep rate
η – surface density of roughness irregularities or viscosity
η^* – complex viscosity
η' – real component of complex viscosity
η'' – imaginary component of complex viscosity
θ – angle between the indenter and material surface
λ – coefficient accounting for adhesion forces, or Stribeck oil film parameter, or damping coefficient
μ – Tabor's parameter
μ_c – coefficient of friction between the indenter and substrate in the scratch test
ν – Poisson's ratio
ρ_{GDN} – density of geometrically necessary dislocations
ρ_{SSD} – dislocation density in the material
σ – standard deviation of surface roughness distribution
σ_0 – maximum stress resulting from the Lennard-Jones potential
σ_F – flow stress
σ_R – residual stress
σ_s – maximum height of surface roughness
σ_{th} – theoretical stress resulting from the Lennard-Jones potential
υ – average dislocation velocity
φ – phase shift between force and displacement
$\Phi(z)dz$ – probability that the height of irregularities falls within a given range $<z, z+dz>$
$\Phi^*(s)$ – normalized distribution of irregularities following the Gaussian distribution
χ – constant dependent on the indenter shape
Ψ – index describing elastoplastic deformations in the contact of irregularities
ω – frequency

1. Introduction

Over the centuries, the development of human civilization has been closely associated with the search for increasingly better materials that could win battles, enhance the quality of life, or enable the exploration of previously unknown regions. However, it is only since the beginning of the last century that we have observed rapid advancements in this area, driven by the production of new materials and the refinement of manufacturing techniques for existing ones. This rapid progress in new materials has also necessitated the development of research methods that allow for increasingly in-depth studies of the properties of newly developed, manufactured, and processed materials. A hundred years ago, tensile testing or hardness measurement sufficed to characterize the mechanical properties of materials. These methods are still in use today; however, the ever-increasing demands placed on new materials by designers have driven the need for novel research methods that enable more precise and detailed determination of their mechanical properties. Current requirements also extend to determining mechanical properties not only on a macro scale but also—due to the development of nanomaterials and techniques related to the deposition of thin layers and coatings—on a micro- and nanometric scale. It may seem that these issues pertain only to precision electronic systems, but even engineers designing much larger structures, such as bridges, want to know the properties of cement mortar in the zone adjacent to the aggregate, which spans an area several tens of micrometers wide, as the mechanical properties of this zone determine the mechanical properties of the entire concrete structure. Knowledge of the properties of materials used in various types of engineering constructions is essential for the proper selection of these materials by designers and technologists. One of the modern techniques for determining the mechanical properties of various groups of engineering materials is the indentation method, which involves pressing a diamond indenter into the material being tested. The method for determining the mechanical properties of materials based on the indentation test allows for the determination of many useful mechanical properties of materials belonging to various groups of engineering materials. It can be used to determine material properties on a macro-, micro-, and nanoscopic scale. For example, it allows for the determination of material hardness and stiffness (Young's modulus), and in the case of brittle materials, such as ceramics or hard metals and alloys, it enables the determination of the critical stress intensity factor. Using this method, it is possible to determine not only the values of residual stresses of the first, second, and third types in metals and alloys but also their nature (sign). The indentation test also enables the study of creep rates in various materials and the determination of dislocation density in metallic materials and their mobility. These material properties can be investigated under both static and dynamic loading conditions. The theoretical foundations for the indentation test using a spherical indenter were first formulated by Heinrich Hertz at the end of the nineteenth century [1, 2], and in subsequent research, they were further developed for a conical indenter by the Scottish mathematician Ian Naismith Sneddon [3, 4].

This edition represents the second version of the original Polish edition, revised and expanded to include additional updates and improvements.

2. Objective of the Study

As mentioned in the introduction, the method of characterizing materials through indentation testing allows the determination of many mechanical properties that are valuable to engineers across various material groups. This method can be used to assess the mechanical properties of metals and their alloys, polymeric and ceramic materials, as well as composite materials. The versatility of this method for material characterization has led to its increasing use in material property research. In literature, indentation testing is often compared to fingerprint analysis, which enables the identification of a criminal; similarly, the impression left in a material after an indentation test allows for the identification of the material under investigation, much like a fingerprint identifies a specific individual. Despite its wide applicability, the relatively high cost of testing equipment limits the ability to perform such studies in many research centers. Furthermore, even in research institutions equipped to conduct this type of material testing, the full potential of the indentation test is not always fully utilized.

The primary objective of this work is to deepen and systematize knowledge regarding the theoretical foundations associated with the characterization of engineering materials using contact mechanics methods. Given that few domestic publications provide examples of using the indentation method to characterize the mechanical properties of various material groups, **the secondary objective of this monograph is to present the potential applications of the indentation test in characterizing newly developed engineering materials or known materials processed in novel, unprecedented ways**. The author, having some experience in characterizing different groups of engineering materials, presents the results of her work, as well as the work of other authors, to acquaint readers with the practical applications of the results obtained from indentation testing, with the aim of facilitating their successful publication in scientific journals worldwide.

3. The Theoretical Foundations of Contact Mechanics

3.1. Hertz Model for a Spherical Indenter Pressed into a Flat Sample

Understanding the phenomenon of indentation begins with the study of contact mechanics between solid bodies. The most well-known system is that of a spherical indenter pressed into a flat sample. The contact and stress between two elastic spheres pressed against each other with a force P were first described by Hertz. The results, initially obtained in 1880 and published in 1882 [1], concerned the contact of two spheres with different radii. If the radius of one of the spheres tends toward infinity, its surface can be considered flat. Hertz described the localized elastic stresses that arise between two rigid spheres with radii *R1* and *R2* and elastic moduli *E1* and *E2*. Hertz's contact theory describes the stress in the contact area as a function of the applied normal force, the curvature radii of the two bodies, and their elastic moduli. The magnitude of the elastic deformation, in turn, depends on the stiffness of the spheres being pressed together. In deriving solutions to contact problems, Hertz made the following assumptions:

- The stresses are small and within the elastic limit.
- The surfaces are continuous and non-conforming (meaning the contact area is much smaller than the characteristic dimensions of the contacting bodies).
- Each body can be treated as an elastic half-space.
- The surfaces are frictionless.

When considering the situation where a rigid sphere is pressed into a flat elastic body (a scenario in which one of the spheres has an infinite radius), the displacement of the sphere into the elastic material increases with the applied compressive force, as is typical in any elastic deformation scenario. However, in the case of Hertzian contact, there are two important factors characteristic of this theory. First, the initial contact between the two bodies is point-like, and the contact area increases as the compressive force increases. The contact radius a between the sphere and the surface (Fig. 3.1) represents the radius of a spherical cap with a depth δ and is approximately geometrically related to the sphere's radius R by the following relationship:

$$a^2 \approx R \cdot \delta \tag{3.1}$$

The second peculiarity of Hertz's theory is that, despite deformations within the elastic range, there is no linear relationship between the load P and the indentation depth δ of the sphere into the substrate. The relationship between force and displacement is given by:

$$P \propto \delta^{3/2} \tag{3.2}$$

The reason for the nonlinear relationship between the load and the displacement of the sphere, expressed as the depth of the spherical cap, is precisely that, as the load increases, the contact area between the sphere and the surface also increases. There is also no linear relationship between the load and the contact radius. This relationship is described as follows:

$$a \propto P^{1/3} \tag{3.3}$$

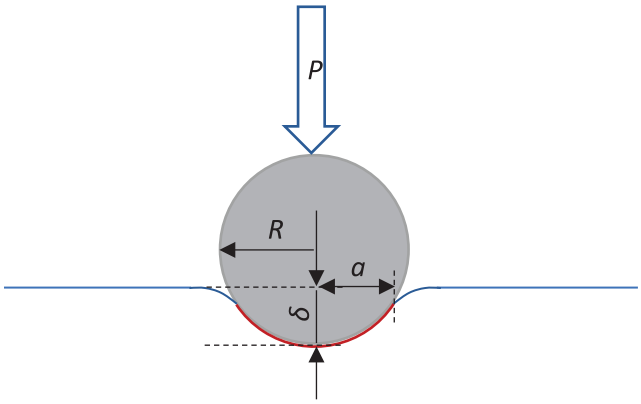

Fig. 3.1. Schematic of elastic surface deformation under the compression of a rigid sphere.
The figure does not represent the actual R/a proportion; a – contact radius between the sphere and the surface;
δ – maximum depth of sphere penetration into the material

Source: Own work based on [1].

In the case of a sphere and a flat surface, the contact area takes the shape of a circle, and for the indentation of an infinitely rigid sphere into a flat sample, it is always equal to πa^2.

The relationships presented in equations (3.1), (3.2), and (3.3) can be relatively easily estimated through the analysis of the elastic deformation energy of the substrate in the following manner. The elastic strain of the substrate is given by $\varepsilon = \delta/a$, and the volume of the material in which these deformations occur is approximately $V \approx a^3$. The elastic deformation energy of the substrate per unit volume (elastic strain energy density) is given by:

$$w_{\mathrm{el}} = \frac{1}{2} E \varepsilon^2 \approx E \left(\frac{\delta}{a}\right)^2 \tag{3.4}$$

where E is the Young's modulus of the substrate material. The total elastic deformation energy of the substrate is obtained by integrating equation (3.4). The result of the integration is of the order of the product of the maximum elastic strain energy density and the elastically deformed volume of the substrate material:

$$W_{\mathrm{el}} \approx w_{\mathrm{el}} \cdot V \approx E \left(\frac{\delta}{a}\right)^2 \cdot a^3 \approx Ea\delta^2 \tag{3.5}$$

Combining the obtained result with the geometric relationship (3.1), we arrive at:

$$W_{\mathrm{el}} \approx Ea\delta^2 \approx E\frac{a^5}{R^2} \approx ER^{\frac{1}{2}}\delta^{\frac{5}{2}} \tag{3.6}$$

To estimate the relationship between the force P and the displacement δ, as well as the contact radius a, the elastic deformation energy W_{el} should be differentiated with respect to the displacement δ; this yields:

$$P \approx ER^{\frac{1}{2}}\delta^{\frac{3}{2}} \tag{3.7}$$

From equation (3.7), the displacement δ and the contact radius a can be estimated by using the geometric relationship (3.1):

$$\delta = \left(\frac{P^2}{E^2 R}\right)^{\frac{1}{3}} \tag{3.8}$$

$$a \approx \left(\frac{PR}{E}\right)^{\frac{1}{3}} \tag{3.9}$$

Equation (3.8) confirms the relationship between force and displacement presented in equation (3.2), while equation (3.9) confirms the relationship between the contact radius and force as presented in equation (3.3).

In his work [2], Hertz provided an exact relationship between the contact radius and the applied force. Hertz's work involved finding the appropriate pressure profile to achieve a deflection profile $u(r)$ of the plane that matches the contact zone with a sphere of radius R and the displacement of the sphere into the substrate δ ($u(0) = \delta$) or the contact radius a (Fig. 3.2).

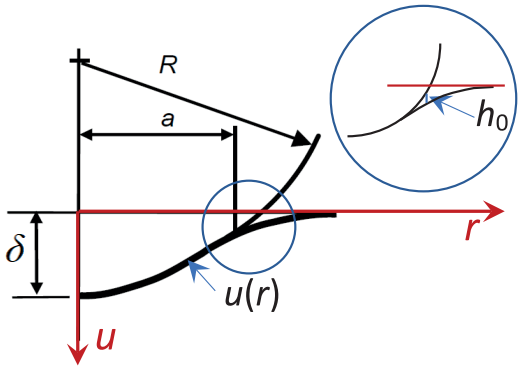

Fig. 3.2. Profile of elastic deflection of the plane after the indentation of an infinitely rigid sphere with radius *R*

Source: Own work based on [2].

The profile provided by Hertz for $r \leq a$ is given by:

$$u(r) = \delta - \frac{r^2}{2R} \tag{3.10}$$

or as a function of the contact radius *a*:

$$u(r) = \frac{1}{E}\frac{3}{2}\frac{P}{4a}\left(2 - \frac{r^2}{a^2}\right) \tag{3.11}$$

The profile $u(r)$ for $r > a$ is given by:

$$u(r) = \frac{1}{\pi R}\left[(2a^2 - r^2)\arcsin\left(\frac{a}{r}\right) + a\sqrt{r^2 - a^2}\right] \tag{3.12}$$

Hertz also determined the pressure profile $p(r)$ in the substrate into which an infinitely rigid sphere is indented. Since the entire system is symmetric around the vertical axis passing through the center of the sphere, the pressure profile is axisymmetric. Hertz demonstrated that this pressure profile is given by:

$$p(r) = p_0\sqrt{1 - \frac{r^2}{a^2}} \tag{3.13}$$

where p_0 is the pressure at the axis of symmetry of the system (for $r = 0$):

$$p_0 = \frac{2E\delta}{\pi a} = \frac{2aE}{\pi r} = \frac{2E}{\pi}\sqrt{\frac{\delta}{R}} \tag{3.14}$$

The relationship between the force *P* exerted on the sphere and the displacement δ or the contact radius *a* can be determined by integrating the total pressure profile:

$$P = \int p(r) \cdot 2\,\pi\, r dr = \frac{4Ea\delta}{3} = \frac{4Ea^3}{3R} = \frac{4ER^{\frac{1}{2}}\delta^{\frac{3}{2}}}{3} \tag{3.15}$$

The system described above, involving an infinitely rigid sphere and a flat sample with stiffness *E*, represents an idealized case. This can be generalized to a system of two spheres with radii *R1* and *R2* and stiffnesses *E1* and *E2* (Fig. 3.3).

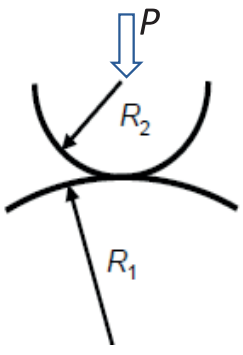

Fig. 3.3. System of two spheres pressed together by force *P*

Source: Own work based on [2].

In the system shown in Fig. 3.3, both spheres have different radii and stiffnesses, which means that both spheres will undergo elastic deformation, with the sphere of greater stiffness displacing into the sphere of lesser stiffness. For such a system, the relationships derived by Hertz apply, where the combined radius R and the reduced stiffness E^* of the system are defined as:

$$\frac{1}{R} = \frac{1}{R_1} + \frac{1}{R_2} \tag{3.16}$$

$$\frac{1}{E^*} = \frac{(1-\nu_1^2)}{E_1} + \frac{(1-\nu_2^2)}{E_2} \tag{3.17}$$

where ν_1 and ν_2 are the Poisson's ratios for sphere 1 and sphere 2, respectively. Considering equations (3.16) and (3.17), the relationship between the compressive force and the contact radius can be expressed in accordance with equation (3.15) as follows:

$$P = \frac{4E^* a^3}{3R} \tag{3.18}$$

The pressure exerted by the system can be determined by normalizing the force P by the contact area πa^2, as follows:

$$p_{\mathrm{m}} = \left(\frac{4E^*}{3\pi}\right)\frac{a}{R} \tag{3.19}$$

3.2. Models Considering Adhesion Forces between the Sphere and the Substrate

If some or all of the assumptions of Hertz's theory are not met, the contact problem between the bodies becomes more complex, and such contact problems are typically referred to as non-Hertzian. For example, classical contact theory primarily focused on the interaction between the indenter and the substrate where no adhesion forces exist between them. However, when the distance between the substrate material and the indenter becomes very small (approaching atomic distances), adhesive attraction forces (van der Waals forces) begin to act, requiring a tensile force to separate the indenter from the substrate in order to overcome these forces. To account for the effect of adhesion in Hertzian contact, Johnson, Kendall, and Roberts [5] formulated the JKR adhesive contact theory, utilizing the balance between stored elastic energy and the loss of surface energy between a spherical indenter and a flat surface. The JKR model considers the influence of both contact pressure and adhesion only within the contact area. The general solution for the pressure distribution within the contact area in the JKR model is given by:

$$p(r) = p_0\left(1 - \frac{r^2}{a^2}\right)^{\frac{1}{2}} + p_0'\left(1 - \frac{r^2}{a^2}\right)^{-\frac{1}{2}} \tag{3.20}$$

Equation (3.20), compared to equation (3.13), contains an additional term related to surface energy. In equation (3.20), p_0 is described by equation (3.14), while p'_0 is given by:

$$p_0' = -\left(\frac{4\gamma E^*}{\pi a}\right)^{\frac{1}{2}} \tag{3.21}$$

where 2γ is the total surface energy of both surfaces (the indenter and the substrate) per unit contact area. By integrating equation (3.20), the relationship between the contact radius and the applied force is obtained:

$$a^3 = \frac{3R}{4E^*}\left(P + 6\gamma\pi R + \sqrt{12\gamma\mu RP + (6\gamma\mu R)^2}\right) \tag{3.22}$$

When the surface energy is zero, equation (3.22) reduces to equation (3.18) as given by Hertz. When the applied force P is zero, the contact radius is given by (Figs. 3.4b, 3.4d):

$$a^3 = \frac{9R^2\gamma\pi}{E^*} \tag{3.23}$$

From equation (3.22), the force P_c required to overcome the adhesion forces between the surface of the sphere and the surface of the substrate material (i.e., when $a = 0$; Fig. 3.4f) can also be calculated:

$$P_c = -3\gamma\pi R \tag{3.24}$$

It is important to note that the force P_c does not depend on the elastic moduli of the materials in contact. For the force P_c, the contact radius is given by (Fig. 3.4f):

$$a_c^3 = \frac{9R^2\gamma\pi}{4E^*} \tag{3.25}$$

If the work required to overcome the adhesion forces is defined as:

$$\Delta\gamma = \gamma_1 + \gamma_2 - \gamma_{12} \tag{3.26}$$

where γ_1, γ_2, and γ_{12} are the surface energies of the sphere, the substrate, and the interaction component between these surfaces, respectively, then the contact radius for the JKR theory is given by (Fig. 3.4c):

$$a^3 = \frac{3R}{4E^*}\left(P + 3\Delta\gamma\,\pi\,R + \sqrt{6\Delta\gamma\,\pi\,RP + (3\Delta\gamma\,\pi\,R)^2}\right) \tag{3.27}$$

the tensile force required to separate the sphere from the substrate is:

$$P_c = -\frac{3}{2}\Delta\gamma\,\pi\,R \tag{3.28}$$

the critical contact radius is described by the following relationship:

$$a_c^3 = \frac{9R^2\Delta\gamma\,\pi}{8E^*} \tag{3.29}$$

and the critical penetration depth at the point of adhesive bond failure is given by (Fig. 3.4d):

$$\delta_c = \frac{a_c^2}{R} = \left(R^{\frac{1}{2}}\frac{9\Delta\gamma\,\pi}{4E^*}\right)^{\frac{2}{3}} \tag{3.30}$$

Alternative models also emerged that considered adhesion forces between the sphere and the substrate, such as the Derjaguin–Muller–Toporov (DMT) elastic contact model [6, 7]. In this model, it was assumed that the contact profile between the contacting sphere and the substrate is the same as in Hertzian theory; however, there are also attractive forces $_{acting}$ between the bodies that extend beyond the contact area. The authors of this model derived an equation describing the relationship between the contact radius and the applied load, as well as the tensile force required to break the adhesive bond, as follows:

$$a^3 = \frac{3R}{4E^*}(P + 4\gamma\,\pi\,R) \tag{3.31}$$

$$P_c = -4\gamma\,\pi\,R \tag{3.32}$$

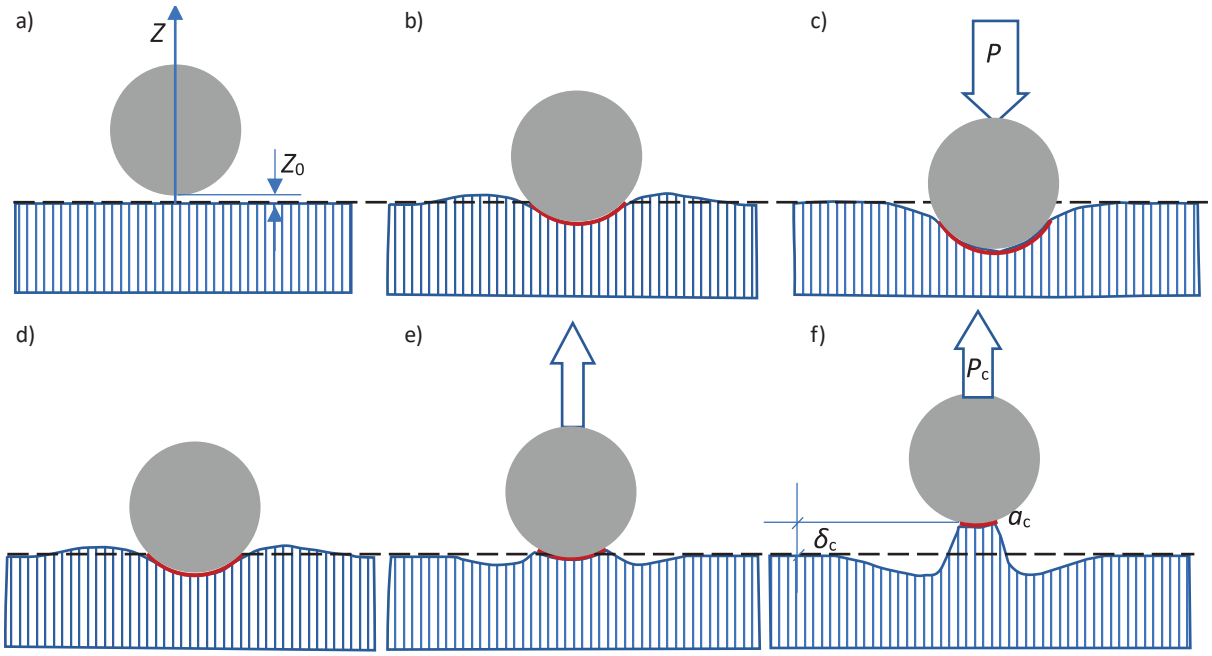

Fig. 3.4. Various phases of contact in JKR theory. The approach phase, where adhesion forces cause attraction at distance z_0 (a); bodies joined by adhesion forces (b); elastic deformation of the substrate after load application (c); state after load removal (d); detachment phase of adhesively bonded bodies (e); moment of separation of adhesively bonded bodies (f)

Source: Own work based on [5].

When the force P_c is reached during the withdrawal of the indenter, the contact between the contacting bodies will be broken. Equations (3.31) and (3.32), like equations (3.28) and (3.29), can be expressed as a function of the work required to overcome the adhesion forces $\Delta\gamma$; thus:

$$a^3 = \frac{3R}{4E^*}(P + 2\Delta\gamma\,\pi\,R) \tag{3.33}$$

$$P_c = -2\Delta\gamma\,\pi\,R \tag{3.34}$$

Tabor demonstrated in his work [8] that the JKR and DMT theories can be related through the parameter μ:

$$\mu = \frac{\delta_c}{z_0} \approx \left[\frac{R(\Delta\gamma)^2}{E^{*2}z_0^3}\right]^{\frac{1}{3}} \tag{3.35}$$

and that they represent extreme cases of the same theory. In equation (3.35), z_0 represents the distance between the sphere and the substrate at which, during the approach of the bodies, they become joined by adhesion forces (Fig. 3.4a). When the parameter μ takes on large values, i.e., for spheres with a large radius and a high value of the work required to overcome the adhesion forces $\Delta\gamma$, the JKR model equations are relevant. In contrast, the DMT model applies when both bodies have high stiffness and a large distance z_0, at which the adhesive bond is formed between them. These observations have been confirmed in subsequent studies [9–11]. In 1992, Maugis [12] further developed Tabor's model. In his model, Maugis represented the surface forces acting between bodies in contact using the approach proposed by Dugdale [13], and he expressed the work required to overcome the adhesion forces as $\Delta\gamma = \sigma_0 \cdot h_0$. In this equation, σ_0 is the maximum stress resulting from the Lennard-Jones potential [14]. The distance h_0 can be calculated by equating the area under the Lennard-Jones curve with the area under the Dugdale curve (Figs. 3.2, 3.5).

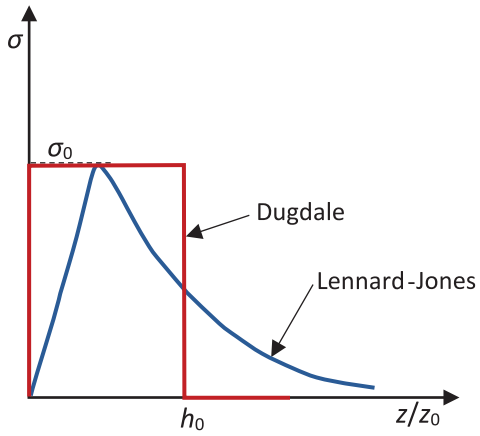

Fig. 3.5. Variation of stresses induced by adhesion forces according to Dugdale and Lennard-Jones
Source: Own work based on [13, 14].

The assumptions made imply that for the distance z between the bodies in the range $<z_0, z_0+h_0>$, the attractive force between the two surfaces remains constant. An ideal contact between the sphere and the substrate occurs at a distance $r = a$ (see Fig. 3.2), and the maximum adhesive forces inducing stresses σ_0 occur within the distance $a \le r \le c$. Within this range of distance from the axis of symmetry, the two surfaces are separated by $h(r{=}a) = 0$ and $h(r{=}c) = h_0$ (see Fig. 3.2). Johnson and Greenwood [15] proposed describing the pressure exerted on the substrate surface, into which the sphere is indented, as the sum of the pressures given by Hertz $p(r)$H and the pressures induced by Dugdale stresses $p(r)^D$, i.e.:

$$p(r) = p(r)^H + p(r)^D \tag{3.36}$$

where $p(r)^H$ is described by equations (3.13) and (3.14), and $p(r)^D$ is given by:

$$p(r)^{\mathrm{D}} = \begin{cases} -\frac{\sigma_0}{\pi}\cos^{-1}\left[\frac{2-m^2\frac{r^2}{a^2}}{m^2\left(1-\frac{r^2}{m^2a^2}\right)}\right] & \text{for } r \le a \\ -\sigma_0 & \text{for } a < r \le c \end{cases} \tag{3.37}$$

where $m = c/a$. Similarly, the total load on the sphere is $P = P^{\mathrm{H}} + P^{\mathrm{D}}$. In this case, P^{H} is described by equation (3.15), and P^{D} is given by:

$$P^{\mathrm{D}} = -2\sigma_0 m^2 a^2\left[\cos^{-1}\left(\frac{1}{m}\right) + \frac{1}{m^2}\sqrt{m^2-1}\right] \tag{3.38}$$

Similarly, the distance between the contacting bodies at a distance c from the axis of symmetry of their contact is determined as follows:

$$h(c) = h(c)^{\mathrm{H}} + h(c)^{\mathrm{D}} \tag{3.39}$$

$h(c)^{H}$ can be determined from Hertz's equations as follows:

$$h(c)^{\mathrm{H}} = \frac{c^2}{2R} - \delta + u(c) \tag{3.40}$$

where δ is determined from equation (3.1), and $u(c)$ from equation (3.12). $u(c)$ can also be expressed as a function of the parameter m as:

$$u(c) = \frac{1}{\pi R}\left[a^2(2-m^2)\sin^{-1}\left(\frac{1}{m} + a^2\sqrt{m^2-1}\right)\right] \tag{3.41}$$

However, the distance between the contacting bodies at a distance c, caused by Dugdale stresses, can be determined by the following relationship:

$$h(c)^{\mathrm{D}} = \left(\frac{4\sigma_0 a}{\pi E^*}\right)\left[\sqrt{m^2-1}\cos^{-1}\left(\frac{1}{m}\right) + 1 - m\right] \tag{3.42}$$

and the displacement of the sphere caused by adhesive stresses δ^{D} is given by:

$$\delta^{\mathrm{D}} = -\left(\frac{2\sigma_0 a}{E^*}\right)\sqrt{m^2-1} \tag{3.43}$$

Taking adhesive interactions into account, the contact area between the sphere and the substrate is given by:

$$\bar{A} = \pi c^2 \tag{3.44}$$

and the load is given by:

$$\bar{P} = \frac{P}{\pi \Delta\gamma R} \tag{3.45}$$

Similarly to equation (3.18), the load can also be expressed as a function of the contact radius:

$$\bar{P} = \bar{a}^3 - \lambda\bar{a}^2\left(\sqrt{m^2-1} + m^2\sec^{-1} m\right) \tag{3.46}$$

where:

$$\bar{a} = \alpha a \tag{3.47}$$

whereas:

$$\alpha = \left(\frac{4E^*}{3\pi\Delta\gamma R^2}\right)^{\frac{1}{3}} \tag{3.48}$$

and λ is given by:

$$\lambda = \sigma_0\left(\frac{9R}{2\pi\Delta\gamma E^{*2}}\right)^{\frac{1}{3}} \tag{3.49}$$

If in *equation* (3.49) it is assumed that the stresses σ_0 reach the theoretical value given by the Lennard-Jones potential σ_{th} (as shown in Fig. 3.5), which is:

$$\sigma_{\mathrm{th}} = \frac{16\Delta\gamma}{9\sqrt{3}z_0} \tag{3.50}$$

then the parameter $\lambda \approx 1{,}16\mu$. Another method for determining the stresses σ_0 was proposed by Zheng and Yu [16]. According to them:

$$\sigma_0 = \exp\left(-\frac{223}{420}\right) \cdot \frac{\Delta\gamma}{z_0} \approx 0{,}588\frac{\Delta\gamma}{z_0} \tag{3.51}$$

If the stresses σ_0 are determined in this manner, the parameter $\lambda \approx 0{,}663\mu$. It is worth noting that the parameter λ is equivalent to the parameter μ proposed by Tabor. Similarly to equation (3.8), but taking into account adhesion forces, the displacement of the sphere into the substrate can be determined from the following equation:

$$\bar{\delta} = \bar{a}^2 - \frac{4}{3}\lambda\bar{a}\sqrt{m^2-1} \tag{3.52}$$

Using the relationships presented above, the equation describing the distance between the contacting bodies in the adhesive gap can be expressed as:

$$\frac{\lambda\bar{a}^2}{2}\left[(m^2-2)\sec^{-1}m + \sqrt{m^2-1}\right] + \frac{4\lambda\bar{a}}{3}\left[\sqrt{m^2-1}\sec^{-1}m - (m+1)\right] = 1 \tag{3.53}$$

By solving equation (3.53), the contact radius c (considering adhesion forces) can be obtained as a function of the contact radius a (without considering adhesion forces) and the parameter λ. From this equation, it follows that for large values of the parameter λ, the contact radius c approaches the contact radius a, meaning that the parameter m tends toward 1. In this case, the conditions of the JKR model are satisfied. Conversely, for small values of the parameter λ, the conditions of the DMT model are met.

3.3. Models for Flat Surfaces Considering their Roughness

When two bodies come into contact, due to the roughness of their surfaces, they only touch at the peaks of the surface asperities (Fig. 3.6). This results in the actual contact area being significantly smaller than the nominal contact area of the bodies. Engineering surfaces exhibit roughness over a wide range of scales, down to the molecular level. Additionally, surface structures exhibit self-similarity, often described in the literature as surface fractality. In practice, a linear relationship is observed between the contact area and the load (the normal force applied to the contacting surfaces) [17]. This relationship can be described by the following equation [18]:

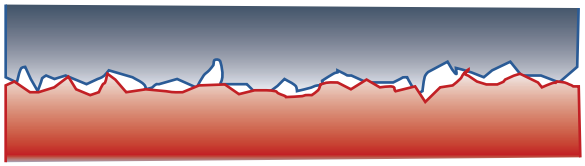

Fig. 3.6. Contact between two rough bodies

Source: own work.

$$A = \frac{\kappa}{E^* h'}P \tag{3.54}$$

where h' is the root mean square deviation from the mean line, i.e., the theoretical line for which the sum of the squares of the distances of peaks and valleys is minimized, and $\kappa \approx 2$. By rearranging equation (3.54), the mean pressure can be determined as follows:

$$p_{\text{av}} = \frac{P}{A} \approx \frac{1}{2}E^* h' \tag{3.55}$$

As indicated by equation (3.55), the mean pressure is half the product of the reduced elastic modulus of both bodies (equation (3.17)) and the root mean square deviation from the mean line. In cases where the mean pressure reaches 1.1 times the yield strength (under uniaxial stress conditions), assuming a Gaussian distribution, the surface asperities will undergo plastic deformation at the points of contact. The above assumption is approximately met when the hardness determined in the indentation test is 39% of the measured value [20]. Another index describing elastoplastic deformations during the contact of surface asperities was proposed by Mikić [21]:

$$\Psi = \frac{E^* h'}{\sigma_0} > \frac{2}{3} \tag{3.56}$$

If Ψ reaches a value greater than 2/3, then the contact of the asperity peaks is entirely plastic. In equation (3.56), σ_0 represents the hardness determined in the indentation test. Both conditions for plastic deformation of the contacting asperity peaks assume that the actual contact area is proportional to the load, as in equation (3.54). Therefore,

whether the system behaves plastically or elastically is independent of the applied normal force, yet it depends on both the load and the actual contact area.

In 1966, Greenwood and Williamson [19] considered the contact between a smooth rigid plane and a flat deformable surface with rounded asperities having a radius R (Fig. 3.7). The Greenwood and Williamson (GW) theory assumes that:

- the heights of the asperities follow a Gaussian distribution;
- the deformation of each asperity is independent of the deformation of its neighbors;
- the deformation of the asperities is described by the Hertz model;
- the probability that the height of an asperity lies within the interval $<z, z+dz>$ is given by $\phi(z)dz$;
- the radius of curvature at the asperity peak is constant;
- adhesion forces that occur in the contact between asperities and the smooth surface are neglected.

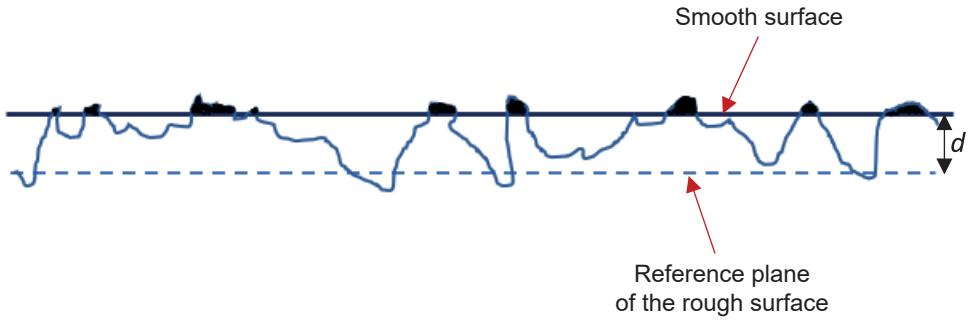

Fig. 3.7. Contact between a flat surface and a rough surface. The load is carried only through contact with the asperities whose heights exceed the distance from the reference plane

Source: Own work based on [19].

If it is assumed that there are N asperities on the surface, the expected number of contacts n with the flat surface will be:

$$n = N \int_d^\infty \Phi(z)dz \tag{3.57}$$

The expected total contact area between the asperities and the flat surface will be:

$$A_a = N\,\pi\,R \int_d^\infty (z-d)\Phi(z)dz \tag{3.58}$$

and the total load will be:

$$P = \frac{4}{3} N E_r \sqrt{R} \int_d^\infty (z-d)^{\frac{3}{2}} \Phi(z)dz \tag{3.59}$$

where z and R are the height and the radius of curvature of the asperities, respectively, and d is the distance between the smooth surface and the reference plane of the rough surface (Fig. 3.7). E_r is the equivalent reduced stiffness E^* (equation (3.17)). The equations (3.56)–(3.58) were also presented by Greenwood and Williamson in a normalized form, for which they used statistical functions introduced to fit the assumed Gaussian distribution of asperity heights:

$$F_n(h) = \int_h^\infty (s-h)^n \Phi^*(s)ds \tag{3.60}$$

where $\Phi^*(s)$ is the normalized distribution of asperity heights consistent with the Gaussian distribution, and h is the normalized (dimensionless) distance between the planes, defined as $h = d/\sigma$ (Fig. 3.7), with σ being the standard deviation of the asperity height distribution. The standard deviation for h and $\Phi^*(s)$ is equal to 1. In normalized form, the equations (3.56)–(3.58) are written as follows:

$$n = \eta A_n F_0(h) \tag{3.61}$$

$$A_a = \pi\,\eta A R \sigma F_1(h) \tag{3.62}$$

$$P = \frac{4}{3} \eta A E_r \sqrt{R} \sigma^{\frac{3}{2}} F_{\frac{3}{2}}(h) \tag{3.63}$$

where η is the surface density of asperities. As indicated by equations (3.60) and (3.61), the actual contact area A_a and the load P can be calculated once the functions $F_n(h)$ for the rough surface are determined [22]. The exact value of this function for $n = 1$ and $n = 3/2$ was provided by Jedynak in his work [23]:

$$F_1(h) = \frac{1}{\sqrt{2\,\pi}} \exp\left(-\frac{1}{2}h^2\right) - \frac{1}{2}h\ erfc\left(\frac{h}{\sqrt{2}}\right) \tag{3.64}$$

$$F_{\frac{3}{2}}(h) = \frac{1}{4\sqrt{\pi}} \exp\left(-\frac{h^2}{4}\right)\sqrt{h}\left[(h^2+1)K_{\frac{1}{4}}\left(\frac{h^2}{4}\right) - h^2 K_{\frac{3}{4}}\left(\frac{h^2}{4}\right)\right] \tag{3.65}$$

where $erfc(z)$ denotes the complementary error function, and $K_v(z)$ is the modified Bessel function of the second kind. In the literature, various approximations of the functions $F_n(h)$ assuming a Gaussian distribution of asperity heights have been proposed. For example, in [23], Jedynak proposed approximations of the integrals of the functions $F_n(h)$ for n values of 1 and 3/2.

$$F_n(h) = \frac{a_0+a_1h+a_2h^2+a_3h^3}{1+b_1h+b_2h^2+b_3h^3+b_4h^4+b_5h^5+b_6h^6} \exp\left(-\frac{h^2}{2}\right) \tag{3.66}$$

For $F_1(h)$, the coefficients [a_0, a_1, a_2, a_3] are [0.398942280401; 0.159773732775; 0.0389687688311; 0.00364356495452], and [b_1, b_2, b_3, b_4, b_5, b_6] are [1.653807476138; 1.170419428529; 0.448892964428; 0.0951971709160; 0.00931642803836; - 6.383774657279 × 10^{-6}], respectively. For $F_{3/2}(h)$, the coefficients [a_0, a_1, a_2, a_3] are [0.430019993662; 0.101979509447; 0.0229040629580; 0.000688602924], and [b_1, b_2, b_3, b_4, b_5, b_6] are [1.671117125984; 1.199586555505; 0.46936532151; 0.102632881122; 0.010686348714; 0.0000517200271]. For the given coefficients, the maximum relative error is 9,93 × 10^{-8} %.

However, in most cases, it has been observed that engineering surfaces do not exhibit Gaussian distributions of surface asperity heights [24–26]. Nonetheless, the presented model can be used in cases where friction or the transmitted load is not critical to the analysis being conducted.

In subsequent years, Greenwood and Tripp [27] proposed another model for the contact between two flat and rough surfaces. In this model, the actual contact area A_a between the contacting asperity peaks and the transmitted load P are given by:

$$A_a = \pi^2(\eta\beta\sigma)^2 A F_2(\lambda) \tag{3.67}$$

$$P = \frac{8\sqrt{2}}{15}\pi(\eta\beta\sigma)^2\sqrt{\frac{\sigma}{\beta}}E' A F_{\frac{5}{2}}(\lambda) \tag{3.68}$$

In equations (3.67) and (3.68), the coefficients η, β and σ are roughness parameters (η is the density of asperity contacts for the contacting surfaces, β is the average radius of the asperity peaks in contact, and σ is the standard deviation of surface heights), A is the nominal contact area of the contacting bodies, $\lambda = h/\sigma$ is the Stribeck oil film parameter, where h is the distance between the reference planes of the rough surfaces, and σ is the standard deviation of the asperity height distribution. E' is the reduced elastic modulus of both surfaces, and $F_2(\lambda)$ and $F_{5/2}(\lambda)$ are statistical functions that adjust the asperity height distribution to the Gaussian distribution, similarly to equation (3.60). The exact and approximate values of the functions $F_2(\lambda)$ and $F_{5/2}(\lambda)$ were provided by Jedynak [23]. The exact values are:

$$F_2(\lambda) = \frac{1}{2}(h^2+1)\ erfc\left(\frac{h}{\sqrt{2}}\right) - \frac{h}{\sqrt{2\pi}}\exp\left(-\frac{1}{2}h^2\right) \tag{3.69}$$

$$F_{\frac{5}{2}}(\lambda) = \frac{1}{8\sqrt{\pi}}\exp\left(-\frac{h^2}{4}\right)h^{\frac{3}{2}}\left[(2h^2+3)K_{\frac{3}{4}}\left(\frac{h^2}{4}\right) - (2h^2+5)K_{\frac{3}{4}}\left(\frac{h^2}{4}\right)\right] \tag{3.70}$$

and the approximate values can be determined from equation (3.66), with the coefficients for $n = 5/2$ being [a_0, a_1, a_2, a_3] equal to [0.616634218997; 0.108855827811; 0.023453835635; 0.000449332509] and [b_1, b_2, b_3, b_4, b_5, b_6] equal to [1.919948267476; 1.635304362591; 0.799392556572; 0.240278859212; 0.043178653945; 0.003863334276], with the maximum relative error for these coefficients not exceeding 4,98 × 10^{-8} %. For $n = 2$, the coefficients [a_0, a_1, a_2, a_3] are [0.5; 0.182536384941; 0.039812283118; 0.003684879001] and [b_1, b_2, b_3, b_4, b_5, b_6] are [1.960841785003; 1.708677456715; 0.856592986083; 0.264996791567; 0.049257843893; 0.004640740133], with the maximum relative error for these coefficients not exceeding 1,67 × 10^{-7} %.

3.4. Conical Indenter and other Indenters with an Apex Angle

All the relationships provided in subsections 3.1, 3.2, and 3.3 pertain to the elastic deformation of contacting and compressed bodies. However, determining the mechanical properties of solids in an indentation test would not be possible based solely on the relationship $P = f(\delta)$ within the elastic deformation range. This is because it is not experimentally feasible to determine the contact area A_c, which depends on the contact radius a. To determine the contact radius, plastic deformation of the tested material is necessary. Indentation tests are often performed for very small indenter displacements, in the nanometer range (nanoindentation); in such cases, the applied loads are small (in the mN or even μN range). To induce plastic deformation of the tested material under such small loads, it is essential to use an indenter with a sharp apex angle. In this scenario, plastic deformation occurs immediately upon contact between the indenter and the material (assuming a sharp angle without rounding). Therefore, to enable the development of the indentation method for determining material properties, relationships similar to those derived by Hertz for a sphere also had to be derived for a conical indenter. This was accomplished by the Scottish mathematician Sneddon [4], approximately 70 years after Hertz's work was published [1]. When using a conical indenter with a sharp apex angle, the material deforms elastically and plastically from the moment of loading, unlike the case of a spherical indenter, where it is possible to achieve a situation where, under small elastic loads, the curve $P = f(h)$ remains in the elastic range. (where P is the load on the indenter and h is its displacement into the substrate material), the curve during loading and unloading of the indenter would follow the same path. In this case, the curve during loading does not coincide with the curve during unloading because loading is accompanied by both plastic and elastic deformation of the substrate, whereas unloading involves only the elastic response of the substrate (Fig. 3.8). When the indenter has a conical shape, as it penetrates the substrate material with increasing load, the impression left in the material replicates the shape of the cone (assuming infinite stiffness of the indenter). Similar to the spherical indenter, at a distance equal to the contact radius a, the contact between the substrate material and the indenter is lost. This situation is illustrated in Fig. 3.9. During the unloading of the indenter, only the elastic response of the substrate occurs, which ultimately determines the shape of the impression left in the material. This scenario is depicted in Fig. 3.10.

In the mid-20th century, Sneddon derived the relationship between the load P and the contact radius a for the case of contact between an infinitely rigid conical indenter and an elastic, semi-infinite half-space with stiffness E. Sneddon demonstrated that the pressure distribution profile in the material is given by:

$$p(r) = \frac{Eh_0}{\pi a(1-\nu^2)} \ln\left(\frac{a}{r}\right) + \sqrt{\left(\frac{a}{r}\right)^2 - 1} = \frac{Eh_0}{\pi a(1-\nu^2)} \cosh^{-1}\left(\frac{a}{r}\right) \tag{3.71}$$

Similar to the case of sphere indentation, the relationship between the force P exerted on the cone and the displacement h_0 or the contact radius a can be determined by integrating the total pressure profile over r. This yields the following [28]:

$$P = \frac{\pi E}{2(1-\nu^2)} a^2 \mathrm{tg}(\theta) = \frac{2E}{\pi (1-\nu^2)} \frac{{h_0}^2}{\mathrm{tg}(\theta)} \tag{3.72}$$

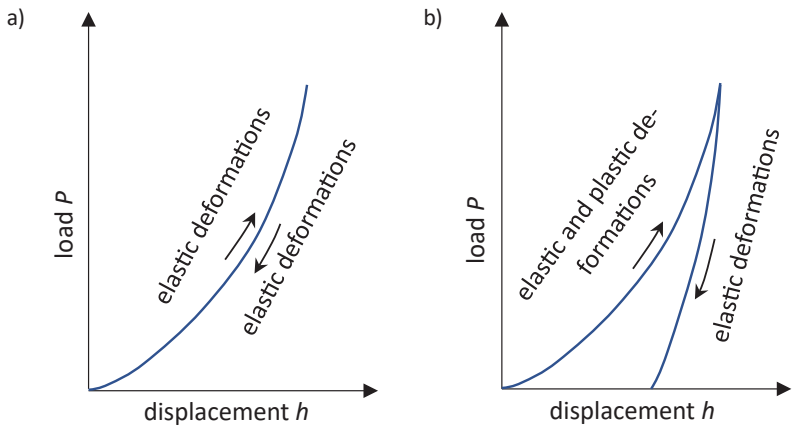

Fig. 3.8. Loading and unloading curves (direction indicated by arrows) for a spherical indenter (a) and a conical indenter (b)

Source: Own work based on [4].

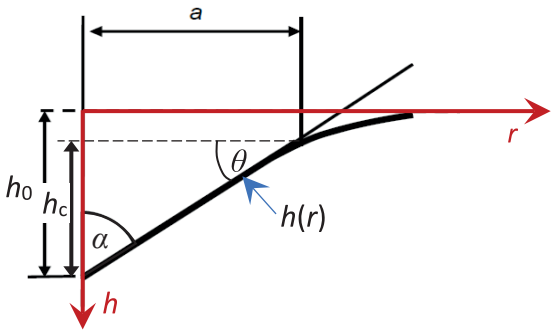

Fig. 3.9. Elastic deflection profile of the plane during the indentation of an infinitely rigid cone with an apex angle of 2α

Source: Own work based on [4].

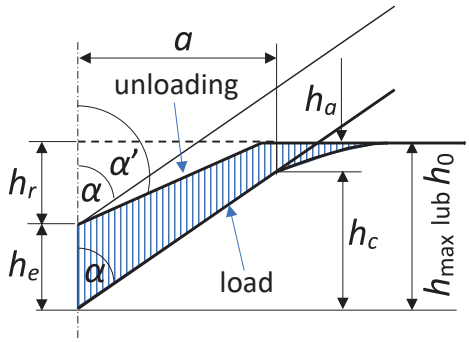

Fig. 3.10. Diagram illustrating the change in the impression profile caused by the elastic response of the substrate material (shaded area) during unloading; h_0 or h_{max} – maximum displacement of the cone into the substrate under maximum load, h_c – contact depth of the cone with the substrate corresponding to the contact radius *a*, h_a – depth at which the cone lost contact with the substrate, h_e – depth of elastic deformation of the substrate along the cone axis, h_r – depth of the impression in the material along the cone axis after unloading the indenter

Source: Own work based on [4].

In the case where the finite stiffness of the conical material is considered, the relationship (3.72) between the load *P* and the displacement h_0 of the cone, expressed in terms of the semi-angles of the conical indenter α, will be:

$$P = \frac{2}{\pi} E^* \cdot {h_0}^2 \cdot \mathrm{tg}\alpha \tag{3.73}$$

Sneddon also provided an equation describing the displacement of the free surface of the sample beneath the indenter. For $r \leq a$, it is given by:

$$h(r) = \left(\frac{\pi}{2} - \frac{r}{a}\right) a \cdot \mathrm{ctg}\alpha \tag{3.74}$$

The contact depth h_c is geometrically related to the contact radius *a* by the equation $h_c = a \cdot \mathrm{ctg}\alpha$ (Fig. 3.9). The total depth of the cone's displacement h_0 (along its axis at h_0) is given by:

$$h_0 = \frac{\pi}{2} h_c \tag{3.75}$$

Which can ultimately be expressed as:

$$h_0 = \frac{\pi}{2} a \cdot \mathrm{ctg}\alpha \tag{3.76}$$

It is important to note that the displacement designations of the indenter in Figs. 3.9 and 3.10 can be somewhat misleading, as Fig. 3.9 depicts, according to Sneddon's assumptions, purely elastic deformation of the substrate, while Fig. 3.10 shows its actual elastoplastic deformation. Therefore, Sneddon's equations describe only the shaded area in Fig. 3.10, and the displacement h_0 in equations (3.71)–(3.73) and (3.75) and (3.76) corresponds to the displacement h_e shown in Fig. 3.10. According to the designations presented in Fig. 3.10, Sneddon's equations can thus be written as:

$$P = \frac{2}{\pi} E^* \cdot {h_e}^2 \cdot \mathrm{tg}\alpha' \tag{3.77}$$

$$h(r) = \left(\frac{\pi}{2} - \frac{r}{a}\right) a \cdot \mathrm{ctg}\alpha' \tag{3.78}$$

where α' is the half-apex angle of the conical impression in the substrate after unloading.

Pyramidal indenters are analyzed in terms of an equivalent conical indenter, which provides the same ratio of the contact area A to the contact depth h_c as in the case of a pyramidal indenter. In practice, various pyramidal indenters are used, primarily because the manufacturing process for such indenters is much simpler than for conical indenters. The simplest to manufacture is a pyramid with a triangular base, as it requires only three surfaces to be ground and polished. This shape was first proposed by Berkovich [29], who originally designed an indenter with an apex angle of 130.04°. However, indenters are now typically made with an apex angle of 130.54°. The cone equivalent to the Berkovich indenter has an apex angle of 140.592° (Fig. 3.11). For the Berkovich indenter, the relationship between the contact area A and the contact depth h_c is as follows:

$$A = 3\sqrt{3}h_c^2\mathrm{tg}^2\theta = 24{,}49h_c^2 \tag{3.79}$$

while the contact radius is given by:

$$a = h_c\mathrm{tg}70{,}276 = 2{,}79h_c \tag{3.80}$$

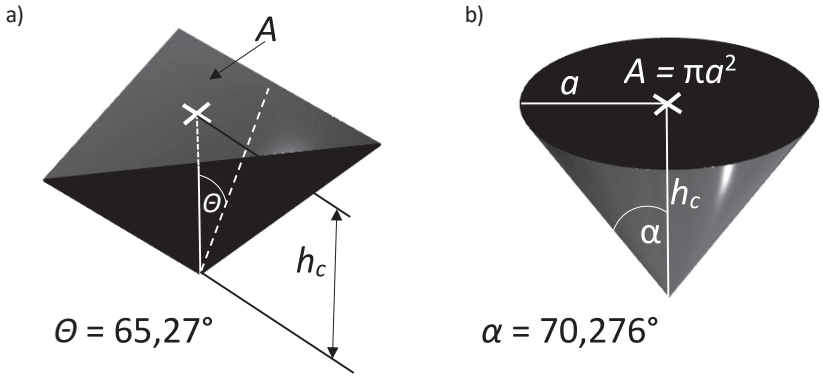

Fig. 3.11. Berkovich indenter (a) and its equivalent conical indenter (b)

Source: Own work based on [29].

The second type of commonly used indenter shapes is a pyramid with a triangular base and an apex angle of 70.53°—the so-called cube corner (Fig. 3.12). For this indenter, the relationship between the contact area A of the indenter with the substrate and the contact depth h_c is given by:

$$A = 3\sqrt{3}h_c^2\mathrm{tg}^2\theta = 2{,}60h_c^2 \tag{3.81}$$

while the contact radius is given by

$$a = h_c\mathrm{tg}42{,}278 = 0{,}91h_c \tag{3.82}$$

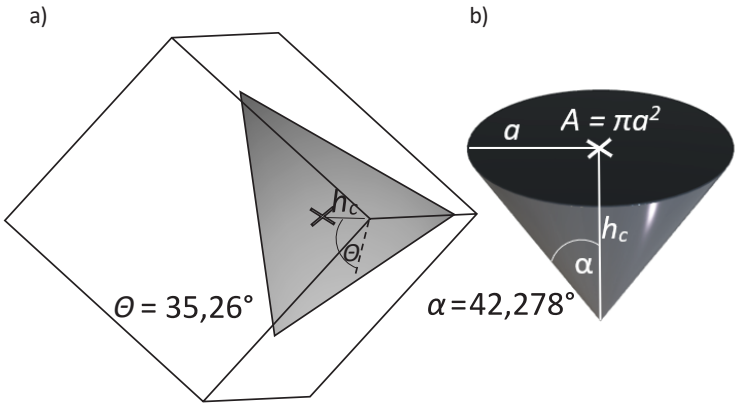

Fig. 3.12. Cube corner indenter (a) and its equivalent conical indenter (b)

Source: Own work.

The Vickers indenter, which has a square-based pyramid shape with an apex angle of 136° (Fig. 3.13), has a contact area given by:

$$A = 4h_c^2 \mathrm{tg}^2\theta = 24{,}50h_c^2 \tag{3.83}$$

while the contact radius is given by:

$$a = h_c \mathrm{tg}70{,}3 = 2{,}793h_c \tag{3.84}$$

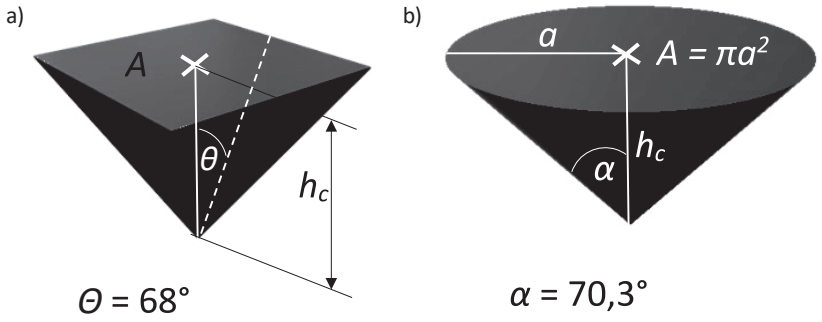

Fig. 3.13. Vickers indenter (a) and its equivalent conical indenter (b)

Source: Own work based on [41].

Another four-sided pyramid is the Knoop indenter (Fig. 3.14), which has two apex angles θ_1 = 172.5°and θ_2 = 130°. The equivalent cone has an apex angle of 155.28°. For this type of indenter, the contact area is given by:

$$A = 2h_c^2 \mathrm{tg}\theta_1 \mathrm{tg}\theta_2 = 108{,}21h_c^2 \tag{3.85}$$

while the contact radius is given by:

$$a = h_c \mathrm{tg}77{,}64 = 4{,}563h_c \tag{3.86}$$

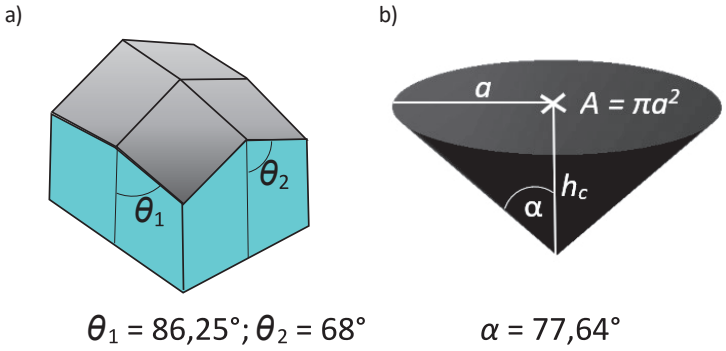

Fig. 3.14. Knoop indenter (a) and its equivalent conical indenter (b)

Source: Own work based on [42].

4. Hardness Measurements

4.1. Meyer Hardness

Over the past hundred years or so, many ideas and methods for determining material hardness have emerged. Generally, hardness can be described as the resistance a material exhibits when a penetrator (indenter) is pressed into it, which can be expressed as $H = P/A$. In this equation, P is the load applied to the indenter, and A is, in general, the area over which the applied load acts. Different methods of measuring hardness propose various ways to determine the area A. For example, Eugen Meyer [30], who worked at the Materials Testing Laboratory of the Imperial Technical School in Charlottenburg, proposed in 1908 that hardness be defined as the average pressure, based on the empirical relationship he observed between the pressure p (in MPa) exerted by a spherical indenter and the diameter of the indentation d:

$$p = kd^n \tag{4.1}$$

where k and n are constants that are often used to estimate strain hardening, as k increases while n decreases as the material undergoes strain hardening. It is important to note that in a double logarithmic plot, equation (4.1) presents a linear relationship between $\log p$ and $\log d$:

$$\log p = n \cdot \log d + \log k \tag{4.2}$$

The parameter n is the slope of the straight line obtained when plotting $\log p$ against $\log d$, and k is the value of p when $d = 1$. Fully annealed metals typically have an n value of around 2.5, while strain-hardened metals have an n value of approximately 2. The Meyer test was originally defined for spherical indenters but can be applied to any indenter shape. A key advantage of the Meyer test is its lower sensitivity to the applied load, especially when compared to the Brinell hardness test. For cold-worked materials, Meyer hardness is relatively constant and independent of the load, whereas Brinell hardness decreases with increasing load. For annealed materials, Meyer hardness continuously increases with load due to strain hardening (Fig. 4.1).

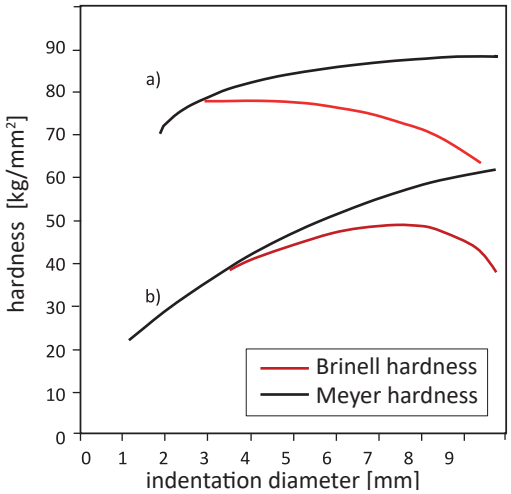

Fig. 4.1. Differences between Brinell hardness and Meyer hardness using a spherical indenter with a diameter of 10 mm for cold-rolled copper (curve a) and annealed copper (curve b)

Source: Own work based on [30].

It is important to note, however, that for indentation diameters below approximately $d = 0.5$ mm, the value of n can exceed 3. For this reason, Meyer's law is often limited to values of d greater than 0.5 mm and less than the diameter of the indenter [31]. It should also be noted that the area needed to determine hardness is the projection of the indentation area onto the plane of the material's surface (Fig. 4.2).

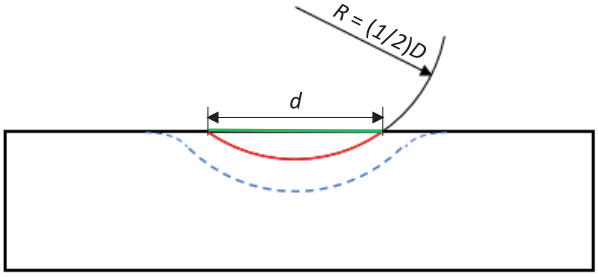

Fig. 4.2. Schematic of the indentation in the matial after Brinell hardness testing. The dashed line indicates the elastoplastic deformation of the tested material under maximum indenter load. The red line shows the surface area of the plastically deformed material after unloading, which is used to determine Brinell hardness, while the green line indicates the surface area used to determine Meyer hardness

Source: Own work based on [31].

4.2. Brinell Hardness

In 1900, Swedish engineer Johan August Brinell proposed a hardness measurement method based on the use of a spherical indenter and the application of large forces. The large size of the indentation left after the hardness test can lead to damage to the tested object, which limits the applicability of this method. However, it is worth noting that for steel, the hardness value divided by 2 gives an approximate value of the tensile strength expressed in ksi units (1 ksi = 6.894757 * 10^6 Pa). This characteristic contributed to the early adoption of the Brinell method compared to competing hardness tests. In a typical hardness test using this method, a carbide ball indenter with a diameter of 10 mm (0.39 inches) is used, and a load of 3000 kgf (29.42 kN) is applied. However, the applied forces can range from 9.807 N (1 kgf) to 29.42 kN (3000 kgf) [32]. ASTM and ISO define multiple Brinell scales, each determined by a combination of the applied force and the indenter ball diameter. For spherical indenters, the geometry of the indenter is not as challenging as it is for indenters with an apex angle, which always have some degree of rounding, altering the deformation conditions of the tested material. The challenge lies more in the material of the indenter itself, which must be well-defined, as using a material that is too soft can result in a change in the ball's shape during indentation, affecting the stresses in the tested material and potentially altering the hardness result significantly. When testing soft materials, a lower force was applied, and for harder materials, a tungsten carbide ball was used instead of a steel ball. This approach was followed until the current standard (PN-EN ISO 6506-1) was established, which specifies the use of carbide materials for indenters. The test involves applying a specified force, holding it for a certain period, then removing the load and measuring the diameter d of the spherical indentation left in the tested material. The hardness is measured by dividing the maximum indenter load by the area of the spherical cap, which is a function of its diameter d and the diameter of the spherical indenter D (Fig. 4.2). The hardness is calculated using the formula:

$$HBW = \frac{2P}{\pi D\left(D-\sqrt{D^2-d^2}\right)} \tag{4.3}$$

There are two phenomena that complicate the measurement of the indentation edge and, consequently, the determination of the spherical cap area. First, the edge of the indentation is difficult to define and may be subject to varying interpretations. Equally problematic is the fact that two different systems for measuring the indentation diameter using optical microscopes may perceive the same edge differently. In the case of Brinell indentations, the challenge lies in defining the indentation edge, which is curved due to the pile-up or sinking of the deformed material at the edge of the indentation. Since the edge is curved, the most common measurement systems, such as optical light microscopes, display the edge differently depending on several factors, which contribute to variations in measurement results. Studies [30, 33, 34] have shown that these factors include light intensity, the direction of incident light, the numerical aperture of the objective, surface roughness, and the operator's subjective interpretation of the indentation edge. If each of these variables were optimized and clearly defined, the measurement of Brinell inden-

tations could also be standardized. Assessing the uncertainty in material hardness measurements using the Brinell method is typically a challenging issue. Probability and statistical methodologies are often employed to evaluate this uncertainty [35]. For instance, Herrmann and Polzin synthesized the uncertainties in hardness measurements using the law of propagation of errors in their work [36]. Additionally, in recent years, other methods for assessing measurement uncertainty have been developed, which can be applied to Brinell hardness testing. For example, Xintao et al. [37] proposed the use of fuzzy set theory, while Hessling [38] suggested the application of appropriate digital filters. Rebouça et al. [39] demonstrated that semi-automatic Brinell hardness measurement using image analysis is easier, faster, and less dependent on operator subjectivity. In another study [40], the authors precisely identified all sources of measurement uncertainty during Brinell hardness testing by utilizing finite element analysis.

4.3. Martens Hardness

The hardness measurement method is based on the continuous recording of the load, the depth of the indenter's penetration—typically a three- or four-sided diamond pyramid—and the duration of the applied load. The area A_s needed to calculate hardness (Fig. 4.3) is determined from the maximum indentation depth h_{max} and the indenter's shape. To do this, equations (3.79), (3.81), (3.83), and (3.85) are used, with the maximum indentation depth during loading being substituted into them. This method does not separate the elastic and plastic deformation of the tested material.

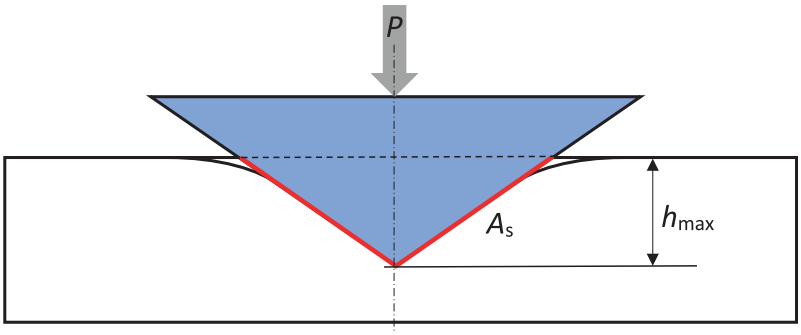

Fig. 4.3. Schematic of the indenter position under maximum load. The area As needed to determine hardness is marked in red

Source: Own work based on [31].

Martens hardness in its differential form is expressed as:

$$HM_{\text{diff}} = \frac{1}{\left(\frac{\partial h}{\partial \sqrt{P}}\right)^2 \frac{A_s}{h^2}} \tag{4.4}$$

When using an indenter in the form of a regular pyramid with an apex angle of 136°, i.e., a Vickers indenter (see Fig. 3.13), Martens hardness can be calculated using the following equation:

$$HM = \frac{P}{4h^2 \sin\theta / \cos^2\theta} = \frac{P}{26{,}43h^2} \tag{4.5}$$

However, when using a Berkovich indenter (see Fig. 3.11), Martens hardness is given by:

$$HM = \frac{P}{3\sqrt{3}h^2 \operatorname{tg}\theta / \cos\theta} = \frac{P}{26{,}97h^2} \tag{4.6}$$

Martens hardness can be used across various ranges of indenter load and displacement. It is generally accepted that when the indenter displacement is below 200 nm, the hardness measured is considered nanohardness. For maximum indenter loads of less than 2 N, microhardness can be determined, while macrohardness is measured at loads not exceeding 30 N. The hardness measurement method assumes that pyramidal indenters have no rounding of the apex angle. Additionally, the thickness of the tested sample must be at least ten times greater than the maximum depth of indenter displacement or three times greater than the diameter of the indentation. The test should be conducted under stable temperature conditions, meaning the temperature must remain constant. Another assumption of the method is that the zero point of measurement (the sample surface) must be determined with an accuracy of at least 1%, and the load should be applied perpendicular to the tested surface, free from vibrations and shocks. In the context of nanohardness measurements, the rate of load application should be within the range of 10–20 nm/s.

By referencing the maximum depth of indenter displacement, Martens hardness can be easily measured and calculated without the need for theoretical models. However, it does not correspond to existing definitions of hardness, especially in the case of materials with a low longitudinal elastic modulus.

4.4. Vickers Hardness

Vickers hardness was developed in 1921 by Robert L. Smith and George E. Sandland, who worked for Vickers Ltd., as an alternative to the Brinell method [41]. The shape of the indenter was designed to produce geometrically similar indentations, regardless of the load size, and to ensure that the indentation had well-defined measurement points. These conditions were met by designing the indenter in the form of a pyramid with a square base. Smith and Sandland determined that the ideal Brinell indentation size was 3/8 of the ball diameter. Since two tangents to a circle at the ends of a chord with a length of 3/8 of the diameter intersect at an angle of 136° (Fig. 4.4), they decided to adopt this angle as the angle between the planes of the indenter tip. This results in an angle of 22° from each surface normal to the horizontal plane on each side.

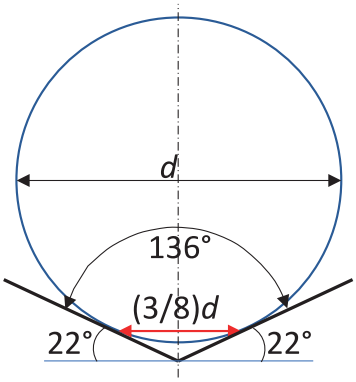

Fig. 4.4. Schematic illustrating the concept of the apex angle of the Vickers indenter

Source: Own work based on [41].

The apex angle was experimentally adjusted, and it was found that the hardness value obtained on a homogeneous piece of material remains constant, regardless of the applied load. Consequently, loads of varying magnitude are applied to a flat surface, depending on the hardness of the material being measured. The HV number is then determined by the ratio P/A, where P is the force applied to the indenter in kilogram-forces. The area A is given in square millimeters. It is determined by measuring the diagonals of the indentation d left by the indenter in the material after the load is removed (Fig. 4.5):

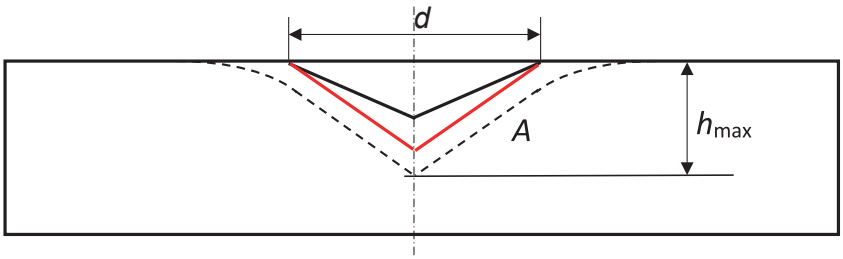

Fig. 4.5. Schematic illustrating the calculated area required to determine hardness using the Vickers method (red line). The solid black line represents the plastically deformed profile of the indentation after unloading, while the dashed line shows the indentation profile under maximum load

Source: Own work based on [41].

$$A = \frac{d^2}{1{,}8544} \tag{4.7}$$

4.5. Knoop Hardness

The hardness measurement method was developed by Frederick Knoop and colleagues in 1939 at the National Bureau of Standards (now the National Institute of Standards and Technology) in the United States. This test was designed for brittle and hard materials, as well as for measuring the hardness of thin coatings. It involves using an indenter in the shape of a pyramid with a rhombic base, where the ratio of the longer diagonal to the shorter one is 7:1, and the respective apex angles are 172° for the longer edge and 130° for the shorter edge (see Fig. 3.14). The depth of the indentation can be approximately determined as 1/30 of the length of the longer diagonal. Knoop [42] observed that, generally, the types of indentations for different materials can be classified according to the contour of the surface adjacent to the ends of the shorter diagonal. He identified three types of contours. Type A included contours with a distinct ridge (Fig. 4.6). The edge build-up effect is referred to in the literature as "pile up." Type B includes contours that show no visible disruption of the original surface at the edge of the shorter diagonal, while Type C includes those where a depression in the contact surface is observed, known in the literature as the "sink in" effect. Knoop noted for Type A profiles that the height h of the ridge decreases from a maximum at the ends of the shorter diagonal to zero as it approaches the ends of the longer diagonal. Knoop observed this type of indentation profile in rolled copper and C25 steel. Microscopic examinations using interference contrast revealed that the highest ridge occurs directly at the edge of the indentation. Type B profiles were those for which there was no visible material build-up at the indentation edge. In Type C profiles, the surface at a considerable distance beyond the ends of the shorter diagonal is depressed, as shown in Fig. 4.6c. In microscopic examinations, this type is recognized by the observer's inability to achieve sharp focus when measuring the indentation's diagonal. Knoop found this type of profile in cast gold. Hardness was defined as:

$$HK = \frac{P}{A_\mathrm{p}} = \frac{2P}{L^2} \cdot \frac{\tan\theta_1}{\tan\theta_2} = 14{,}229 \cdot \frac{P}{L^2} \tag{4.8}$$

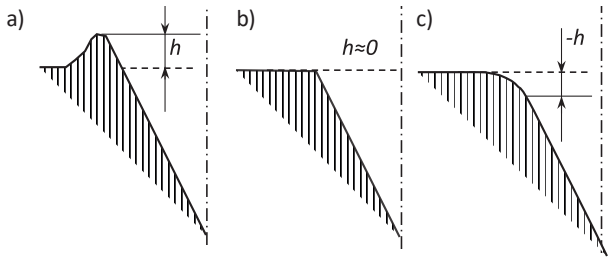

Fig. 4.6. Three types of indentation contours obtained in the Knoop test: a) Type A contour with surface pile-up at the edge; b) Type B contour without visible changes at the edge; c) Type C contour with surface sink-in effect

Source: Own work based on [42].

To calculate Knoop hardness (HK), the projected contact area A_p of the indenter onto a plane parallel to the surface of the tested material, after the load is removed, is used (Fig. 4.7). The projected contact area A_p is determined based on the measured longer diagonal L of the indentation.

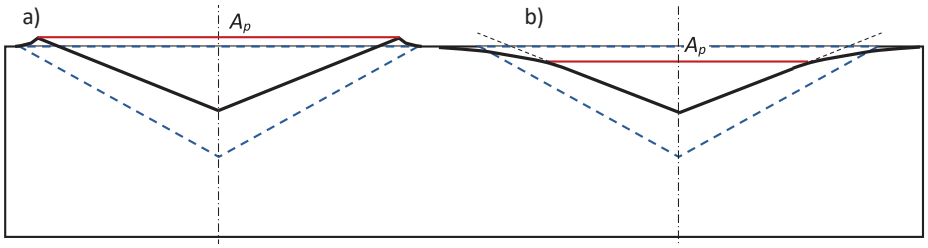

Fig. 4.7. Knoop indentation contours. The blue dashed line indicates the contour under load, the solid black line shows the contour of the indentation after load removal, and the red line marks the projected area A_p used to calculate Knoop hardness for Type A (a) and Type C (b) profiles. The longer diagonal L aligns with the red line Ap.

Source: Own work based on [42].

The advantage of the Knoop test is that it requires only a very small sample of material and is useful over a wide range of loads. However, the main disadvantages include the difficulties associated with using a microscope to measure the indentation (with an accuracy of up to 0.5 μm) and the time required for sample preparation and

indenter application. This procedure can be influenced by variables such as load, temperature, and environment, which have been thoroughly analyzed in studies [43–46].

4.6. Rockwell Hardness

The concept of measuring hardness using the depth difference method was first introduced in 1908 by Viennese professor Paul Ludwik in his book Die Kegelprobe (The Cone Test) [as cited in 47]. The depth difference method accounted for errors related to mechanical imperfections in the system, such as play and surface roughness. The Brinell hardness test, invented in Sweden, was developed earlier—in 1900—but it was time-consuming, unsuitable for fully hardened steel, and left too large of an indentation to be considered non-destructive. Hugh M. Rockwell (1890–1957) and Stanley P. Rockwell (1886–1940) from Connecticut, USA, jointly invented the "Rockwell hardness tester"—a device for measuring depth differences. They filed a patent application on July 15, 1914 [48]. The device was needed for quickly determining the impact of heat treatment on hardened steel bearing rings. The patent was approved on February 11, 1919, and was granted U.S. Patent 1,294,171. At the time of the invention, both Hugh and Stanley Rockwell were working for New Departure Manufacturing Co. in Bristol, CT [49]. The determination of Rockwell hardness requires the application of a minor preliminary load (typically 10 kgf, or 3 kgf for coating assessments), followed by the application of a major load, as illustrated in Figure 21. The magnitude of the major load depends on the selected Rockwell scale and ranges from 15 kgf to 150 kgf. According to the applicable standard PN-EN ISO 6508-1, the use of Rockwell indenters fitted with tungsten carbide composite balls is considered standard. Alternatively, steel indenters may be used, provided they comply with the requirements set forth in Annex A of the standard, which specifies special testing methods HR30TSm and HR15TSm intended for thin materials. The minor load serves to establish the zero reference position. After this reference is set, the major load is applied and subsequently removed, while the preliminary load is maintained. The penetration depth measured from the zero point is then read on a calibrated dial, where lower readings correspond to harder materials. This reflects the inverse proportionality between penetration depth and material hardness. A key advantage of the Rockwell hardness testing method is its capability to provide a direct readout of hardness values, thereby eliminating the need for complex post-measurement calculations that are often required in other hardness testing techniques.

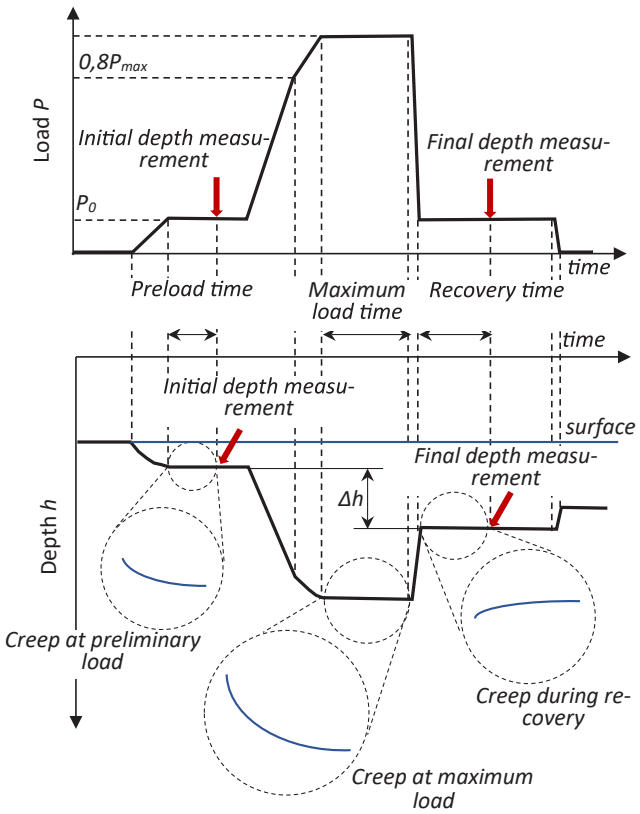

Fig. 4.8. Load variation and indenter displacement over time during the Rockwell hardness measurement process

Source: Own work based on [48].

5. Indentation Test

During the indentation test, both the load and the displacement of the indenter in the material are recorded during the loading and unloading phases. Indenters with an apex angle (such as Berkovich, Vickers, and Knoop) cause the material to undergo elastic-plastic deformation almost immediately after contact is made, particularly near the apex angle of the indenter [50–52]. After reaching the maximum load, the indenter is unloaded, and at this stage of the test, only the material's elastic response occurs (Fig. 5.1), which for a conical indenter is described by Sneddon's equations (equations (3.77) and (3.78)). In the case of pyramid-shaped indenters, an equivalent cone is assumed, characterized by the same base area-to-height ratio as the pyramid (subsection 3.4). The equivalent cone has a slightly larger apex angle than the pyramidal indenters.

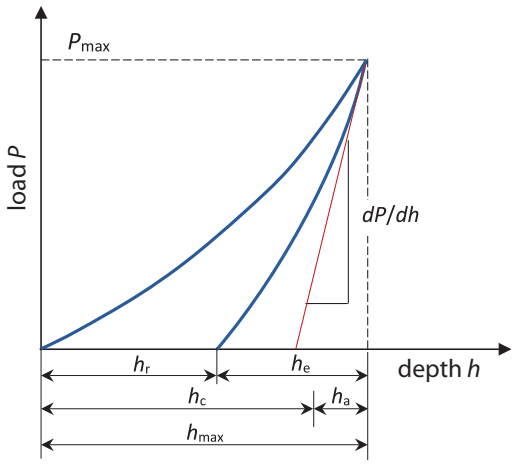

Fig. 5.1. The relationship between load and indenter displacement during an indentation test, showing the loading and unloading phases. The tangent to the unloading curve at the maximum indenter load is indicated by the red line

Source: Own work based on [51].

In indentation testing, a wide range of loads is used, ranging from micronewtons (μN) to several tens of newtons. The smallest load values allow for material characterization at the nano- or even picometric scale [53, 54]. The range of loads and indenter displacements used during indentation enables measurements to be conducted on both thin films and bulk materials. Nanoindentation testing requires not only the selection of the appropriate indenter geometry but also the precise adjustment of several other testing variables, such as the percentage of unloading, maximum load, and the manner in which the load is applied and removed. Typically, one of three loading and unloading scenarios is chosen: constant loading and unloading rate i.e., $dP/dt = C$, constant indenter displacement rate i.e., $dh/dt = C$ or constant material deformation rate i.e., $(dP/dt)\cdot 1/P = (dh/dt)\cdot 1/h = C$. When using small maximum loads in the range of μN and mN, the indentation test often becomes a compromise between indenter displacement and the surface roughness of the tested material. If the surface roughness is too large relative to the maximum indentation depth and the indenter tip radius, the assumption of semi-infinite half-space in Sneddon's contact equations will be invalid. Therefore, one of the most critical factors affecting the quality of results obtained during an indentation test is the condition of the tested material's surface, as well as the method of sample mounting. Cleaning and polishing influence the final surface roughness of the sample. Typical surface irregularities in a ma-

terial after polishing usually range between 200–500 nm, and contact equations assume an ideally flat surface, so any irregularities in the surface profile will cause deviations in the results. The impact of surface roughness on the measurements in an indentation test can be quantitatively assessed using the parameter α [55]:

$$\alpha = \frac{\sigma_S R}{a^2} \tag{5.1}$$

where σ_s represents the maximum height of the surface asperities, R is the tip radius of the indenter, and a is the contact radius. It is generally accepted that if the value of the parameter α is less than 0.05, the influence of the test conditions on the validity of the contact equations is minimal. Indenters used for nanoindentation tests are typically made from sintered, ground, and polished diamond, which is mounted in a stainless steel holder. The Berkovich indenter is frequently used in indentation tests. Unused Berkovich indenters have a tip radius of approximately 150 nm, which can increase to around 250 nm after one year of use [56]. Additionally, if the tip radius of a pyramidal indenter becomes too large, the fully developed plastic zone may not be achieved, which is crucial for the indentation test's objective of measuring the material's properties. Figure 5.2 shows an indentation curve obtained using a Berkovich indenter after three years of use. The large tip radius resulted in the material undergoing elastic deformation up to approximately 40 nm, consistent with Hertz's equations, with elastic-plastic deformation only occurring after the load exceeded 5 mN. In such cases, it is necessary to shift the starting point of the indentation curve, as illustrated in Figure 5.2. Another issue encountered during indentation testing of thin films or thin samples is the substrate's influence on the results. If the substrate is too soft compared to the hardness of the deposited film, it can significantly affect the measured properties. If the substrate is too soft compared to the hardness of the deposited coating, plastic deformation may occur in the substrate during the loading of the indenter. Conversely, if the substrate has insufficient stiffness relative to the coating, the measured elastic modulus of the coating may be influenced by the deformation of the substrate. Another issue that arises during the indentation test is the phenomenon of material creep. Creep occurs when the material is at a temperature (expressed in Kelvin) between 0.3 and 0.7 times its melting temperature T_t, where T_t is the melting temperature for metals and alloys, or the softening temperature for polymers. Consequently, metals and alloys with a melting temperature of, for example, 300°C, will undergo creep during an indentation test conducted at 20°C. In such cases, the displacement of the indenter recorded during the indentation test will include both the creep of the material and the penetration of the material by the indenter under load, leading to errors in material characterization. Another challenge in nanoindentation testing is the phenomenon of thermal drift. Thermal drift refers to a time-dependent measurement error in the displacement of the indenter during a nanoindentation test, caused by the thermal expansion of components within the measurement system. This manifests as an additional displacement superimposed on the measured or applied displacement of the indenter during the test. For instance, if an indentation test lasts 60 seconds and the maximum indenter displacement is expected to be 60 nm, but the measurement system's thermal drift is 1 nm/s, the measurement error caused by thermal drift can completely invalidate the true penetration depth reading (as illustrated in Figure 5.3). To mitigate the effects of thermal drift, several approaches are employed. The simplest method is to conduct measurements only when the temperatures of the sample and nanoindenter are stable during the test. Achieving temperature equilibrium between the sample and the indenter requires waiting an appropriate amount of time before taking measurements. To minimize random temperature fluctuations, the indenter is typically housed in an enclosure. Another approach involves correcting the measured values by subtracting the indenter displacement caused by thermal drift. In this case, during the unloading phase of the test (typically when the indenter load decreases to 10% of the maximum value), a pause of several seconds is introduced to measure the indenter's drift velocity. This velocity is then used in a drift correction model. The impact of temperature is also reduced by manufacturing critical parts of the device from materials with exceptionally low coefficients of thermal expansion.

Another source of uncertainty in nanoindentation studies is the penetration of the indenter into the sample under minimal load. The depth measurement can only begin after the first contact is made, which occurs at the minimal measurable load P_i, but the corresponding depth h_i (see Figure 5.4) is not yet known. However, it must be added to the measured maximum depth h_{max} so that the actual depth is $h = h_{max} + h_i$. An approximate value of the initial penetration h_i can be obtained by fitting the initial part of the $P = f(h)$ curve and extrapolating it to zero load. Since every indenter has a more or less rounded tip, the initial part of the indentation curve can be described by transforming equation (3.15) as:

$$h = \left(\frac{3}{4E\sqrt{R}}\right)^{\frac{2}{3}} \cdot P^{\frac{2}{3}} = kP^n \tag{5.2}$$

where k and n are constants. The value of h_i calculated in this manner is represented by the red curve in Figure 5.4. Conversely, extrapolation of the initial measurement points on the curve results in an incorrect value h'_i (green

curve in Figure 5.4). If the initial penetration depth constitutes too large a fraction of the total penetration, its calculation must be carried out with exceptional precision. Additionally, in the case of testing thin layers, if the initial penetration is too large, the indenter may penetrate the layer under investigation before the actual test begins, thus measuring the properties of the substrate instead.

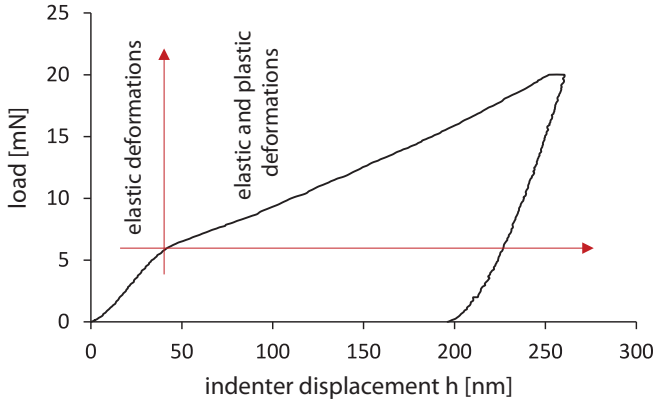

Fig. 5.2. Indentation curve for a ferrite grain in C45 steel after surface grinding to a depth of 8 μm, using a Berkovich indenter after three years of use

Source: Own work based on [51].

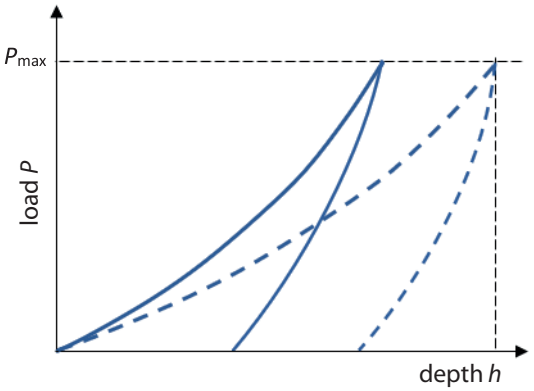

Fig. 5.3. Indentation curve without thermal drift (solid line) and with thermal drift (dashed line)

Source: Own elaboration based on [55].

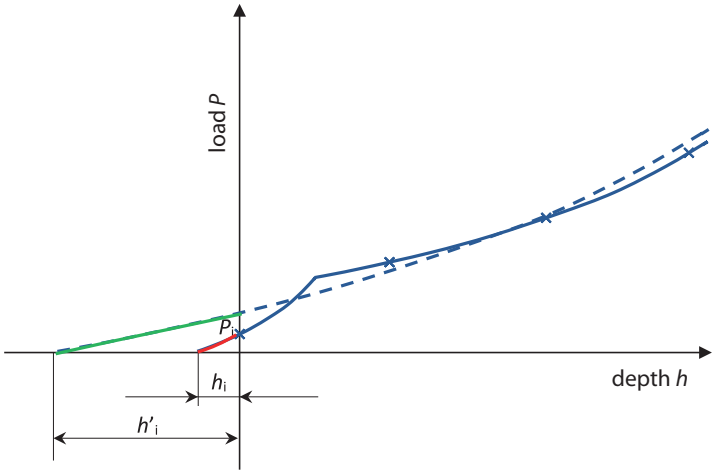

Fig. 5.4. Determination of initial penetration depth (schematic); the response of the indenter at low loads was influenced by a thin hard oxide layer on the surface; P_i – initial load, h_i – initial penetration depth calculated according to equation (5.2) (red curve), h'_i – initial depth obtained by extrapolation of measured depths (crosses) without considering the surface layer (green curve)

Source: Own elaboration based on [57].

5.1. Stresses and Strains in the Material During the Indentation Test

Over several decades, various studies [58–63] have attempted to describe the stresses and strains occurring during indentation tests to obtain $P = f(h)$ curves during the loading phase (see Fig. 5.1) and to correlate these curves with the stress-strain curves obtained from uniaxial compression tests. One of the earliest studies aimed at correlating the material's response to spherical indentation with uniaxial compression tests is attributed to Tabor [64], who assumed that the mean contact pressure (the load divided by the projected area of the indentation after unloading—the green area in Fig. 4.2) is proportional to the "representative" flow stress of the material under compression, and the corresponding "representative" strain is proportional to a/R. Tabor was able to experimentally correlate the measured values of indentation stress and strain in annealed copper and mild steel using a spherical indenter with the stress and strain measurements under uniaxial compression conditions for the same metals. Specifically, Tabor demonstrated that the mean contact pressure (p_m) scaled by a factor of 2.8 (on the plot $p_m = f(a/R)$ provides an excellent fit to the stress-strain curves under compression [31]. The factor of 2.8 was defined as the "constrain factor" C, intended to capture the effect of the higher hydrostatic stress (under the indenter) characteristic of the indentation test. Despite the remarkable correlation between material hardness, which was defined similarly to Meyer's, and the yield strength of the material observed in Tabor's experiment, the definition of indentation strain based on a/R has no known physical significance. It is also important to note that in Tabor's approach, the contact radius a was only estimated by measuring the indentation after unloading, and thus was not identical to the contact radius from Hertzian theory [65] (equation (3.19)), which applies to the loaded material. Tabor's original approach is also very labor-intensive, as each indentation test provides only one point on the $P = f(h)$ curve. During indentation testing, plastic deformation of the characterized material typically occurs due to the initiation of slip under the influence of shear stresses. The maximum shear stress in the elastic field of the contact stresses for a spherical indenter occurs beneath the surface along the axis of symmetry, and it is there that the plastic deformation zone begins to develop (Fig. 5.5). As the load increases, the zone encompassing the plasticized material also increases until the size of this zone matches the contact geometry, and the mean pressure p_m reaches a constant value. For a spherical indenter, if the mean pressure p_m does not exceed 110% of the yield strength of the characterized material ($p_m < 1.1R_e$), only elastic deformation of the substrate material occurs (Fig. 5.6a). When the mean stresses are greater than $1.1R_e$ but do not exceed $C \cdot R_e$, where C is the aforementioned "constrain factor," whose value depends on the material and the geometry of the indenter, plastic deformation of the material occurs beneath the surface, but it is confined by the surrounding elastic material (Fig. 5.6b).

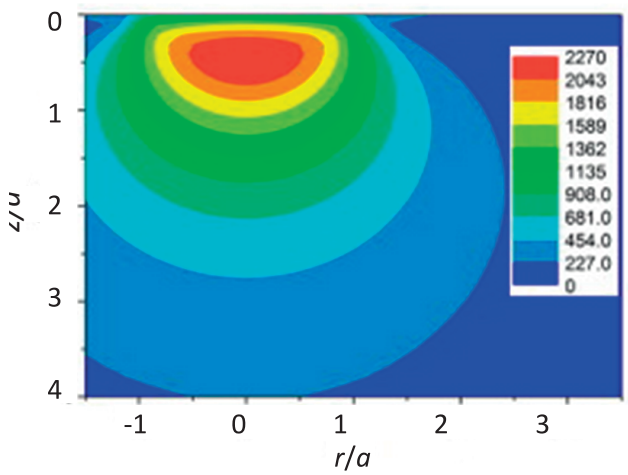

Fig. 5.5. Contour plot of von Mises stresses [MPa] for the contact between a spherical indenter and a flat substrate

Source: own work based on [66].

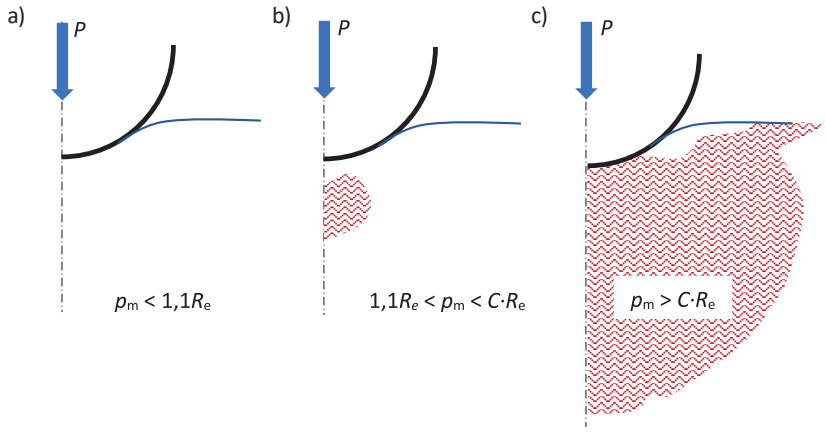

Fig. 5.6. Distribution of material deformations under a spherical indenter during the indentation test depending on the magnitude of average pressures: a) only elastic deformations; b) small plastic deformation zone; c) well-developed plastic deformation zone

Source: own work based on [66].

However, when the average pressures exceed the value of $C\,R_e$, the plastic zone extends to the surface of the sample and continues to grow, so that the contact surface of the indentation

increases at a rate that results in only a slight or no increase in average pressure with further increases in indenter load (Fig. 5.6c). Figure 5.7 illustrates the impact of average pressures on the deformations that occur during the indentation of a spherical indenter in Tabor's test.

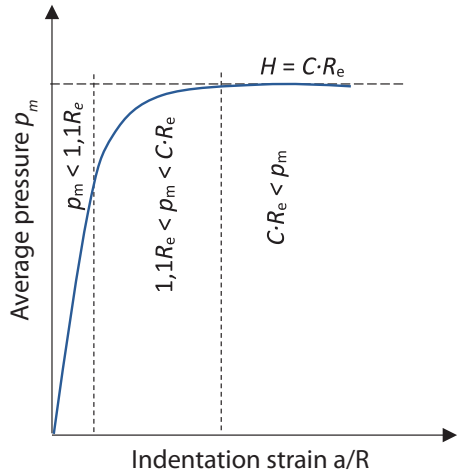

Fig. 5.7. Correlation between average pressures and deformations during the indentation of a spherical indenter in Tabor's test

Source: Own study based on [66].

For indenters with a sharp apex angle, the stress distribution differs from that of spherical indenters. In this case, the stresses in the material around the indenter, where there is no rounding of the apex angle, reach maximum values at the apex of the indentation, as illustrated in Fig. 5.8.

The indentation test can be applied to measure the hardness of even brittle materials due to the localized nature of the stress field generated in the material during the test. The stresses beneath the indenter are constrained by the elastically deformed material, allowing the achievement of shear stress levels at which plastic flow of the material can occur without fracturing (as it might in uniaxial tension or compression tests). The constraint factor C relates the hardness H *of* the material to its yield strength R_e:

$$H = C \cdot R_e \tag{5.3}$$

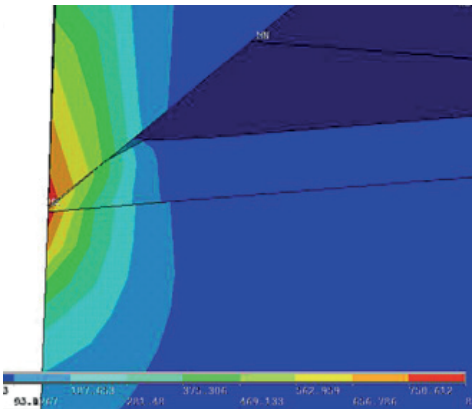

Fig. 5.8. Stress distribution in an indenter with an apex angle and in the material characterized by the indentation test. The figure presents the stress distribution in the indenter and in the coated substrate, where the coating consists of a different material.

Source: Own work based on [67].

In the 1950s, Tabor [31] demonstrated that $C \approx 3$ for most metals, i.e., for materials characterized by a high E/H ratio. However, for brittle materials such as ceramics, which exhibit a low E/H ratio, the coefficient C is less than 3. The reason why the mean pressures p_m do not increase despite an increase in the applied load P and the corresponding deformation a/R can be explained by Johnson's model [5, 20, 68] of expanding indentation during an indentation test. This model was developed by extending Hill's theory [69] of expanding cylindrical or spherical indentation in elastic-plastic materials to ensure consistency between the volume of material displaced by the indenter and the volume occupied by the elastically deformed material. Johnson's theory of rigid, perfectly plastic solids predicts that the pressures during an indentation test using pyramidal or conical indenters depend only on the geometry of the indenter and the yield strength of the material. In cases where the indenter tip is rounded or for materials with a low E/R_e ratio, the material under the indenter forms a hydrostatic core that is displaced by the moving indenter, approximately through radial expansion, into a zone of plastic deformation, which is, in turn, surrounded by elastically deformed material (see Fig. 5.9).

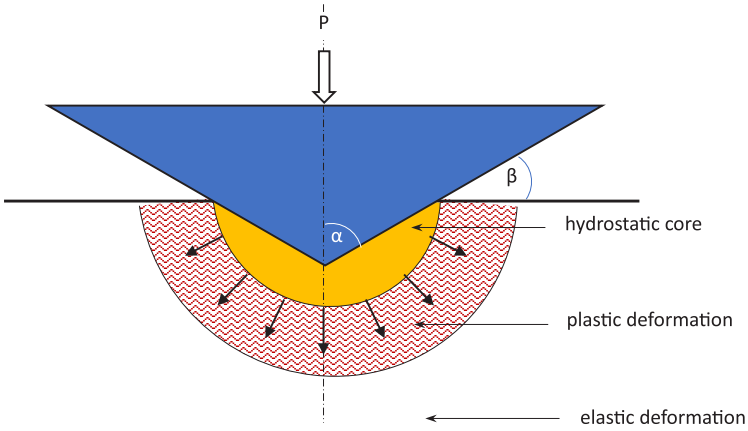

Fig. 5.9. Schematic representation of Johnson's model for expanding material indentation during an indentation test

Source: Own work based on [68].

Under these circumstances, the mean pressures fall below the value of R_e. In such cases, measurements of mean pressures for different indenter geometries show a correlation with the E/R_e parameter and the angle β of the indenter's inclination to the surface at the edge of the indentation:

$$\frac{p_m}{R_e} = \frac{2}{3}\left[2 + \ln\left(\frac{(E/R_e)\mathrm{ctg}\alpha + 4(1-2\nu)}{6(1-\nu)}\right)\right] \tag{5.4}$$

The parameter E/R_e can thus be interpreted as the ratio of deformation imposed by the indenter to the plastic deformation of the material. If, in equation (5.4), the average pressures are assumed to be equal to hardness H, then the quotient p_m/R_e equals C. For example, if E and H are known, R_e can be calculated using equation (5.4). Johnson's

model assumes that the plastic zone is hemispherical, which is generally true for high values of E/H. For low E/H values, the shape of the plastic zone becomes more spherical.

5.2. Pile up Effect

In subsection 4.5, the types of indentation profiles classified by Knoop are described. Hertz's theory and other models assume that the indentation edge in the material during the indentation test is recessed relative to the material's surface, as Knoop described for a type C profile (see Fig. 4.6). However, it sometimes happens that after the indentation test, the edge of the indentation bulges out (type A profile). This effect is referred to in the literature as "pile up." In such cases, the actual contact area is larger than the values assumed by the models. Without correcting for the pile-up effect, the calculated hardness and elastic modulus are higher than the actual values. The occurrence of the pile-up effect is influenced by the ratio of the elastic modulus to the yield strength of the material E/R_e, the material's tendency for strain hardening, and the shape of the indenter. The pile-up effect around sharp indenters is typical for materials with a high E/R_e ratio that do not undergo strain hardening. Examples include relatively soft metals that have been cold-worked. For instance, Knoop observed this effect in cold-rolled copper. Figure 5.10 shows an example of the pile-up effect for a thin gold layer. In materials with low hardness and a high E/R_e ratio but capable of strain hardening, the pile-up effect is not observed because the low hardness of the material results in a relatively large plastic zone during indentation, meaning a large volume of material around the indenter must be displaced through plastic flow toward the surface (Fig. 5.9). However, the intensively deformed surface layer around the indenter strain-hardens and becomes harder, which limits upward material flow and forces it to flow in directions with less strain hardening. In hard and highly elastic materials, such as glass and ceramics, where the E/H ratio is lower, the size of the plastic zone is small, and the volume of material displaced by the indenter can be accommodated by elastic deformations of the material surrounding the plastically deformed zone. In this case, the pile-up effect is also not observed. The error in calculating the contact area, leading to incorrect calculation of the material's hardness or stiffness (the method of calculating hardness and stiffness in an indentation test will be described in subsection 5.3), for materials exhibiting the pile-up effect can be as high as 60% [71]. For the elastic modulus, the error is lower but can still reach several tens of percent, owing to the role of the contact area A in the equation used to calculate the material's stiffness. The situation with sharp-angle indenters has been studied by comparing measured values of h_c and $A(h)$ (subsection 3.4) with values obtained through direct imaging of indentations [72] and by finite element modeling [73, 74]. Several conclusions can be drawn from these studies. First, the pile-up effect can be expected for materials where the E/H ratio is at least 100. Second, the stress field around a sharp-angle indenter is similar to the stress distribution in the indenter itself, as shown in Fig. 5.8, and the degree of stress concentration at the tip of the indentation does not depend on the penetration depth. A simple metric to assess a material's tendency to exhibit the pile-up effect is the ratio of the residual indentation depth after unloading h_r to the maximum indentation depth under load h_{max}, h_r/h_{max} (see Fig. 5.1). The pile-up effect is pronounced if the h_r/h_{max} value is close to 1.0, and the material exhibits minimal strain hardening. If the h_r/h_{max} value is less than 0.7, no or very little pile-up effect is observed, regardless of whether the material undergoes strain hardening or not [73, 75].

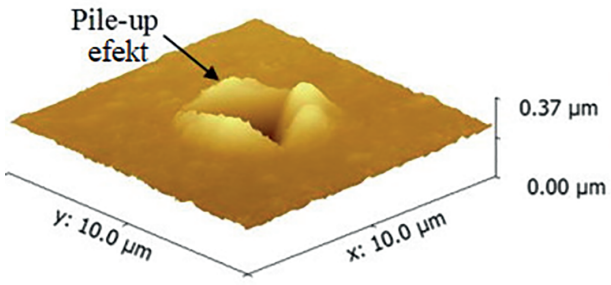

Fig. 5.10. AFM image of a thin gold layer obtained under a 10 mN load

Source: Own work based on [70].

For spherical indenters, the occurrence of the pile-up effect is more complex. The average contact pressure p_m, as well as the stresses and strains, increase with the depth of penetration of the indenter into the material. The "representative" strain is usually expressed as the ratio of the contact radius a to the indenter radius R (as discussed in subsection 5.1). At relatively low loads, the material deforms elastically only and sinks around the indenter (see

Fig. 3.1). Plastic flow of the material begins when the average pressures reach $p_m = 1.1R_e$, but Hertz's equation describing the load as a function of displacement (Equation 3.15) holds approximately up to average pressures of $p_m = 1.6R_e$. At such values of average pressures, the volume of plastically deformed material under the indenter becomes so large that the material around the indenter begins to be pushed upward. It has also been observed that the tendency for the pile-up effect increases with an increase in the ratio of E/R_e and with an increase in the relative depth of indenter penetration h_{max}/R. Finite element method studies [76] have shown that for a material that does not undergo strain hardening and has an E/R_e ratio of 200, the pile-up effect is negligible when the h_{max}/R value is less than 0.001 and noticeable when this ratio exceeds 0.01. For materials exhibiting strain hardening, the tendency for pile-up is reduced. The pile-up effect can also occur when a spherical indenter penetrates a soft coating deposited on a hard substrate. In such cases, the coating material is displaced upward from the contact zone around the indenter more than in a homogeneous sample [57]. The opposite scenario occurs in materials that densify under high compressive stresses. In this situation, the surface sinking is more pronounced than in conventional elastoplastic materials. Pile-up and sink-in effects influence the shape of the indentation left after unloading, as shown in Fig. 5.11.

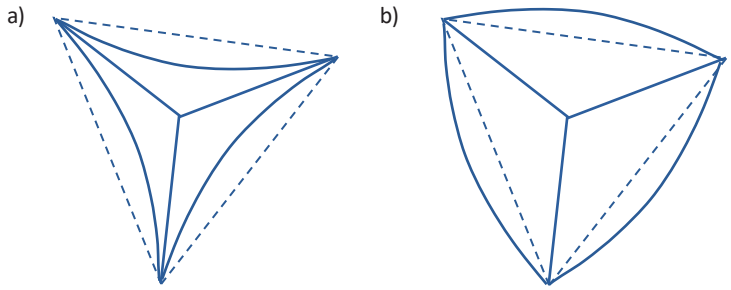

Fig. 5.11. Shape of the indentation after unloading the Berkovich indenter in a material exhibiting the sink-in effect (a) and the pile-up effect (b)

Source: Own work.

5.3. Determining Material Hardness and Stiffness

The hardness of a material in the indentation test is determined differently than in the methods described in Chapter 4. There is a similarity between determining hardness in the indentation test and the Martens hardness test, in that both the Martens method and the indentation method measure the contact area for the indenter under maximum load, considering both the elastic and plastic deformation of the material during the hardness measurement. The differences between these methods arise from the fact that in the Martens method, the contact area of the indenter with the material reflects the lateral surface area of the indenter without accounting for the sink-in or pile-up effects, whereas in the indentation method, the projected area on the plane parallel to the material's surface is considered, taking into account the effects at the edges of the deformed material (see Figs. 4.4, 5.12). Nanoindentation is conventionally performed using equipment that records the load and displacement of the indenter during the indentation process. The material's responses during both the loading of the indenter and the unloading process are recorded in the form of a load-displacement curve $P = f(h)$. The analysis of the load-displacement curve allows for the calculation of the elastic modulus E and hardness H without the need for direct measurement of the contact area A. The elastic response of the material during the unloading phase, when the material undergoes elastic deformation, is the foundation of this technique. As shown in Fig. 5.12, the contact area A depends on the geometry of the indenter and the contact depth h_c. Subsection 3.4 presents the relationships between the contact depth h_c and the contact area for different indenter geometries. During the indentation test, it is not possible to directly measure the contact depth h_c however, it can be calculated using Sneddon's equations. From Fig. 5.12, it can be seen that $h_c = h_{max} - h_a$.

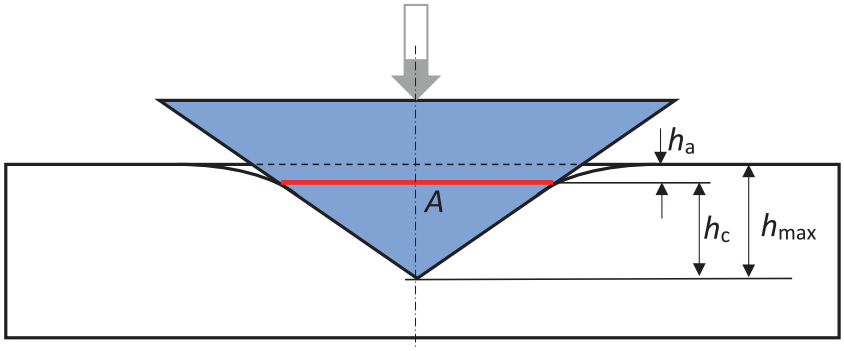

Fig. 5.12. Schematic of the indenter's position at maximum load. The area A needed for hardness determination is marked in red
Source: Own elaboration based on [28].

The maximum indentation depth h_{max} can be directly read from the indentation test, while the depth h_a is determined from equation (3.78) by substituting $r = a$:

$$h(a) = h_a = \left(\frac{\pi}{2} - \frac{a}{a}\right) a \cdot \mathrm{ctg}\alpha' \tag{5.5}$$

On the other hand, if $r = 0$ is substituted into equation (3.78), the displacement depth h_e is obtained (see Figure 3.10), which is given by:

$$h(0) = h_e = \frac{\pi}{2} a \cdot \mathrm{ctg}\alpha' \tag{5.6}$$

By rearranging equation (5.6), it can be written as:

$$a \cdot \mathrm{ctg}\alpha' = \frac{2h_e}{\pi} \tag{5.7}$$

Substituting equation (5.7) into equation (5.5), we obtain:

$$h_a = \left(\frac{\pi}{2} - 1\right)\frac{2h_e}{\pi} = \frac{\pi-2}{\pi} h_e \tag{5.8}$$

The depth h_e can be read from the indentation curve as $h_e = h_{max} - h_r$ (see Fig. 5.1) or calculated using the second Sneddon's equation, which describes the relationship between the load P and the indentation depth h_e (equation (3.77)). If equation (3.77) is differentiated with respect to h_e, we obtain:

$$\frac{dP}{dh_e} = 2\frac{2}{\pi} E^* h_e \cdot \mathrm{tg}\alpha' \tag{5.9}$$

Multiplying and dividing the right-hand side of equation (5.9) by h_e, we obtain:

$$\frac{dP}{dh_e} = 2\frac{\frac{2}{\pi}E^* {h_e}^2 \cdot \mathrm{tg}\alpha'}{h_e} = \frac{2P}{h_e} \tag{5.10}$$

It follows that:

$$h_e = \frac{2P}{dP/dh_e} \tag{5.11}$$

Substituting equation (5.11) into equation (5.8), we can write:

$$h_a = \frac{\pi-2}{\pi} \cdot \frac{2P}{dP/dh_e}$$

Having h_a,we can calculate h_c:

$$h_c = h_{max} - \frac{\pi-2}{\pi} \cdot \frac{2P}{dP/dh_e} \tag{5.12}$$

From equation (5.12), it follows that to calculate the depth h_c, it is sufficient to know h_{max}, P and dP/dh_e (the tangent to the unloading curve at maximum load) or, alternatively, h_e. All these values are obtained from the indentation test. Knowing the depth h_c allows for determining the contact area A and the hardness of the tested material as $H = P/A$. Equation (5.12) can also be written as:

$$h_c = h_{max} - \varepsilon \frac{P}{dP/dh_e} \tag{5.13}$$

where ε is a constant *dependent* on the geometry of the indenter. For a conical indenter, it is given by:

$$\varepsilon = \frac{(\pi-2)2}{\pi} = 0{,}72 \tag{5.14}$$

However, considering that every indenter with an apex angle has a rounded tip, a paraboloid of revolution (as shown in Fig. 5.13) is a better approximation for the actual shapes of indenters than a cone.

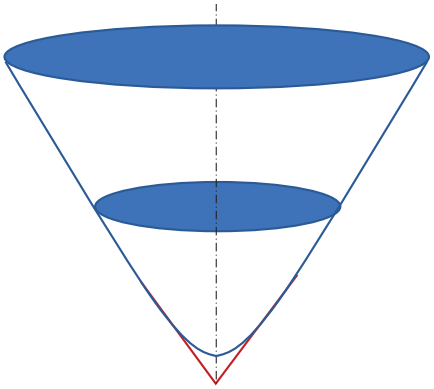

Fig. 5.13. Paraboloid of Revolution

Source: Own elaboration.

Oliver and Pharr [71] reported that for a paraboloid of revolution, the constant ε is 0.75. The method used to determine the depth h_c using equation (5.13) is commonly referred to in the literature as the Oliver-Pharr method.

Often in the indentation test, the stiffness of the material is also determined. To do this, equation (5.6) is substituted into equation (5.9), yielding:

$$\frac{dP}{dh_e} = 2\frac{2}{\pi}E^*\frac{\pi}{2}a \cdot \mathrm{ctg}\alpha' \cdot \mathrm{tg}\alpha' = 2E^*a \tag{5.15}$$

By rearranging equation (5.15), the reduced modulus E^* can be determined as follows:

$$E^* = \frac{dP}{dh_e}\frac{1}{2}\frac{1}{a} \tag{5.16}$$

And since $A = \pi a^2$, the stiffness of the system is given by:

$$E^* = \frac{dP}{dh_e}\frac{1}{2}\frac{\sqrt{\pi}}{\sqrt{A}} \tag{5.17}$$

The stiffness E_1 of the tested material can be determined from equation (3.17), knowing the stiffness E_2 of the indenter material, as well as the Poisson's ratios for both the indenter material and the tested material. For diamond indenters, a stiffness of 1050 GPa and a Poisson's ratio of 0.07 are typically assumed.

Another method for determining the contact depth h_c was proposed by Field and Swain [77]. This method uses the elastic contact equations derived by Hertz ((3.11) and (3.15)) and the load data on the indenter. In equation (3.15), $\delta = h_e$. Originally, this method was developed for spherical indenters but can also be applied to other indenter shapes. In equation (3.15), for $r = 0$, $h = h_e$, that is:

$$h_e = \frac{1}{E^*} \cdot \frac{3}{4} \cdot \frac{P}{a} \tag{5.18}$$

In turn, for $r = a$, $h = h_a$, that is:

$$h_a = \frac{1}{E^*} \cdot \frac{3}{4} \cdot \frac{P}{a} \cdot \frac{1}{2} \tag{5.19}$$

From equations (5.18) and (5.19), it follows that $h_a = 1/2h_e$, and since $h_c = h_{max} - h_a$, we can further write $h_c = h_{max} - 1/2h_e$. And because $h_e = h_{max} - h_r$, finally:

$$h_c = \frac{h_{max}+h_r}{2} \tag{5.20}$$

To determine h_r, Field and Swain used the following method. They selected the point of maximum load on the unloading curve with coordinates (P_{max}, h_{max}) and a second point S with coordinates (P_s i h_s) (see Fig. 5.14). Then, using equation (3.15), they calculated the elastic displacements for these points:

$$h_e = h_{max} - h_r = \left[\left(\frac{3}{4E^*}\right)^{\frac{2}{3}} \frac{1}{\sqrt[3]{R}}\right] \sqrt[3]{P_{max}^2} \tag{5.21}$$

$$h_s - h_r = \left[\left(\frac{3}{4E^*}\right)^{\frac{2}{3}} \frac{1}{\sqrt[3]{R}}\right] \sqrt[3]{P_s^2} \tag{5.22}$$

From equations (5.21) and (5.22), it follows that:

$$\frac{h_{max}-h_r}{h_s-h_r} = \left(\frac{P_{max}}{P_s}\right)^{\frac{2}{3}} \tag{5.23}$$

Solving equation (5.23) allows for the determination of h_r:

$$h_r = \frac{h_s\left(\frac{P_{max}}{P_s}\right)^{2/3} - h_{max}}{\left(\frac{P_{max}}{P_s}\right)^{2/3} - 1} \tag{5.24}$$

which, when substituted into equation (5.23), allows for the determination of the contact depth h_c.

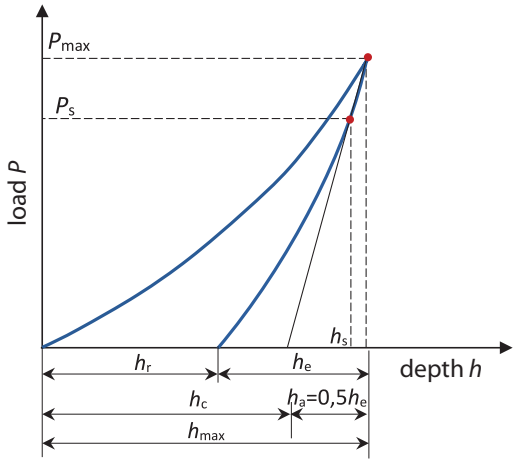

Fig. 5.14. Schematic representation of the Field and Swain method for determining the contact depth h_c

Source: Own work based on [77].

The depth h_c can also be determined using energy methods. The area under the loading curve represents the total work U_t done by the indenter, which is needed for both the elastic and plastic deformation of the material, while the area under the unloading curve represents the work U_s done by the material for its elastic deformation during unloading. The area enclosed between the loading and unloading curves corresponds to the work U_p done by the indenter for the plastic deformation of the material during loading (Figure 5.15). The loading curve can be expressed by the equation

$$P = C_p h^m \tag{5.25}$$

and the unloading curve by the equation:

$$P = C_e(h - h_r)^m \tag{5.26}$$

where C_p, C_e and m are constants depending on the material and the shape of the indenter. For a conical indenter, $m = 2$, while the constant C_p (for elastoplastic deformation) is given by:

$$C_p = \left\{\frac{1}{\sqrt{\pi H \mathrm{tg}^2\alpha}} + \left[\frac{2(\pi-2)}{\pi}\right]\sqrt{\frac{\pi}{4}}\frac{\sqrt{H}}{E^*}\right\}^{-2} \tag{5.27}$$

and the constant C_e for the elastic response of the material during unloading is:

$$C_e = \frac{2}{\pi} E^* \mathrm{tg}\alpha \tag{5.28}$$

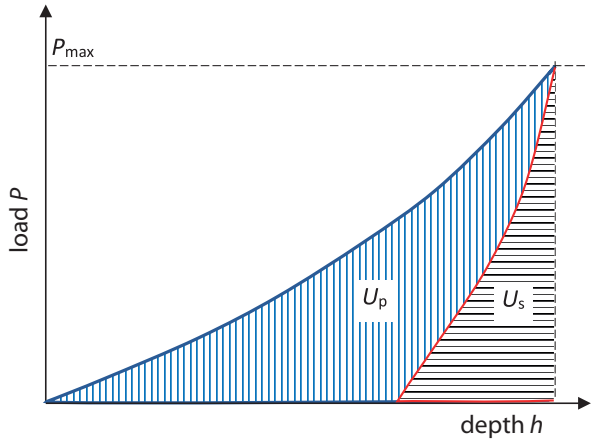

Fig. 5.15. Surface areas under the loading and unloading curves of the indenter corresponding to the energy of plastic deformation U_p and elastic deformation U_e of the material

Source: Own study based on [77].

Since at the maximum load both curves described by equations (5.25) and (5.26) have the same value, it can be written as:

$$P_{\max} = C_{\mathrm{p}} {h_{\max}}^2 = C_{\mathrm{e}}(h_{\max} - h_{\mathrm{r}})^m \tag{5.29}$$

For the maximum load P_{max} and $m = 2$, by integrating equation (5.25) with respect to h, the equation describing the energy U_t is obtained as:

$$U_{\mathrm{t}} = \frac{1}{3} C_{\mathrm{p}} h_{\max}^2 \tag{5.30}$$

On the other hand, by integrating equation (5.26), the energy U_e is obtained as:

$$U_{\mathrm{e}} = \int_{h_{\mathrm{r}}}^{h_{\max}} C_{\mathrm{e}}(h - h_{\mathrm{r}})^m dh = C_{\mathrm{e}} \frac{(h_{\max} - h_{\mathrm{r}})^{m+1}}{m+1} \tag{5.31}$$

Further, it can be written that:

$$U_{\mathrm{p}} = U_{\mathrm{t}} - U_{\mathrm{e}} = \frac{1}{3} C_{\mathrm{p}} h_{\max}^2 - C_{\mathrm{e}} \frac{(h_{\max} - h_{\mathrm{r}})^{m+1}}{m+1} \tag{5.32}$$

Using equations (5.30) and (5.32), it can be written as:

$$\frac{U_{\mathrm{p}}}{U_{\mathrm{t}}} = 1 - \frac{3}{m+1}\left(1 - \frac{h_{\mathrm{r}}}{h_{\max}}\right) \tag{5.33}$$

Computer simulations and experimental studies indicate that for a conical indenter with a half-apex angle of 70.3° (a substitute shape for the Berkovich indenter), the constant m takes a value of 1.36. Substituting this value into equation (5.33), we get:

$$\frac{U_{\mathrm{p}}}{U_{\mathrm{t}}} = 1{,}27\left(\frac{h_{\mathrm{r}}}{h_{\max}}\right) - 0{,}27 \tag{5.34}$$

Computer simulations also demonstrate that the following relationship occurs:

$$\frac{H}{E^*} = \kappa \frac{U_{\mathrm{e}}}{U_{\mathrm{t}}} \tag{5.35}$$

Similarly, for a cone with a half-apex angle of 70.3°, κ = 5.3. Substituting H = P/A into equation (5.35) and transforming it, a relationship describing the contact area A can be obtained:

$$A = \frac{1}{\kappa^2} \frac{4}{\pi} P_{\max}^2 \left(\frac{dh}{dP}\right)^2 \left(\frac{U_{\mathrm{t}}}{U_{\mathrm{e}}}\right)^2 \tag{5.36}$$

Having determined the contact area, by substituting A into equation (5.17), both hardness H and the reduced modulus E^*, can be calculated:

$$E^* = \kappa \frac{\pi}{4} \left(\frac{dP}{dh}\right)^2 \frac{U_{\mathrm{e}}}{U_{\mathrm{t}}} \frac{1}{P_{\max}} \tag{5.37}$$

$$H = \kappa^2 \frac{\pi}{4} \left(\frac{dP}{dh}\right)^2 \left(\frac{U_e}{U_t}\right)^2 \frac{1}{P_{max}} \tag{5.38}$$

As follows from equations (5.37) and (5.38), to determine the reduced contact stiffness and hardness, the values U_e/U_t, dP/dh and P_{max}, are needed, which are determined in the indentation experiment.

5.4. Size Effect and Determining Dislocation Density

During the indentation test, small maximum indenter loads are often applied. This is typically the case when determining the hardness or stiffness of thin coatings or diffusion layers. During the indentation test, the crystalline material undergoes displacements and rotations due to the pressing of the indenter, replicating the shape of the indenter. Sharp indenters, with an apex angle, generate plastic deformations in the material almost immediately upon contact. In order for the material to take on the shape of the indenter, dislocations must form, which allow for plastic deformation. These additional dislocations generated during the indentation test combine with the pre-existing dislocations in the crystalline material, increasing its hardness. This effect is referred to in the literature as the "indentation size effect" (ISE), and the additional dislocations are known as geometrically necessary dislocations (GND). To determine the actual hardness of the material (macroscopic hardness), it is necessary to calculate the GND dislocation density and subtract it from the total dislocation number to eliminate the influence of the additional dislocations on the obtained hardness value. To determine the GND dislocation density (ρ_{GND}), the total length of dislocation loops (λ) and the volume of the plasticized material (V) around the indenter must be known; then, it can be expressed as $\rho_{GND} = \lambda/V$ [78]. For a cone-shaped indenter and materials with high elasticity, i.e., high H/E (metals and their alloys), the plasticized zone has the shape of a hemisphere. Its volume can be determined by knowing the radius of the plasticized zone a_{pz} (Fig. 5.16):

$$V = (2\pi \cdot a^3{}_{pz})/3 \tag{5.39}$$

In turn, the total length of the dislocation loops (λ) can be determined if the contact radius a_c is known:

$$\lambda = (\pi h_c \cdot a_c)/b \tag{5.40}$$

where h_c is the contact depth of the indenter with the material, and b is the scalar magnitude of the Burgers vector. Using equations (5.39) and (5.40), the equation describing the GND dislocation density can be written as:

$$\rho_{GND} = \frac{3}{2} \cdot \frac{h_c \cdot a_c}{b \cdot a_{pz}^3} \tag{5.41}$$

If the coefficient $f = a_{pz}/a_c$ is assumed, equation (5.41) can be written as:

$$\rho_{GND} = \frac{3}{2} \cdot \frac{h_c \cdot a_c}{b \cdot f^3 a_c^3} = \frac{3}{2} \cdot \frac{1}{f^3} \cdot \frac{h_c}{b \cdot a_c^2} \tag{5.42}$$

If the numerator and denominator of equation (5.42) are further multiplied by h_c, the equation can be written in the following form:

$$\rho_{GND} = \frac{3}{2} \cdot \frac{1}{f^3} \cdot \frac{h_c^2}{b \cdot h_c \cdot a_c^2} \tag{5.43}$$

Since $h_c/a_c = ctg\theta$ (see Fig. 5.16), the final equation is:

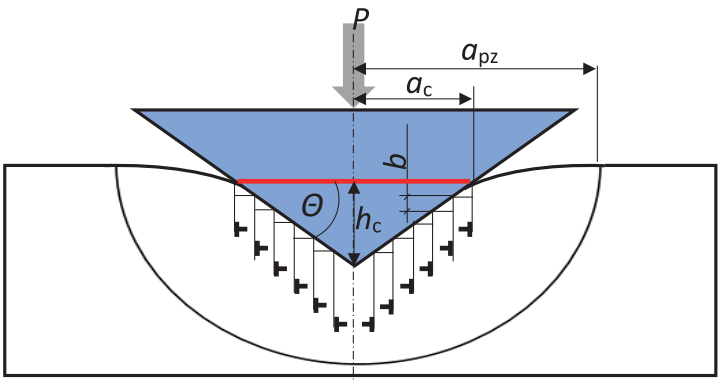

Fig. 5.16. Diagram of the plasticized material zone under the indenter during the indentation test

Source: Own study.

$$\rho_{GND} = \frac{3}{2} \cdot \frac{1}{f^3} \cdot \frac{\mathrm{tg}^2\theta}{bh_c} \tag{5.44}$$

where θ is the angle between the cone's generatrix and the surface of the sample. Although the analysis presented above applies to a cone-shaped indenter, similar relationships are obtained for indenters of other shapes. As derived from equation (5.44), the density of geometrically necessary dislocations (GND) generated in the material during the indentation test depends on the coefficient f and the contact depth h_c.The coefficient f as described earlier, is dependent on the size of the plastic zone under the indenter. For different materials, this zone varies in size, but for most metals and alloys, the radius of the material's plastic zone a_{pz} is larger than the contact radius a_c. In such cases, the coefficient f is greater than 1; for instance, for soft materials like ferrite, the coefficient f is approximately 2.2 [20]. The second variable influencing the GND density is the contact depth. The smaller the contact depth, the greater the density of generated dislocations, which in turn increases the hardness and stiffness values. Although GND dislocations form continuously during the indentation test, their effect on the measurement results diminishes as the indenter depth increases. Hence, the smaller the maximum load applied to the non is known as the "indentation size effect." Other factors also influence the generation of indenter during the indentation test, the greater the material hardness obtained. This phenome GND dislocations. For example, crystal anisotropy increases the GND density [79]. In addition to GND dislocation density and statistically stored dislocations (SSD) that formed during the material's production, the measured hardness is also influenced by factors such as internal friction stresses H_{fr} (Peierls stresses) [80, 81] and solution hardening H_{ss} [82]. The equation describing the material's hardness measured during the indentation test can be expressed as follows:

$$H_{ISE} = H_{fr} + H_{ss} + MC\alpha Gb\sqrt{\rho_{GDN} + \rho_{SSD}} \tag{5.45}$$

where: M is the Taylor factor, relating shear stresses to normal stresses in uniaxial deformation, C is the constraint factor, converting the complex stress state under the indenter to an equivalent uniaxial stress state (subsection 5.1), α is a coefficient dependent on the dislocation structure, G is the shear modulus, and b is the magnitude of the Burgers vector. The relationship between the macroscopic hardness of the material H_0 (without considering the indentation size effect, ISE) and the statistically stored dislocation density (SSD) is described by Taylor's equation [83]:

$$H_0 = MC\alpha Gb \cdot \sqrt{\rho_{SSD}} \tag{5.46}$$

The scale effect is more pronounced in the case of soft crystalline materials. This is due to the greater strain gradient near the indenter in soft materials compared to harder ones (see Fig. 5.8). The increase in yield strength caused by the generation of geometrically necessary dislocations (GND) becomes more noticeable as the indentation depth decreases and strain gradients increase. The presence of the scale effect, resulting from the existence of GNDs, also depends on the availability of sufficient dislocation sources in the material. For example, Lilleodden et al. [84], based on numerical simulations of gold indentation conducted on grains with a total of 79 boundaries, found that homogeneous dislocation nucleation occurs in perfect crystals during indentation, whereas preferential dislocation emission from the grain boundary occurs when indentation takes place near the boundary.

5.5. Material Creep and Determining Dislocation Mobility

As mentioned in subsection 5.1, the analysis of the $P = f(h)$ curve during the indentation test assumes that for sharp indenters (those with a vertex angle), plastic deformation of the material occurs almost immediately after contact with the indenter due to the high concentration of stresses (above the yield strength) in the material near the indenter's vertex. This model assumes that the material behaves in an elastoplastic manner, and the material deformation does not depend on the rate of applied load (time). However, for many materials during the indentation test, time-dependent creep of the material may occur, manifesting as displacement of the indenter under constant load. In the indentation test, plastic deformations caused by stresses exceeding the yield strength should be considered separately from deformations caused by creep induced by stresses below the material's yield strength. The amount of plastic deformation caused by material creep depends on the magnitude of applied loads, the material's temperature, and the duration of stress application.

Materials that undergo elastic deformation, and whose plastic deformation is not time-dependent, are called elastoplastic materials. Materials that deform elastically and exhibit time-dependent plastic deformation are called viscoelastic, while materials that do not deform elastically and whose plastic deformation is time-dependent are

called viscoplastic. The time-dependent properties of materials are analyzed in terms of mechanical models, such as the three-element Voigt model and the two-element Maxwell model (Fig. 5.17).

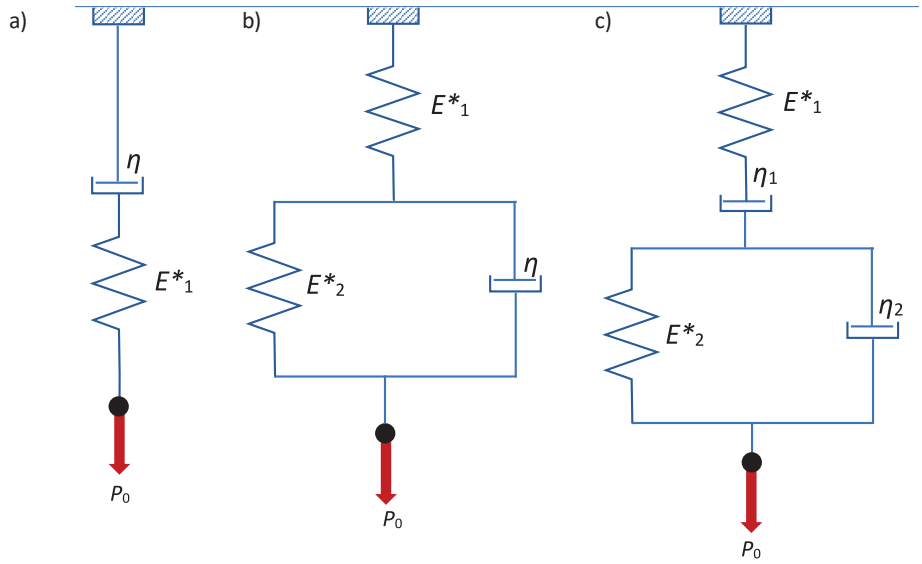

Fig. 5.17. Maxwell model representing a viscoelastic solid (steady-state creep) (a); three-element Voigt spring for a viscoelastic solid (delayed elastic response) (b); and a combination of Maxwell and Voigt models (c)

Source: own work based on [85].

In nanoindentation testing, the recorded displacement of the indenter is thus the sum of the displacement resulting from the elastoplastic properties of the material and from creep, both viscoelastic (for viscoelastic materials) and viscoplastic (for viscoplastic materials). For a spherical indenter with a radius R and for a constant applied load P_0, the deformation for viscoelastic materials described by the Voigt model, with viscosity η, increases over time according to the equation [20] (Fig. 5.18a):

$$h^{3/2}(t) = \frac{3}{4}\frac{P_0}{\sqrt{R}}\left[\frac{1}{E_1^*} + \frac{1}{E_2^*}\left(1 - e^{-t\frac{E_2^*}{\eta}}\right)\right] \tag{5.47}$$

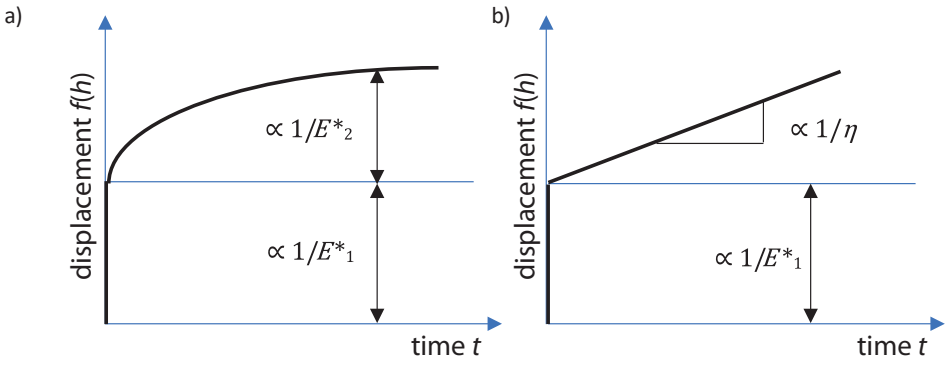

Fig. 5.18. Indenter displacement for a stepwise load increase for the Voigt model (a) and for the Maxwell model (b); $f(h) = h^2$ for a conical indenter and $f(h) = h^{3/2}$ for a spherical indenter

Source: Own study based on [85, 86].

The expression in square brackets in equation (5.47) describes the time response of the Voigt model to a stepwise applied load P_0. For viscoelastic materials described by the Maxwell model, the equation takes the form:

$$h^{3/2}(t) = \frac{3}{4}\frac{P_0}{\sqrt{R}}\left[\frac{1}{E_1^*} + \frac{1}{\eta}t\right] \tag{5.48}$$

In the case of using a conical indenter for viscoelastic materials described by the Voigt model, the material's response to a stepwise applied load takes the following form (Fig. 5.18a):

$$h^2(t) = \frac{\pi}{2} P_0 \mathrm{ctg}\alpha \left[\frac{1}{E_1^*} + \frac{1}{E_2^*} \left(1 - e^{-t\frac{E_2^*}{\eta}} \right) \right] \tag{5.49}$$

and for materials described by the Maxwell model, the equation takes the following form:

$$h^2(t) = \frac{\pi}{2} P_0 \mathrm{ctg}\alpha \left[\frac{1}{E_1^*} + \frac{1}{\eta} t \right] \tag{5.50}$$

To obtain the equations describing the displacement of a spherical indenter for materials modeled by a combination of the Maxwell and Voigt models (Fig. 5.17c), equations (5.47) and (5.48) must be combined, and for a conical indenter, equations (5.49) and (5.50) must be combined. For a spherical indenter, the resulting equation will be:

$$h^{3/2}(t) = \frac{3}{4} \frac{P_0}{\sqrt{R}} \left[\frac{1}{E_1^*} + \frac{1}{E_2^*} \left(1 - e^{-t\frac{E_2^*}{\eta_2}} \right) + \frac{1}{\eta_1} t \right] \tag{5.51}$$

and for a conical indenter, the equation will be:

$$h^2(t) = \frac{\pi}{2} P_0 \mathrm{ctg}\alpha \left[\frac{1}{E_1^*} + \frac{1}{E_2^*} \left(1 - e^{-t\frac{E_2^*}{\eta_2}} \right) + \frac{1}{\eta_1} t \right] \tag{5.52}$$

Equations (5.51) and (5.52) assume a sudden application of force to the indenter; however, in the indentation test, the load gradually increases from zero to the maximum load. In such cases, the superposition method [85] can be used. These equations also assume that as the load on the indenter increases, the contact radius with the material grows, but this is not always the case. More general equations describing this problem can be found in the work [86]. To obtain the values of E and η, equations (5.47)–(5.52) can be fitted to the experimentally obtained creep data. This approach is often used to determine material properties at elevated temperatures [87, 88].

In crystalline materials, creep is caused by the movement of dislocations within the crystal. The velocity of these dislocations can be determined using the indentation test by applying Orowan's equation [89]:

$$\frac{d\varepsilon}{dt} = \dot{\varepsilon} = v \cdot b \cdot \rho_{\mathrm{SSD}} \tag{5.53}$$

where $d\varepsilon/dt$ is the creep rate of the material during the dwell time at constant indenter load, v is the average velocity of dislocation movements, and b is the Burgers vector. Figure 5.19a shows the indentation curve for a CoCrWMo alloy, printed using selective laser melting (SLM), obtained with an indenter displacement rate of 200 mN/s. After reaching the maximum indenter load of 2 N, the load was held constant for 10 seconds (dwell time). During this time, the material exhibited creep, meaning the indenter continued to penetrate deeper into the material, from approximately 18,000 nm to 21,500 nm, despite the constant indenter load, as shown in Figure 5.19a. However, the rate of this displacement was not constant during this period. As shown in Figure 5.19b, during the first 6 seconds of constant load, the indenter moved into the material with a decreasing velocity (red curve). After 6 seconds, the creep proceeded at a constant rate of 0.0133 1/s (black curve). This rate, when substituted into equation (5.53), allows for the calculation of the average velocity of dislocations in the crystal, provided that the Burgers vector and dislocation density are known. It is important to note that the shape of the creep curve corresponds to the combination of Maxwell and Voigt models for the four-element model, as shown in Figure 5.17c.

5.6. Determining the Strain Hardening Coefficient of the Material

In a uniaxial tensile test of an ideally elastic-plastic material, as the stresses σ increase within the elastic range, the material's strain ε grows proportionally to the longitudinal elastic modulus E, i.e., $\sigma = E \cdot \varepsilon$. After the stress reaches a value equal to the yield strength R_e, the stress remains constant as the strain increases (see Fig. 5.20a). However, for many materials, such as annealed metals, once the stress reaches the yield strength, it does not remain constant but continues to increase with increasing strain (see Fig. 5.20b). This effect is associated with the phenomenon of strain hardening, which involves the accumulation of dislocations in the material and their mutual interactions, leading to reduced mobility. The average speed at which dislocations move can be calculated using Orowan's equation (5.53). The reduced mobility of dislocations, as well as their increased density, results in an increase in the hardness of the material and, consequently, its strengthening. In such strain-hardening materials, the correlation between strain and stress is described by an exponential function $\sigma = K \cdot \varepsilon^x$, which in a double logarithmic plot appears as a straight line with a slope equal to x. The exponent x is also referred to as the material's hardening coefficient. For

ideally elastic-plastic materials, the hardening coefficient equals zero. For metals exhibiting strain hardening, its value ranges between 0.1 and 0.5. The hardening coefficient is most easily determined in a uniaxial tensile test; however, this is a destructive method and may not always be suitable. In some cases, the coefficient x can be determined in an indentation test. As derived from Hertz theory, when a spherical indenter is pressed with small loads, the material undergoes elastic deformation, and the relationship between the load and the displacement of the indenter or the contact radius is described by equation (3.15). Further increases in load cause the material to deform plastically. The critical load P_c, at which the transition between elastic and plastic deformation occurs, happens when the average pressure exerted by the indenter equals the hardness [77]. In such a case, it can be expressed as:

$$P_c = \left(\frac{3}{4E^*}\right)^2 (\pi H)^3 R^2 \tag{5.54}$$

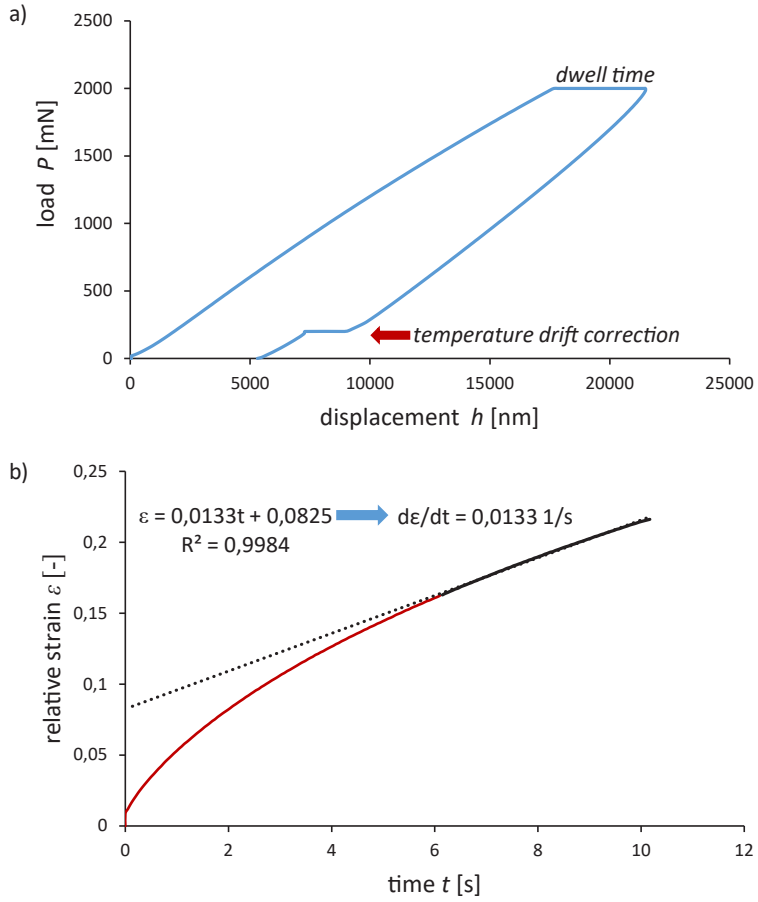

Fig. 5.19. Indentation curve for CoCrWMo alloy (a); visible correction for thermal drift for the unloading curve (after 90% of the maximum load is removed) and the creep curve (b)

Source: own work based on [87].

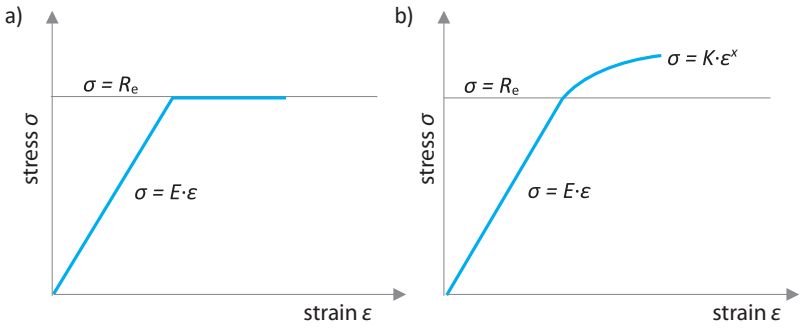

Fig. 5.20. The relationship between stress and strain in a uniaxial tensile test for ideally elastic-plastic materials (a) and materials exhibiting hardening (b)

Source: own work based on [77].

For the critical load, the critical contact radius can be determined, which is a function of the material's hardness:

$$a_c = \sqrt{\frac{P_c}{\pi H}} \tag{5.55}$$

After exceeding the critical load, it is assumed that there is no further increase in average pressures and thus in the material's hardness (see Fig. 5.7), and the contact is fully plastic. To calculate the contact radius for loads greater than the critical load P_t, the following relationship is used:

$$a = a_c \left(\frac{P_t}{P_c}\right)^{\frac{1}{2+x}} \tag{5.56}$$

From equations (5.54)–(5.56), it follows that by knowing the hardness and stiffness of the material, one can calculate the critical force P_c and the radius a_c, and from the indentation experiment conducted under the load P_t, the contact radius a can be determined, and thus the strain hardening coefficient x can be calculated.

An alternative method for determining the strain hardening coefficient is to use Meyer's work [30], which stated that the slope n of the line $logP$ =n $logd$ +log, where d is the diameter of the indentation obtained in the spherical indentation test (see equation (4.1), Fig. 4.2), and P is the load, is not sensitive to the indenter radius and is related to the material's strain hardening exponent x by the relationship:

$$n = x + 2 \tag{5.57}$$

In later studies, it was found that n ranges between 2 and 2.5, with the higher value corresponding to soft, annealed materials. In contrast, the lower strain hardening coefficient applies to harder materials. It is worth noting that Meyer established a lower limit of validity for his equation at deformations of $a/R = 0.1$. For smaller deformation values, such as in nanoindentation studies, an increase in the value of n is observed.

5.7. Determining Residual Stresses

In many engineering materials, residual stresses are caused by manufacturing and processing techniques. Residual stresses can also be introduced during the preparation of a sample surface for indentation tests, as a result of mechanical polishing. The effect of residual stresses on the indentation curve was studied in [90], where the authors concluded that compressive residual stresses increase the hardness and stiffness of the material, while tensile stresses reduce both properties, with a greater difference observed for stiffness. It was noted that in the presence of compressive residual stresses, this difference was caused by errors in calculating the actual contact area based on data obtained from the unloading curve. These errors were due to the pile-up effect. When the actual contact area was determined optically, neither stiffness nor hardness was affected by the residual stresses. In contrast, in [91], the authors, when studying the hardness and stiffness of soda-lime glass with compressive and tensile stresses, found that in the case of uniaxial stresses, the relationship between residual stresses and hardness and stiffness was similar to that described in [90], i.e., compressive residual stresses increase hardness while tensile stresses decrease it. However, in the presence of biaxial compressive-tensile stresses, which they observed near the edges of the Vickers indentation, both hardness and stiffness decreased. For thin films, literature reports indicate that reducing compressive residual stresses results in a slight increase in the hardness of titanium nitride (TiN) coatings [92, 93].

There are several methods described in the literature for using indentation tests to determine residual stresses in engineering materials. For example, in [94], an experimental method was presented that allows the measurement of both the nature and magnitude of applied stresses in metals. The method utilizes optical interference to measure the permanent surface deformations around a shallow spherical indentation in a polished metal sample surface. The author measured the deviation from the circular symmetry of the surface deformation under known applied stress values in reference samples. It was concluded that the deviation from symmetry could be used to determine the magnitude of applied tensile stresses in samples of the same material. Determining applied compressive stress proved more complex, and the method showed limitations in this regard.

Indentation tests using spherical indenters to determine stresses in brittle materials, such as glass and aluminum oxide, were discussed in [95]. The idea of determining stresses in this case is based on the existence of a threshold load below which cracks near the indentation, regardless of their size, cannot propagate. The presence of residual stresses in the surface layer shifts this threshold load. The method also assumes that the change in residual stresses has little effect on crack propagation lengths. The authors presented two methods of analysis (one approximate and one more general), which allow the calculation of residual stresses based on the change in threshold load. To determine residual stresses, it is only necessary to know the radius of the indenter, the elastic constants of the sphere and

substrate, as well as the fracture toughness (K_{IC}) of the substrate (or the use of a reference sample without stresses). There is no need to measure crack length.

In [96], experimental studies of indentation-induced fracture of flat surfaces of thermally tempered soda-lime glass were described. The indenters used were steel and tungsten carbide spheres with radii ranging from 0.5 to 2.5 mm, and a diamond Vickers pyramid. For spherical indenters, it was shown that Hertzian ring-cone cracks most often initiate on the contact circle between the indenter and the sample surface. Regarding the investigated sizes of spherical indenters, it was found that for tempered glass, the critical load required to cause ring-cone cracking is proportional to the indenter radius. These observations were compared with the results of studies of the same glass samples in an annealed state. Under the Vickers indenter, it was found that at sufficiently high loads, tempered glass forms a central crack. During the loading of the indenter, the shape of this crack remains approximately unchanged as the indenter load increases. During unloading, the central crack changes its shape. In annealed glass, the central crack clearly changes its shape as the indenter load increases during the loading cycle. Additionally, in both types of glass (with and without residual stresses), shallow radial cracks were observed to initiate during both loading and unloading of the indenter. The authors concluded that residual stresses can be calculated using the following equation:

$$\sigma_{\mathrm{R}} = \frac{\chi(P^{*}-P)}{1{,}16c^{2}} \tag{5.58}$$

In equation (5.58), P^* represents the indenter load at which cracks of length c form in glass with residual stresses, and P represents the indenter load at which cracks of the same length form in glass without residual stresses. The constant χ depends on the shape of the indenter. For a Vickers indenter with a vertex angle of 136°, it is:

$$\chi = \frac{1}{\pi^{3/2}\mathrm{tg}68} \tag{5.59}$$

Lee and Dongil, in their work [97], studied residual stresses in thin films of gold and DLC (diamond-like carbon) deposited on a silicon substrate. The authors found that the residual stresses in the coatings contributed to a change in the slope of the loading curve, while they did not affect the intrinsic hardness of the coatings. To explain the behavior of the indenter displacements in a coating with residual stresses, a stress-sensitive, reversibly deformed zone around the contact was modeled. Then, based on changes in the contact shape and applied load during stress relaxation under conditions of constant indenter displacement, the residual stresses were evaluated. According to the authors, these stresses can be determined based on the following relationship:

$$\sigma_{\mathrm{R}} = \frac{L_{\mathrm{Res}}}{A} \tag{5.60}$$

where $L_{Res} = L_0 - L_t$, for tensile stresses or $L_{Res} = L_0 - L_c$, for compressive stresses, where L_0 is the indenter load that causes its displacement into a material without residual stresses to a depth h_c, L_t is the indenter load at which its displacement is the same but in a material with tensile residual stresses, and L_c is the indenter load at which its displacement is the same in a material with compressive residual stresses as in a material without stresses. Figure 5.21 shows two indentation curves for structural steel with residual stresses and the same steel after stress-relief annealing. As shown in Figure 5.21, the reduction of residual stresses due to stress-relief annealing resulted in an increase in the indenter load (by 183 mN), which gives the same displacement as in the pre-annealed steel (in a stressed state). The difference of 183 mN, referred to the contact area A, allows for the determination of residual stresses in the stressed sample.

In the work [98], an experimental technique is presented that allows for the measurement of biaxial residual stresses using the indentation method. The technique is based on the use of a spherical indenter and appropriate applied loads, which in certain deformation regimes of the material, enable the determination of residual stresses. The authors developed two different methods for determining residual stresses. One method requires independent measurement of the material's yield strength, while the other utilizes a reference sample in a stress-free state or another known reference state. As described in subsection 5.1, plastic deformations occur in the material during indenter loading when the pressures p_m reach a value of $1.1R_e$. If biaxial residual stresses are present in the material, the onset of plastic deformation can be expressed as:

$$p_{\mathrm{m}} = 1{,}1(R_{\mathrm{e}} - \sigma_{\mathrm{R}}) \tag{5.61}$$

where σ_R represents the residual stresses in the material. Using equation (3.19), it can further be expressed as:

$$\sigma_{\mathrm{R}} = R_{\mathrm{e}} - \left(\frac{4E^{*}}{3{,}3\pi}\right)\frac{a}{R} \tag{5.62}$$

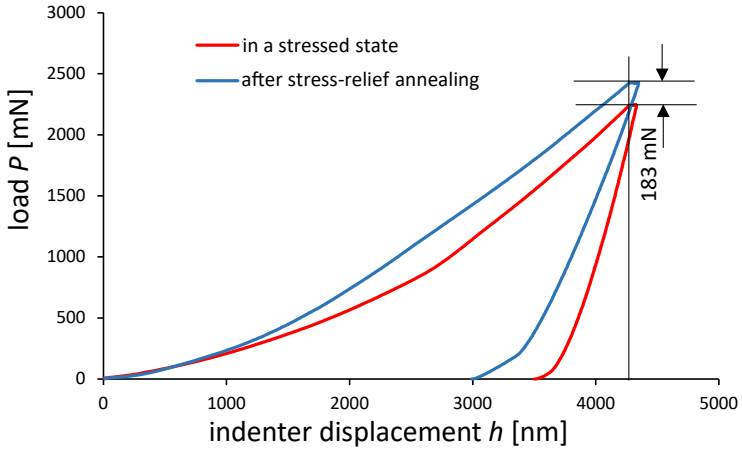

Fig. 5.21. Indentation curves obtained for high-strength chromium-nickel steel with 0.30% carbon content after CO_2 laser remelting and for the same steel after stress-relief annealing, both with the same maximum indenter displacement

Source: Own research results.

Equation (5.62) thus allows for the determination of residual stresses, provided the material's stiffness, hardness, and deformation a/R are known.

The second method for determining residual stresses is based on computer simulations using the finite element method (FEM) [98]. These simulations demonstrated that, over a wide range of material stiffness and yield strength, a correlation exists between the parameter h_r/h_{max} and residual stresses for a specific value of $(E/R_e)(2h_{max}/a_{max})$, where a_{max} is the contact radius measured in a straight line to the free surface of the specimen. Subsequently, Swadener et al. [98] observed that for a spherical indenter, when the average contact pressure p_m is in the transitional range (see Figure 5.7), and the function $p_m = f[(E/R_e)(a/R)]$ is determined, the data obtained will be vertically shifted by an amount equal to the applied biaxial stress σ_R, leading to the following equation:

$$p_{\mathrm{m}} + \sigma_{\mathrm{R}} = C\sigma_{\mathrm{F}} \tag{5.63}$$

where C is the constraint factor (discussed in Section 5.1), and σ_F is the flow stress, which represents the difference between the yield strength R_e and the residual stresses σ_R (Equation (5.61)). As seen from Equation (5.63), residual stresses can be determined in an indentation test using a spherical indenter, loaded in such a way that the average pressures it exerts fall within the transitional range (from $1.1R_e$ to CR_e), where the value of C is variable. The procedure for determining residual stresses requires calibration on a sample of the same material with known residual stresses, to establish how the constraint factor C changes as a function of the average contact pressures p_m within the transitional range. The advantage of this method is that it does not require knowledge of the material's yield strength to determine residual stresses. Experiments conducted on aluminum alloys with controlled biaxial bending stresses showed that both methods are capable of measuring residual stresses with an accuracy of 10–20% of R_e.

5.8. Determining the Critical Stress Intensity Factor

Fracture toughness is one of the key mechanical properties of brittle materials such as glass or ceramics, which are highly susceptible to destruction through brittle fracture. Conventional standardized testing methods used to determine fracture toughness typically require large samples to meet the condition of plane strain. For small samples, indentation is a popular and sometimes the only method available for determining fracture toughness, as it can be conducted on a small, flat surface of the specimen.

During the indentation test, tensile stresses are generated in the material as load is applied to the indenter, which increase as the radius of the plastic zone expands. Additionally, when the load is removed from the indenter, further stresses are generated because the elastically deformed material surrounding the plastic zone attempts to return to its original shape, but is hindered by the permanent deformation associated with the plastic zone . In hard and brittle materials, surface cracks initiate as the indenter penetrates, where tensile stresses reach their maximum values. The location of the highest tensile stresses is at the edge of the contact between the material and the indenter. Once initiated, the crack propagates and then halts at a certain distance, becoming stable. This occurs due to the stress

distribution, which decreases with increasing distance from the edge of the indentation, as shown in Figure 5.22 (see also Figures 5.5 and 5.8).

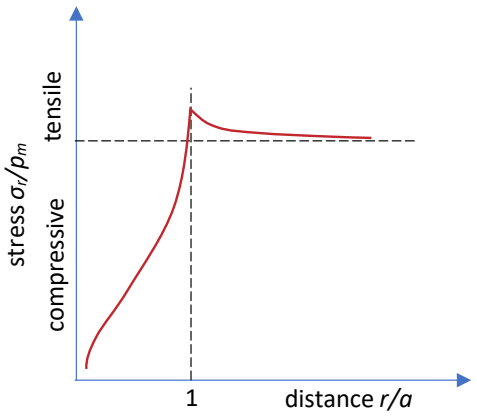

Fig. 5.22. Stress distribution in the material during spherical indenter penetration

Source: Own study based on [100].

The initiation, propagation, and arrest of cracks during an indentation test have allowed for the development of procedures to determine the critical stress intensity factor K_{IC} for brittle materials. The advantage of determining the K_{IC} factor using the indentation test, compared to conventional methods, is that the test does not require the preparation of large samples or the introduction of pre-existing cracks or notches. Another advantage is that the test is performed on the surface of the samples, and the maximum loads applied to the indenter are relatively small, making this method non-destructive. During indenter penetration in brittle materials, three types of cracks are generated [101]. The first type is radial cracks, which develop from the corners of the imprint in the case of sharp indenters, extend through the plastic zone, and stop beyond this zone. These cracks result from circumferential stresses and extend into the material, but they are usually quite shallow (Figs. 5.23, 5.24a). A variation of these cracks is semi-circular cracks, which develop in the same plane as radial cracks but propagate deeper, encompassing two opposite corners of the Vickers indentation, as shown in Fig. 5.24a. Both types of these cracks can be observed on the surface of the sample (Fig. 5.23).

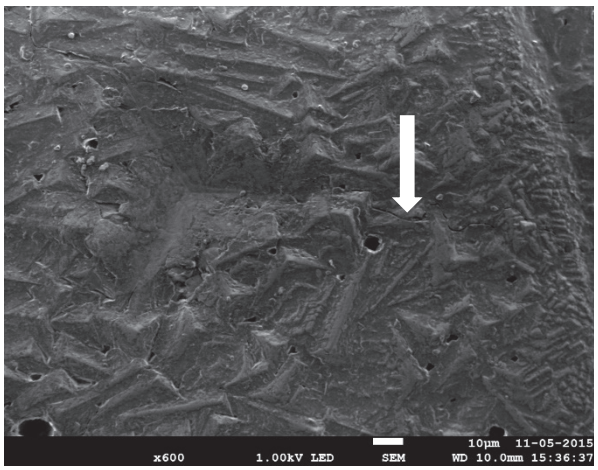

Fig. 5.23. Radial crack (arrow) in a plasma-sprayed Al2O3 coating on X5CrNi18-10 stainless steel, propagating from the corner of the indentation made by a cube corner indenter

Source: Based on own research findings.

The second type of cracks are transverse, or horizontal cracks, which initiate beneath the indenter and are symmetrical with respect to the load axis. They result from tensile stresses and often reach the surface, causing the formation of a surface ring, which can lead to chipping of the sample surface. The third type of cracks are median cracks, which develop vertically along the load axis of the indenter, taking a circular shape. These cracks form beneath the surface along the symmetry axis of the indentation and extend in the direction of its corners. Depending

on the loading conditions, median cracks may expand upwards and merge with surface radial cracks, forming two semicircular cracks that intersect the surface.

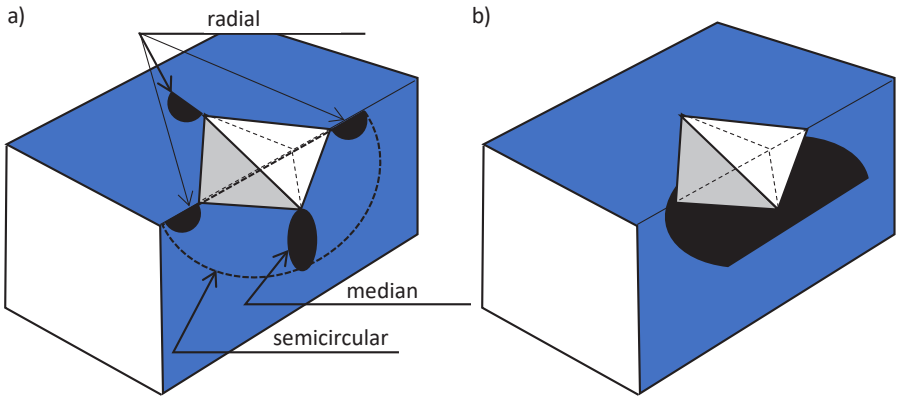

Fig. 5.24. Types of cracks formed during an indentation test using a sharp Vickers indenter in the cross-section of the indentation: a) median, semicircular, and radial cracks; b) transverse cracks

Source: own work based on [100].

The order in which these three types of cracks initiate depends on the indentation test conditions and the presence of residual stresses in the material. For example, tensile residual stresses perpendicular to the material surface will promote the initiation of transverse cracks. However, in determining the critical stress intensity factor, radial cracks are the most important because they are visible on the surface and can be easily measured for their length.

The author of the first studies published over 60 years ago that described the possibility of evaluating the brittleness of materials through indentation tests was Palmqvist [102, 103]. He observed that the length of cracks caused by indentation in brittle materials varied proportionally to the load applied to the indenter. However, due to issues related to contact/fracture, there is still no single model or method that can be universally applied to most brittle materials. Each existing method assumes a specific mode of fracture and is suitable only for certain groups of materials [104]. Based on literature reports, it can be concluded that sharp indenters can be used to assess the brittleness of a wider range of materials than spherical indenters, as the length of the resulting cracks can be easily and accurately measured. Existing methods for determining the K_{IC} factor have been developed empirically or semi-empirically, resulting in significant variation. For example, Lawn et al. [99] analyzed fully developed radial cracks formed during indentation tests on soda-lime glass and found that the ratio $P/c^{3/2}$, where c is the length of the radial crack measured from the geometric center of the indentation (Fig. 5.25), is a constant value, regardless of the indenter load. The value of this constant depends on the material's fracture toughness, which can be expressed using the following equation:

$$K_c = k\left(\frac{E}{H}\right)^n \frac{P}{c^{3/2}} \tag{5.64}$$

where k and n are coefficients ensuring the proper calibration of equation (5.64); for soda-lime glass, $k = 0.016$ and $n = 0.5$.

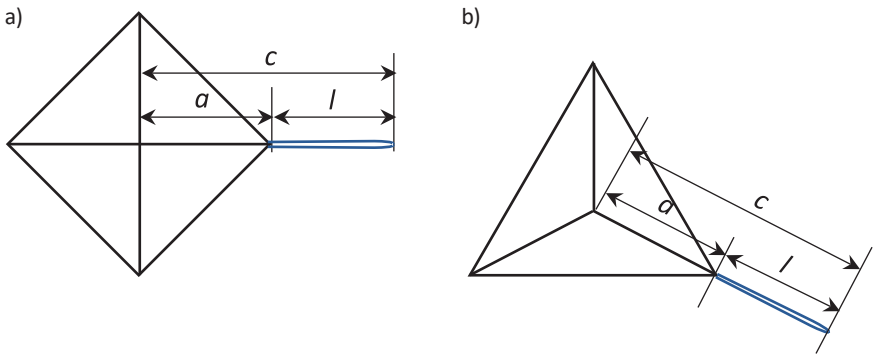

Fig. 5.25. Schematic images of indents from the Vickers (a) and Berkovich (b) indenters with marked radial cracks of length l

Source: own work based on [99].

In turn, Laugier [105], analyzing the results obtained by other researchers, proposed that fracture toughness be calculated using the following equation:

$$K_c = x_v \left(\frac{a}{l}\right)^{1/2} \left(\frac{E}{H}\right)^{2/3} \frac{P}{c^{3/2}} \tag{5.65}$$

where a, l, and c are the geometric quantities shown in Fig. 5.25. Laugier also demonstrated that for a constant $x_v = 0.015$, the predicted lengths of radial and semicircular cracks as a function of the load applied to the indenter are nearly identical. The research results also indicate that the quantity $(a/l)^{1/2}$ shows little variation between glass and ceramics. Equation (5.65) applies to the determination of the K_{IC} coefficient using a Vickers indenter. The Berkovich indenter is also frequently used in indentation studies; however, in this case, symmetry is lost, creating challenges for modeling and predicting crack lengths since two radial cracks cannot merge to form a larger semicircular crack. Therefore, Ouchterlony [106] proposed a correction factor k_1, which accounts for the number of radial cracks $n > 2$:

$$k_1 = \sqrt{\frac{\frac{n}{2}}{1+\frac{n}{2\pi}\sin\frac{2\pi}{n}}} \tag{5.66}$$

Dukino and Swain [107] compared the radial crack sizes caused by Vickers and Berkovich indenters for various materials. They found that the size of radial cracks was slightly larger for the Berkovich indenter than for the Vickers indenter. Their observations showed that cracks induced by the Berkovich indenter are best described by the expression developed by Laugier, combined with the modification proposed by Ouchterlony, which accounts for the number of radial cracks. Since the ratio k_{1V}/k_{1B}, where k_{1V} refers to the Vickers indenter ($n = 4$) and k_{1B} to the Berkovich indenter ($n = 3$), is 1.073, the radial crack length c for the Berkovich indenter should be $1{,}073^{2/3} = 1.05$ times the crack length produced by the Vickers indenter for the same K_c value. Therefore, for the Berkovich indenter, equation (5.65) can be rewritten as:

$$K_c = 1{,}073 x_v \left(\frac{a}{l}\right)^{1/2} \left(\frac{E}{H}\right)^{2/3} \frac{P}{c^{3/2}} \tag{5.67}$$

In brittle materials subjected to indentation testing using sharp indenters, it is often observed that, at a load much greater than necessary to initiate radial cracks, there is a sudden increase in the indenter's penetration rate. This phenomenon is referred to in the literature as pop-in (Figure 5.26) and is believed to be associated with a change in crack morphology. It presumably occurs when a median crack forms at the boundary of the plastic zone directly beneath the indenter's contact point. When a pop-in event happens, this crack rapidly propagates toward the surface and joins with existing cracks, leading to the formation of radial cracks on the surface. Although the propagation of median cracks from each corner may not occur simultaneously, all corners seem to be involved in initiating cracks as the load increases. When a pop-in occurs at lower loads, the increase in indenter penetration is smaller compared to a pop-in at higher loads, but regardless of the threshold for pop-in, the crack paths eventually converge and remain connected throughout the rest of the loading sequence.

The pop-in phenomenon is not generally observed with less sharp indenters at similar loads, and the threshold load appears to be related to the indenter's apex angle and is characteristic of the given material. Reducing the indenter's apex angle promotes crack initiation in brittle materials and allows for the assessment of fracture toughness at low indenter loads. However, cracks formed at very low loads are short and difficult to measure. Therefore, Field et al. [108] proposed that instead of measuring the length of short cracks c (Figure 5.25), their length could be calculated using the additional indenter displacement depth h_x caused by the pop-in effect, as shown in Figure 5.26a, using the following equation:

$$c = \sqrt{2h_{\mathrm{m}}} + \left(Q\frac{E\prime}{H_{\mathrm{M}}} - \sqrt{2}\right) h_x \tag{5.68}$$

where Q is a constant that can be obtained by differentiating equation (5.68) with respect to h_x, H_M is Meyer hardness, and h_x can be calculated as the difference between the maximum indenter displacement h_m with the pop-in effect and the indenter displacement h_t, which would have occurred if the pop-in effect had not taken place. This displacement can be calculated using equations (5.25) and (5.26), assuming the parameter m = 2. As mentioned, the parameter Q is calculated by differentiating equation (5.68); this yields:

$$\frac{dc}{dh_x} = Q\frac{E\prime}{H_{\mathrm{M}}} - \sqrt{2} \tag{5.69}$$

The value of dc/dh_x can be obtained from the equation:

$$\frac{dc}{dh_x} = \frac{dc}{dP^{2/3}} \frac{dP^{2/3}}{dh_x} \tag{5.70}$$

where $dc/dP^{2/3}$ is the slope of the line $c = f(P^{2/3})$, as predicted by Lawn et al. [99], and $dh_x/dP^{2/3}$ is the inverse of the slope of the line $h_x = f(P^{2/3})$.

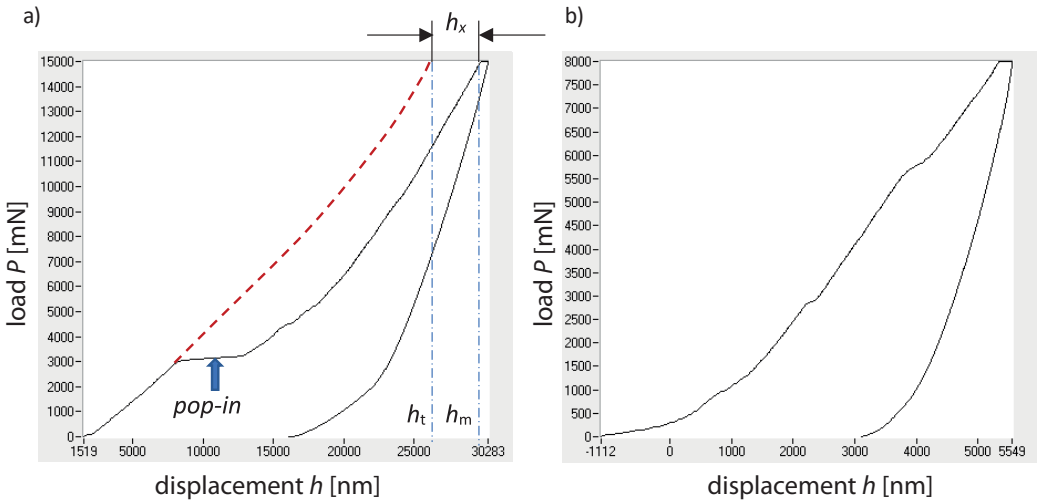

Fig. 5.26. Indentation curve of plasma-sprayed Al_2O_3 on X5CrNi18-10 stainless steel using a Berkovich indenter showing a large pop-in effect (a) and the same coating after remelting with a CO_2 laser with two smaller pop-in effects, indicating greater crack resistance (b)

Source: based on own research.

5.9. Dynamic Indentation Test

The value of *dP/dh* can also be determined by applying a sinusoidal load to the indenter (dynamic test). The advantage of this method is that the *dP/dh* measurements can be obtained more quickly (e.g., during a loading sequence), and it also allows for the measurement of the storage modulus *G'* and the loss modulus *G"* of the sample material.

In ideal elastic-plastic materials during a static tensile test, in the elastic deformation range, the strain corresponds to stress, and the proportionality constant between them is called the Young's modulus *E*. In dynamic tests, it is often the shear stress, not normal stress as in uniaxial tensile or compression tests, that is of interest. For shear stresses, the proportionality constant between stress and strain in the elastic range is called the shear modulus *G*. Both *E* and *G* are material properties that quantify the elastic characteristics of the material and, consequently, its ability to store elastic deformation energy under load. In an ideal elastic material, this stored energy is denoted by *G'*. In contrast, in an ideal viscous material, there is no elastic deformation, and the material's response, i.e., its deformation, to applied stress will be phase-shifted by 90° relative to the applied strain (Fig. 5.27a, b). In this case, the stress generated in the material is proportional to the rate of applied strain, and the proportionality constant is known as the loss modulus, denoted *G"*. The loss modulus is directly related to the material's viscosity. In dynamic tests, materials usually exhibit viscoelastic behavior. For viscoelastic materials, the combined elastic and viscous response is represented by the complex modulus, defined as:

$$G^* = G' + iG'' \tag{5.71}$$

If we consider a system like in Fig. 5.28, where the spring has a stiffness k and the damping element has a damping coefficient λ, and if a force is applied to the mass m in such a way that it causes oscillations, then generally, there is a phase shift ø between the force and displacement signals. Mathematically, this can be expressed as:

$$P(t) = P_0 e^{i(\omega t + \phi)} \tag{5.72}$$

$$h(t) = P_0 e^{i(\omega t)} \tag{5.73}$$

The velocity and acceleration of the mass can be obtained by differentiating equation (5.73) once and twice with respect to time, leading to:

$$\frac{dh}{dt} = i\omega h \tag{5.74}$$

$$\frac{d^2h}{dt^2} = -\omega^2 h \tag{5.75}$$

Linear viscoelastic solids are typically best represented by the standard three-element Voigt model, as shown in Fig. 5.28. In this model, the application of a gradual displacement of the mass causes an immediate high value of stress, which gradually stabilizes over time. Similarly, a gradual increase in stress results in an immediate displacement that increases to a steady value over time. In the model where the spring and the damping element are arranged in parallel, as in the Voigt model (Fig. 5.28), the force P can be expressed as the sum of three components:

$$P = kh + \lambda\frac{dh}{dt} - m\frac{d^2h}{dt^2} = (k - m\omega^2 + i\omega\lambda)h \tag{5.76}$$

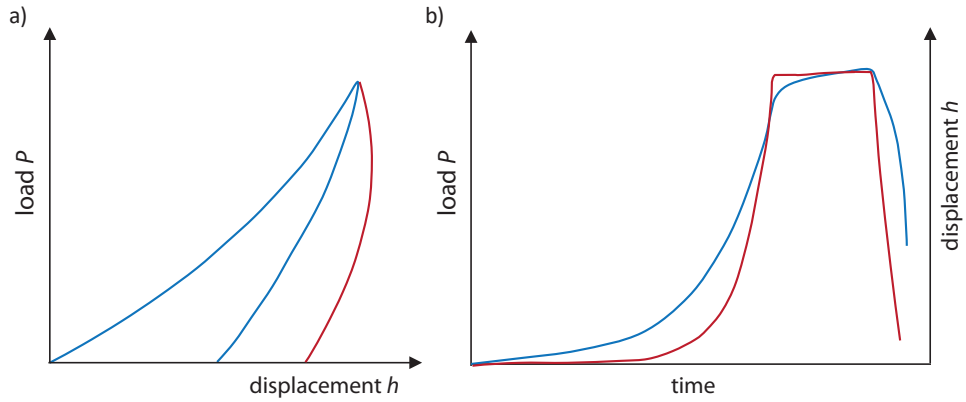

Fig. 5.27. Indentation curve in a static indentation test for an elastic-plastic material (blue line) and a viscoelastic material (red line) (a) and time-dependent load curves (red line) and indenter displacement (blue line) for a viscoelastic material (b)

Source: Own work based on [109].

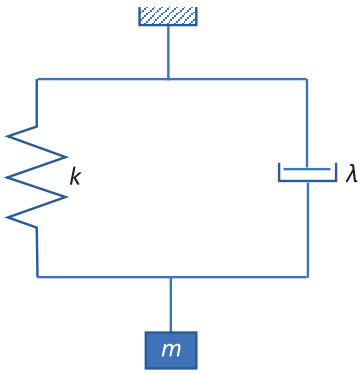

Fig. 5.28. Dynamic mechanical model of Voigt with a mass supported by a spring with stiffness k and a damping element with damping coefficient λ

Source: Own work based on [56].

The expression in parentheses in equation (5.76) is called the transfer function (TF). The real part of the TF refers to the storage of elastic energy G', while the imaginary part equals the loss modulus G'', i.e.:

$$G' = k - m\omega^2 \tag{5.77}$$

$$G'' = \omega\lambda \tag{5.78}$$

In cases where the loading geometry is more complex than shown in Fig. 5.28, such as in the indentation test, the storage modulus G' and loss modulus G'' can be derived from the transfer function (TF) if the loading geometry parameters are known. For example, in an indentation test, the spring constant k in the above equations is the

contact stiffness *S,* which in this case is related to the reduced modulus of elasticity of the indenter and the sample E^* as follows:

$$E^* = S\frac{\sqrt{\pi}}{2\sqrt{A}} \tag{5.79}$$

The contact stiffness S is related to the storage modulus G'. If S represents the contact stiffness, the magnitude of the transfer function (TF) vector for equation (5.76) is defined as:

$$|TF| = \frac{P_0}{h_0} = \sqrt{(S - m\omega^2)^2 + \omega^2\lambda^2} \tag{5.80}$$

and the phase shift angle ϕ between the load and the indenter displacement is given by:

$$\mathrm{tg}\phi = \frac{\omega\lambda}{S - m\omega^2} \tag{5.81}$$

In a nanoindentation experiment, the quantities P_0 and h_0 as well as the phase angle tgø are measured. The mass component can be determined by oscillating the indenter in air, i.e., for $S = 0$ and $\lambda = 0$, and performing measurements for different frequencies ω. The mass m is then obtained from the plot of the transfer function TF versus ω^2. When in contact with a viscoelastic sample, the real TF_{re} and imaginary TF_{im} parts of the transfer function TF are determined from the experimental readings of P_0, h_0, and ø as follows:

$$G' = TF_{\mathrm{re}} = \frac{P_0}{h_0}\cos\phi = S - m\omega^2 \tag{5.82}$$

$$G'' = TF_{\mathrm{im}} = \frac{P_0}{h_0}\sin\phi = \omega\lambda \tag{5.83}$$

and the total shear modulus can be calculated from equation (5.71). From equations (5.82) and (5.83), the contact stiffness S can be determined, and using equation (5.79), the reduced modulus E^* can also be calculated. The system presented in Figure 5.28 is a simplified representation of the behavior of the sample. In practice, additional mechanical elements participate in the deformation, depending on the characteristics of the device used to perform the indentation test. For example, in an indentation test, the stiffness of the shaft support, on which the indenter is mounted, must also be considered. When measuring the dynamic properties of a viscoelastic material, an additional damping component λ_s, related to the interaction between the indenter and the sample, must be taken into account. In dynamic tests conducted over a range of frequencies, the slope of the stiffness graph $S = f(dP/dh)$ is proportional to the material's elastic modulus, while the slope of the $\lambda_s \cdot \omega = f(h)$ graph is proportional to the material's loss modulus G'' at *the* contact point with the indenter .

If E^* is known, the contact area A can be calculated from equation (5.16), and based on this, the hardness and modulus of elasticity of the material can be determined. For a perfectly elastic material, the storage modulus G' corresponds to the stiffness of the spring k. In the indentation test, the "spring" is nonlinear, and the reduced (complex) modulus E^* can be derived from the storage modulus G' using the contact equations:

$$E^* = \frac{\sqrt{\pi}}{2\sqrt{A}}G' = \frac{\sqrt{\pi}}{2\sqrt{A}}\frac{P_0}{h_0}\cos\phi = \frac{\sqrt{\pi}}{2\sqrt{A}}TF_{\mathrm{re}} \tag{5.84}$$

$$E'' = \frac{\sqrt{\pi}}{2\sqrt{A}}G'' = \frac{\sqrt{\pi}}{2\sqrt{A}}\frac{P_0}{h_0}\sin\phi = \frac{\sqrt{\pi}}{2\sqrt{A}}TF_{\mathrm{im}} \tag{5.85}$$

A useful measure to determine the relative contribution of the storage modulus and the loss modulus in the mechanical response of a material is the loss factor, defined as:

$$\mathrm{tg}\delta = \frac{E''}{E^*} \tag{5.86}$$

where δ = ø. If tanδ >1, the material behaves predominantly like a viscous substance, whereas if tanδ <1, it indicates that the material behaves mostly like a solid.

From the perspective of contact viscosity, the complex viscosity is defined as:

$$\eta^* = \eta' + i\eta'' \tag{5.87}$$

where η' and η'' are:

$$\eta' = \frac{G''}{\omega} \tag{5.88}$$

$$\eta'' = \frac{G'}{\omega} \tag{5.89}$$

In this case, the real part of the total viscosity represents the fluid-like behavior of the material and is referred to as dynamic viscosity, while the imaginary component is representative of the material's elastic response. From equation (5.78), it follows that for the Voigt model, the damping component λ can be directly obtained from the loss modulus G″. In the case of indentation testing, the situation is more complicated, as the contact area changes with loading, meaning the nature of the contact viscosity depends on the loading history. Conventionally, the quantity $\omega\lambda$ is associated with the loss modulus *G"*, but viscosity is often the primary focus of interest. For the scenario of gradual loading of a conical indenter, linear viscous creep of a solid is expressed as [110]:

$$P = \left(\frac{8}{3}\eta\right)\left[\frac{2}{\pi}h \cdot \mathrm{tg}\alpha\right]\frac{dh}{dt} \tag{5.90}$$

Since $dh/dt = i\omega h$ (equation (5.74)), equation (5.90) can be written as:

$$P = i\left(\omega\frac{8}{3}\eta\right)\left[\frac{2}{\pi}h^2 \cdot \mathrm{tg}\alpha\right] \tag{5.91}$$

The expression in square brackets in equation (5.90) corresponds to the loss modulus *E"* described by equation (5.85). To obtain it, TF_{im} should be determined from the dynamic indentation test. Then, to calculate the viscosity, the loss modulus *E"* should be divided by 8ω/3.

A *similar* analysis for a spherical indenter gives the equation:

$$P = i(2\omega\eta)\frac{4}{3}h^{3/2}R^{1/2} \tag{5.92}$$

It is important to remember that equation (5.90) is valid only when the load applied to the indenter is increasing, and extending this equation to sinusoidal oscillatory motion (loading and unloading the indenter) is not entirely appropriate. Additionally, in many contact situations, the relationship between P and h is nonlinear, and this function depends on the shape of the indenter. The presence of plastic deformation in the material during contact also affects the validity of the reduced modulus E^* for a zero frequency, calculated using the above procedure. In practice, the described method is only suitable for small amplitude oscillations.

5.10. Scratch Test

A typical scratch test requires gradually increasing the load on the indenter while simultaneously moving it in a direction perpendicular to the applied force. The scratch test is most commonly performed on thin coatings to determine the critical normal force, L_c, at which adhesion failure between the coating and the substrate occurs (Fig. 5.29). However, during the scratch test, as the load on the indenter increases, various forms of material damage may be generated. Therefore, the analysis of the scratch test process allows not only the determination of the adhesion of coatings to substrates but also the characterization of the coating material and the surface layers of solid materials (Fig. 5.30).

During the scratch test, as well as in a simple indentation, various events can occur, such as cracking of the surface layer, coating, or substrate, delamination between the coating and the substrate, phase transformations, or slip under the indenter. These events are often accompanied by acoustic emission, and its analysis allows for correlating the magnitude of the applied load with the occurrence of these events. Furthermore, the amplitude of the recorded acoustic emission indicates the intensity of the event. For instance, in the study [111], the authors determined the energy of events occurring during the scratch test of titanium carbide based on the acoustic emission signal obtained.

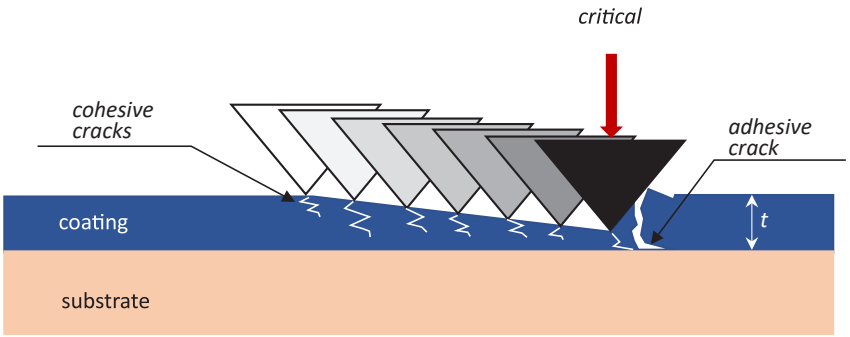

Fig. 5.29. Successive indenter positions during the scratch test of the coating and corresponding cohesive and adhesive cracks

Source: Own work based on [111].

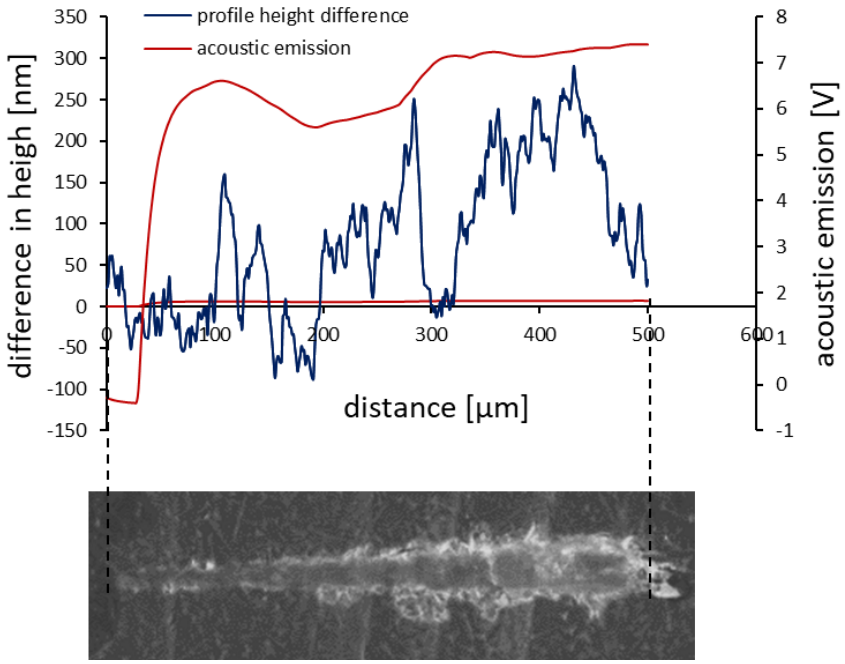

Fig. 5.30. Example of data obtained from a scratch test on a plasma-sprayed Al_2O_3 coating. Measured height difference in the surface profile before and after the test, along with acoustic emissions accompanying the scratch. The test was conducted over a distance of 500 µm, and the normal force increased from 0 to 6 N

Source: based on own research.

The interpretation of data sets from scratch tests has become easier in recent years thanks to the emergence of better tools, such as panoramic imaging, depth characterization, and synchronized optical microscopy observation of the scratch track. Improved methods for modeling the deformation of the coating, substrate, and contact as a function of the applied load have provided a better understanding of the indentation test parameters, which can lead to coating failure at the required depth (usually at the interface between the coating and the substrate). This has led to an increased use of a wide range of indenter sizes and shapes, which allow for calculating the ideal contact conditions with the substrate before testing. Significant progress has also been made in using scratch tests to measure additional mechanical properties of materials, such as fracture resistance, hardness, viscoelasticity, etc. Moreover, the use of scratch tests in conjunction with other techniques, such as acoustic microscopy, Raman spectroscopy, in-situ microscopy, etc., has revealed additional information about subsurface events (such as cracking, fatigue, tearing, etc.) that were not previously accessible. It is expected that these and other successful applications of scratch tests will provide the necessary information for the development of multiscale models of the mechanical behavior of materials [112].

As already mentioned, the scratch test is most commonly performed to determine the critical force at which delamination between the coating and the substrate occurs. The driving forces for damage in the coating-substrate system during the scratch test are a combination of elastic-plastic indentation stresses, friction stresses, and residual stresses present in the coating (usually introduced during the deposition process). During a scratch test with increasing load, several successive instances of coating damage can be observed as the load increases, with the final instance typically corresponding to complete delamination. The critical load depends on the adhesion of the coating, but also on several other parameters, some of which are directly related to the test itself (internal parameters), while others are related to the coating-substrate combination (external parameters). The critical damaging load (causing delamination) L_c can be expressed as:

$$L_c = \frac{A}{\nu \mu_c} \left(\frac{2EW}{t}\right)^{\frac{1}{2}} \tag{5.93}$$

where A is the cross-sectional area of the scratch track, ν is the Poisson's ratio of the coating material, μ_c is the coefficient of friction between the indenter and the coating at the critical load, E is the elastic modulus of the coating, W is the work done to detach the coating, and t is the thickness of the coating.

The scratch test can also be performed under a constant indenter load. In such cases, it is typically conducted as a series of scratches at a constant load or at increasing loads at regular time intervals. When the scratch is repeated

along the same track, it becomes a wear test. The scratch test is closely related to tribology. In tribological studies, common techniques such as pin-on-disk, ball-on-disk, pins, rings, or disk-on-disk are used, enabling the measurement of friction force and coefficient of friction, layer adhesion strength, wear rate, contact resistance, and acoustic emission events related to cracking. Conventional indentation instruments generally do not offer such capabilities. However, some tribological instruments do provide an indentation mode.

6. Examples of own Research in the Characterization of Engineering Materials

6.1. Mechanical Properties of Bacterial Nanocellulose

Cellulose is a polysaccharide composed of D-glucose units connected by β-glycosidic bonds and is naturally occurring in the environment. It is a component of cotton and wood, but can also be produced by bacteria. In this way, cellulose provides bacteria with access to oxygen and nutrients and protects them from harmful UV radiation [113]. Bacterial nanocellulose (BNC) can also be produced in bioreactors. There are many strains of bacteria that synthesize BNC, with "Gluconacetobacter xylinus" being the most well-known and efficient strain [114]. Due to its unique properties, such as high chemical purity compared to plant-based cellulose, non-toxicity, high water absorption, flexibility, biocompatibility, thermal stability, and environmental friendliness, BNC has many medical and technical applications. It is used in wound dressings, vascular implants [115], and as a material for artificial skin [116]. BNC also shows promise as a material for heart valve prostheses. However, its main drawback is its lower mechanical strength compared to synthetic polymers, due to the presence of a large amount of water in the synthesized BNC membrane. Physical or chemical modifications can improve the mechanical properties of BNC. The simplest way to modify BNC's structure and properties is through physical modification by drying. Gentle drying conditions, such as convection or lyophilization, make this the easiest way to increase BNC's tensile strength. The selection of appropriate convection and lyophilization parameters can shape the material's morphology [117]. Many chemical modification methods of BNC are also known. One way to change the structure and improve BNC properties is to select appropriate components for the polymer matrix, creating a composite either during (in situ) or after (ex situ) production by introducing additional modifying compounds, such as silver nanoparticles, chitosan, or hydrocarbon acids, into the polymer matrix.

Tensile strength and creep resistance are key mechanical properties that should be considered when selecting materials for cardiovascular implants, as they are usually subjected to variable stresses. Proper chemical and physical modifications of BNC, in addition to improving mechanical properties, can also lead to a material with enhanced biocompatibility. This would improve the safety of using BNC-based valve prostheses and increase their durability, extending their lifespan.

The results presented in this subsection were obtained as part of a project funded by NCBiR, aimed at developing alternative materials to the currently used synthetic materials for aortic heart valves and implementing the industrial-scale production of BNC. The author of this monograph was responsible for assessing the impact of physical and chemical modifications on the mechanical properties of BNC in the PBSII project titled "Preclinical studies of the potential use of original Polish bionanocellulose (BNC) in regenerative medicine in the context of bioimplants in cardiac and vascular surgery" (acronym: KARDIO BNC), under the Applied Research Program. The project was carried out in collaboration with research institutions, including the Faculty of Medicine of the Medical University of Gdańsk, Bowil Biotech Sp. z o.o., the Faculty of Chemistry and the Faculty of Mechanical Engineering of Gdańsk University of Technology, Maritime Advanced Research Centre, Professor Zbigniew Religa Foundation of Cardiac Surgery Development, and the Faculty of Biology of the University of Gdańsk. Figure 6.1 presents the view

of a heart valve prosthesis made of BNC and its testing stand. The testing stand shown in the image is located at the Medical Engineering Laboratories of the Maritime Advanced Research Centre in Gdańsk.

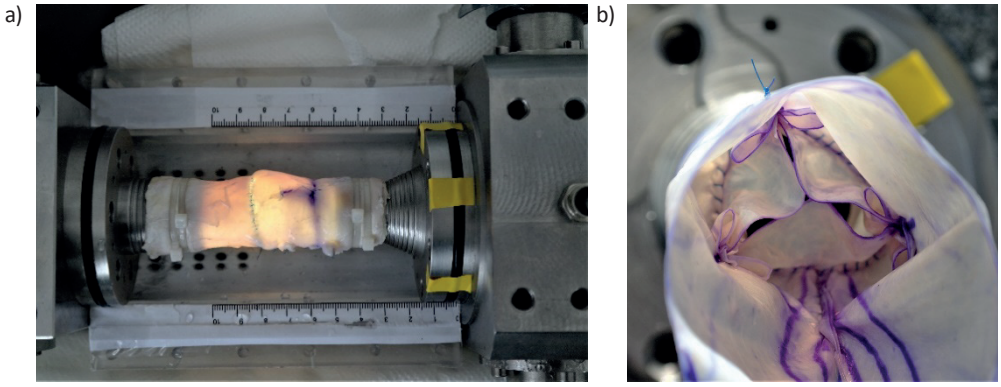

Fig. 6.1. View of the in vitro testing stand for heart valve prostheses (a) and a heart valve prosthesis sewn into a vessel made of BNC (b)

Source: Valve tests conducted as part of the KARDIO BNC project PBS2/A7/16/2013, funded by The National Centre for Research and Development (NCBiR) – grant PBS2/A7/16/2013.

The bacterial nanocellulose (BNC) samples for testing mechanical properties were produced by the biotechnology company Bowil Biotech. The cellulose production process has been described in detail in patents: PL 171952B1 (1993) and PL 212003B1 (2003). All details regarding the production of native BNC are presented in [118]. The BNC production was carried out using the "*Gluconacetobacter xylinus*" E25 strain in the standard Schramm and Hestrin SH solution, consisting of 5–10% inoculum, which constituted one-third of the volume. The synthesis temperature was in the range of 30 ± 2°C, and the pH of the medium was 5.75 ± 0.03. After synthesis, the membranes were cleaned, pressed, rinsed with water, and then boiled in 1% sodium hydroxide (NaOH), followed by acetic acid. After these procedures, the BNC was boiled again in tap water, then in deionized water, and pressed. It was then sterilized in an autoclave for 20 minutes at 120°C. The resulting material was native BNC (reference BNC) and had a thickness of 2 mm.

The chemically modified BNC was produced in the SH medium containing 2% glucose and 1% hyaluronic acid (HA), added during the tray casting stage (in situ modification). The same steps as used for the synthesis of native BNC were then followed. The material was cut into smaller pieces and sterilized in an autoclave for 20 minutes at 120°C. The obtained samples had a thickness of 2 mm and were referred to as native BNC HA (reference BNC HA). For physical modification, the BNC and BNC HA materials were dehydrated by convective drying at 25°C (25DR), 105°C (105DR), and lyophilization (FDR), followed by rehydration through soaking in demineralized water at 25°C for 2 hours (ex situ modification). The resulting samples had a thickness of 0.5 mm for 25R and 105DR and 2 mm for FDR BNC and BNC HA.

To characterize the biocellulose, a NanoTest Vantage nanoindenter (Micro Materials, UK) was used. A diamond Berkovich indenter was employed for the tests. The maximum load was 1 mN, and the loading rate of the indenter was 0.02 μN/s. The same unloading rate was applied. To determine the creep rate (cellulose creep), the maximum load was maintained for 10 seconds (dwell time). The creep rate $\dot{\varepsilon} = d\varepsilon/dt$ was calculated as the slope of the straight line of the relative displacement of the indenter ε as a function of time t during the stabilized creep period (constant creep rate; see Figure 5.19). In the nanoindentation test, the hardness and stiffness of the cellulose (reduced Young's modulus) were also determined using the Oliver–Pharr method. Each measurement was performed 10 times, and the average and standard deviation were calculated.

Figure 6.2 shows the load-displacement curve for physically modified BNC (Figure 6.2a) and BNC HA (Figure 6.2b). The graphs in Figure 6.2 represent the median of 10 measurements. As shown, the curves are typical for elastoplastic materials. At 10% of the maximum force, corrections for thermal drift can be seen on the indenter unloading curves. Based on these curves, the stiffness (Young's modulus), hardness, and creep rate of BNC were calculated. As seen in Figure 6.3, ex situ modification of BNC allows for an increase in hardness by 69–115%, depending on the method. Furthermore, double modification of BNC, first in situ by adding HA to the medium and then ex situ through soaking in water and convective or lyophilization drying, increases hardness by 73% for lyophilization and 407% for convective drying at 25°C. A similar trend was observed for BNC stiffness (Figure 6.3b), which was also increased by *ex situ* modification.

The high water content in native BNC and BNC HA [119] likely resulted in a significant reduction in longitudinal Young's modulus, as shown in the nanoindentation test for physically modified BNC. Only FDR BNC HA showed values of E and H comparable to native BNC and BNC HA. This is likely due to the size and distribution of pores present in the HA BNC structure after lyophilization. Microscopic studies indicated that this drying method produced the highest percentage of pores, and the pores were larger than those produced by other drying methods. Due to the small forces applied, in the range of 1 mN, the results showed high variability. The indenter could either measure individual fibers, fiber agglomerates, or hit a pore, in which case the calculated hardness could be very low or close to zero. However, the results indicate that BNC and BNC HA become strengthened after physical modification, which is also associated with an increase in hardness and Young's modulus compared to the native material. Convective drying at 25°C and lyophilization show a strong correlation between the magnitude of residual stresses (determined in earlier studies based on XRD diffraction pattern analysis) and high hardness and stiffness, despite the stresses being tensile in nature. A similar observation was made for BNC HA dried at 25°C. This may be due to the formation of more hydrogen bonds, which generate tensile residual stresses. However, there is no correlation between the degree of crystallinity and crystallite size (determined in XRD studies) with BNC hardness and stiffness.

An important property of BNC from the perspective of its application in cardiovascular implants is creep resistance, which can be defined as the inverse of the creep rate in the steady state during constant indenter load at maximum load. Figure 6.4 shows the change in deformation ε of modified BNC (Figure 6.4a) and BNC HA (Figure 6.4b) during maximum indenter load. As seen, for the first 6 seconds, the creep rate decreases, after which it stabilizes at a constant level. This creep behavior suggests that it can be described using equation (5.52), which is a combination of Maxwell and Voigt models (see Figure 5.17c).

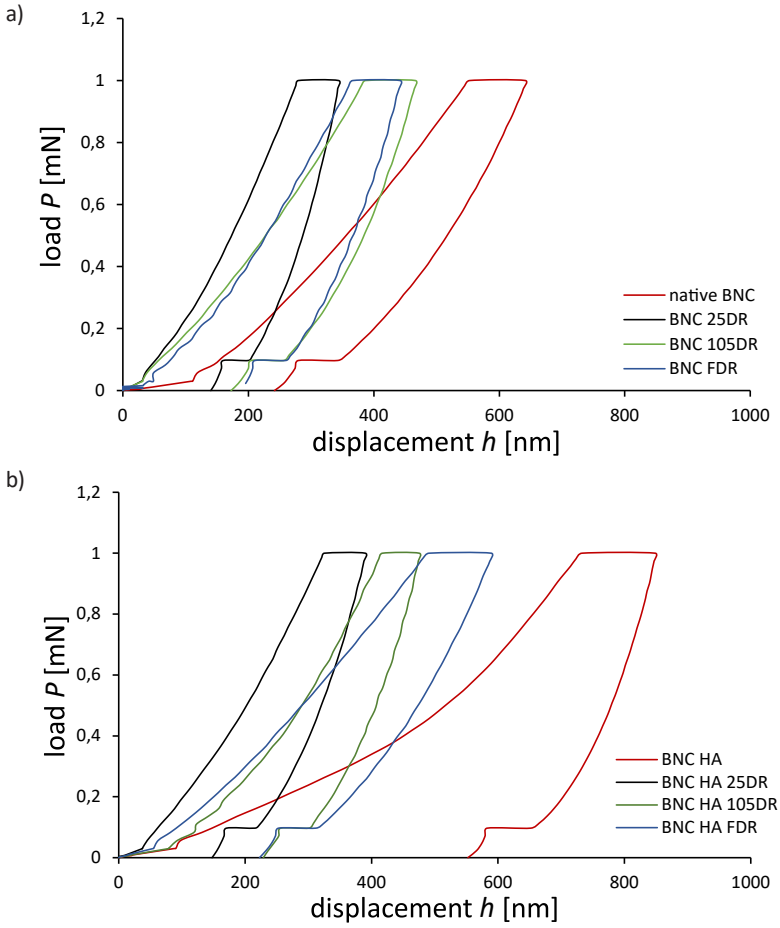

Fig. 6.2. Load-displacement curves determined for physically modified BNC (a) and BNC HA (b). The presented curves represent the median of 10 measurements

Source: Developed based on own research [120].

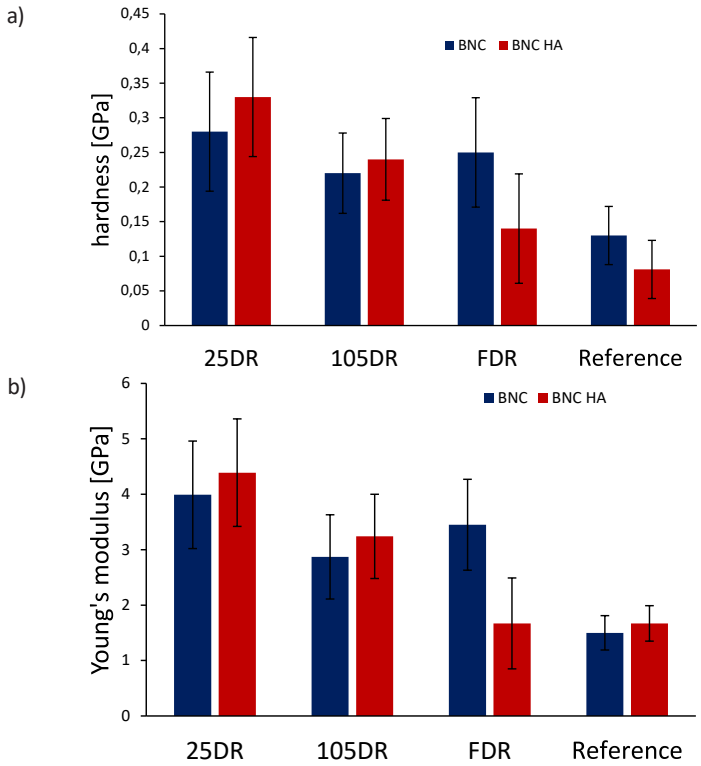

Fig. 6.3. Average hardness results (a) and average Young's modulus (b). Results obtained from 10 measurements in the nanoindentation test. Error bars indicate ± standard deviation

Source: Developed based on own research [120].

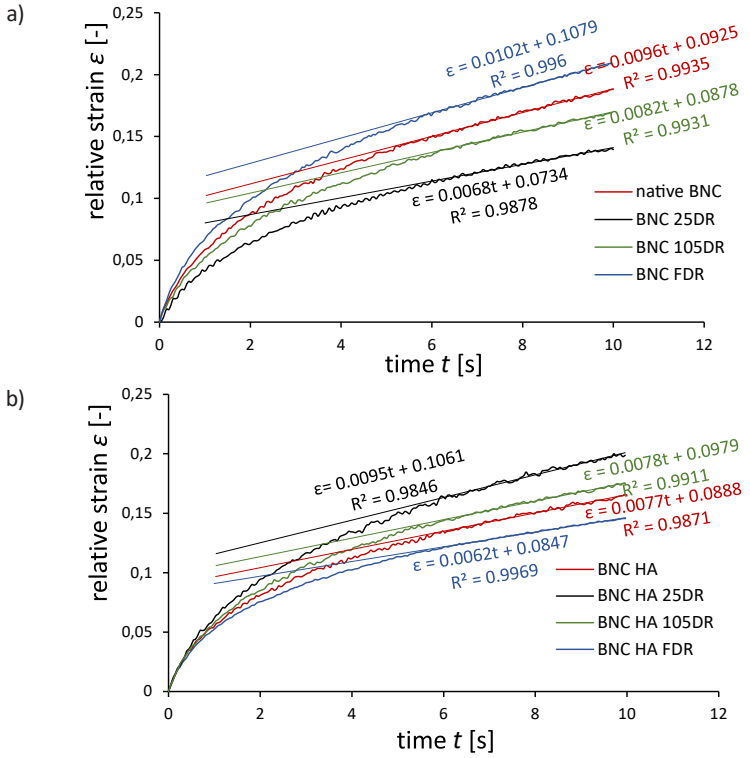

Fig. 6.4. Examples of creep curves (median of 10 measurements) determined by nanoindentation for BNC (a) and for BNC HA (b)

Source: based on own research [120].

Fig. 6.5 presents the arithmetic mean value of the creep rate calculated from 10 trials. As shown in Fig. 6.5, BNC HA and freeze-dried BNC HA exhibited the lowest creep rate, while the highest creep rate was recorded for freeze-dried BNC. These results indicate that creep resistance is related to the porosity of BNC. A low number of

pores in the structure of BNC HA and FDR BNC HA positively impacts BNC's creep resistance. On the other hand, a high number of pores, as in the case of FDR BNC, corresponds to lower creep resistance.

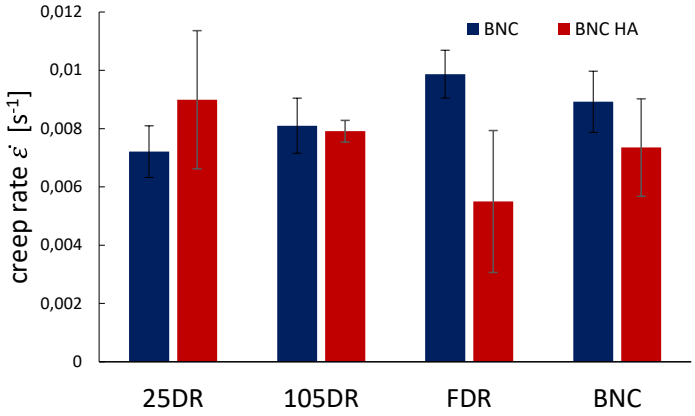

Fig. 6.5. Average creep rate for BNC and BNC HA determined from 10 trials. Error bars indicate ± standard deviation

Source: based on own research results [120].

To verify whether the obtained results for hardness *H,* Young's modulus *E,* and creep rate are statistically significant, a one-way analysis of variance (ANOVA) was performed. The results indicate that significant differences were observed between the groups for all analyzed BNC modifications, with a p-value of less than 0.01. To assess the strength of these effects, the η^2 coefficient was calculated as the ratio of the sum of squares (SS) between the tested groups (modifications) and the total SS. For both groups of cellulose, BNC and BNC HA, the η^2 values were no less than 0.41, 0.56, and 0.57 for hardness, Young›s modulus, and creep rate, respectively. Since the η^2 values were greater than 0.14, it can be concluded that there is a strong differentiating effect between the BNC groups. As the research results suggest, the indentation test can be used to characterize the BNC polymer and determine the influence of its production parameters on its mechanical properties.

Nanoindentation testing has proven to be a valuable method for characterizing the mechanical properties of bacterial nanocellulose (BNC). This technique allows for precise measurements of hardness, Young's modulus, and creep resistance, providing insights into the effects of both physical and chemical modifications on the material. The results indicate that nanoindentation can effectively evaluate the impact of production parameters on BNC's mechanical performance. Furthermore, this method can be successfully applied to assess the mechanical properties of new and advanced engineering materials, making it a versatile tool in materials research and development.

6.2. Characterization of the Ground Surface Layer of C45 Steel

Grinding is a finishing abrasive process that allows obtaining products with high dimensional accuracy and low surface roughness, with a specific topography that can be influenced even by the number of tool passes. However, designers often require not only low roughness and high dimensional accuracy but also sufficiently high mechanical properties of the ground surface layer. To meet these expectations, technologists plan heat treatment or thermo-chemical treatment of ground products, such as bulk or surface hardening, carburizing, or nitriding. However, such additional technological processes increase production costs and extend the production time. Moreover, heat treatment or thermo-chemical treatment requires the use of toxic coolants, which negatively affect the environment and production workers who are in direct contact with them [121]. In recent years, technology combining grinding with simultaneous hardening of the surface layer has been intensively developed to eliminate these disadvantages [122, 123]. During grinding, the surface layer of the workpiece heats up rapidly and is subjected to significant mechanical loads. The heat generated by friction between the workpiece and the grinding wheel raises the temperature of the workpiece. The increase in temperature of the ground surface layer above the austenitization temperature A_{c3} (the temperature at which ferrite transforms into austenite) and simultaneous rapid cooling of the workpiece at a rate greater than critical results in the hardening of the ground surface layer. However, the introduction of this technology in the production of structural elements faces several difficulties. There are problems with obtaining repeatable results, achieving the desired depth of hardening, and attaining the specified hardness after grinding, which necessitates

applying so-called softening grinding to temper the hardened surface layer. Additionally, setting grinding parameters to achieve the surface temperature increase necessary for ferrite to austenite transformation significantly reduces the yield strength of the heated layer, which, combined with the high mechanical loads during grinding, makes it difficult to achieve the desired surface roughness. Furthermore, the residual stresses in the surface layer resulting from grinding hardening have an unfavorable distribution, with large tensile stresses beneath the hardened layer.

Deformation strengthening of the surface layer during grinding can be an alternative method that eliminates the disadvantages associated with grinding hardening. To ensure high hardness after grinding, grinding parameters should be chosen so that a significant portion of the grinding energy contributes to plastic deformation of the material. Simultaneously, thermal effects should be minimized. To avoid material recrystallization effects, the maximum temperatures in the contact zone should be kept as low as possible. This can be achieved by low cutting speeds combined with small cutting depths. Such grinding conditions allow for combining the shaping process and the mechanical strengthening of the surface layer in a single-stage machining operation [124]. The objectives of the study [125] included determining the effect of grinding depth of C45 steel in a single-stage grinding operation on the susceptibility of pearlite and ferrite to deformation strengthening and characterizing the microstructure of the hardened surface layer. C45 steel was ground to varying depths in the range of 2 to 20 µm, while keeping the other grinding parameters constant, i.e., the peripheral speed of the grinding wheel v_s = 25 m/s and the feed rate v_{ft} = 1 m/min. To determine the changes in the mechanical properties of surface layers after grinding to different depths, caused by changes in the microstructure, and to calculate the density and mobility of dislocations (average dislocation movement velocity) in ferrite grains, nanoindentation tests were performed. Nanoindentation tests were conducted with a constant maximum load of 20 mN using a Berkovich indenter. The load rate increased to the maximum load at 1 mN/s. After reaching the maximum load, it was held for 5 seconds, followed by unloading the indenter over 15 seconds. The hardness tests were carried out within ferrite grains in the strain-hardened zone (within 5 µm from the sample ground surface). To minimize measurement errors, the tests were performed in a room with a constant temperature of 21 °C ± 0.5 °C.

To determine the hardness and stiffness distribution profile of the steel surface layer, a nanoindentation test was also performed on the ground surface. The test involved increasing the load applied to the Berkovich indenter in the range of 100 to 2000 mN. Within this load range, 10 measurements of hardness and contact stiffness were performed at various distances from the ground surface, ranging from 2 to 10 micrometers. During each of the 10 cycles, the indenter load was increased to the maximum value over 20 seconds, held at the maximum load for 5 seconds, and then unloaded over the next 20 seconds.

Fig. 6.6 presents selected results of the indentation test performed on the cross-section of the ground surface layer (Fig. 6a) and on the ground surface (Fig. 6b), with increasing load in the range of 100 mN to 2000 mN. As shown in Fig. 6a, grinding caused an increase in hardness within the surface layer, at a depth of approximately 5 µm from the surface. Using Sneddon's equations and the Oliver- Pharr method, based on the $P = f(h)$ curves in the elastic deformation range of the material (during unloading), the hardness H_{ISE} and the reduced modulus of elasticity E^* were determined. Subsequently, using equations (5.44)-(5.46), assuming f = 2.2 for ferrite grains, the Burgers vector magnitude b = 0.284 nm, and angle θ = 19.72 (for a Berkovich indenter), the density of geometrically necessary dislocations, the dislocation density caused by grinding, and the macroscopic hardness H_0 were calculated. All these values are summarized in Table 6.1. As indicated by the values presented in Table 6.1, grinding to depths ranging from 2 µm to 20 µm results in a significant increase in both hardness and contact stiffness, with the most substantial increases observed for grinding depths of 2 µm and 20 µm. The increase in material hardness and stiffness is associated with an increase in the dislocation density caused by grinding, with the highest dislocation densities observed at grinding depths of 2 µm and 20 µm, amounting to 4.716×10^{15} m^{-2} and 3.740×10^{15} m^{-2}, respectively. For ferrite after normalization annealing, the dislocation density is 1.144×10^{14}.

To create hardness and contact stiffness distribution profiles within the ground layer, an indentation test was conducted in multiload mode. Figure 6.7 presents the hardness distribution profiles (Fig. 6.7a) and stiffness profiles (Fig. 6.7b) within the ground surface layers. As shown in Fig. 6.7, the hardness distribution profiles are well described by exponential functions, while the stiffness profiles are well represented by second-degree polynomials. Fig. 6.7 also indicates that a significant increase in material hardness and stiffness occurs at depths of up to 6-7 micrometers from the ground surface. According to Orowan's theory, only dislocations with low mobility contribute to the increase in material hardness; therefore, to assess dislocation mobility, the recorded deformation behavior as a function of time was analyzed under constant indenter load during the nanoindentation test (Fig. 6.8a). To minimize the influence of geometrically necessary dislocations on the indenter displacement during material creep, the creep test was performed under a load of 1366 mN during the multiload mode. The creep rate was determined by differentiating the linear equation describing the steady-state creep behavior, which was reached approximately 1.7 seconds after the start of the creep test. As shown in Fig. 6.8b, the highest creep rate of 0.0057 s^{-1} was observed

in steel after normalization annealing. As the grinding depth increased, the creep rate decreased, reaching a minimum value of 0.0032 s^{-1} for steel ground to a depth of 14 µm. Using equation (5.53), the average dislocation velocity was calculated (Fig. 6.8b). Given that the highest dislocation density was measured in steel ground to a depth of 2 µm, this result seems evident. However, a more detailed analysis of the dislocation density and its relationship with the average dislocation velocity indicates that although the dislocation density after grinding to a depth of 2 µm is approximately 30% higher than after grinding to a depth of 20 µm, the average dislocation velocity after grinding to a depth of 2 µm is similar to that of ferrite ground to a depth of 20 µm. To explain this phenomenon and assess whether the hardness after grinding is also influenced by stresses generated in the surface layer during grinding, an analysis of the XRD diffractograms was conducted (see Fig. 6.9). According to the Williamson-Hall analysis, the slope of the $Bcos\theta = f(sin\theta)$ function allows for the determination of lattice strain ε, while the intercept with the $Bcos\theta$ axis allows for the determination of crystallite size L. Knowing the material's stiffness E^* at a distance of 2 µm from the ground surface, which was determined in the nanoindentation test, the residual stresses were calculated as $\sigma_R = E^* \cdot \varepsilon$. Table 6.2 summarizes all the results obtained from the Williamson-Hall analysis. As shown by the data presented in Table 6.2, grinding to a depth of 2 µm and 20 µm generates residual stresses of approximately 600 MPa in the surface layer, compared to 150 MPa that occur after normalization annealing.

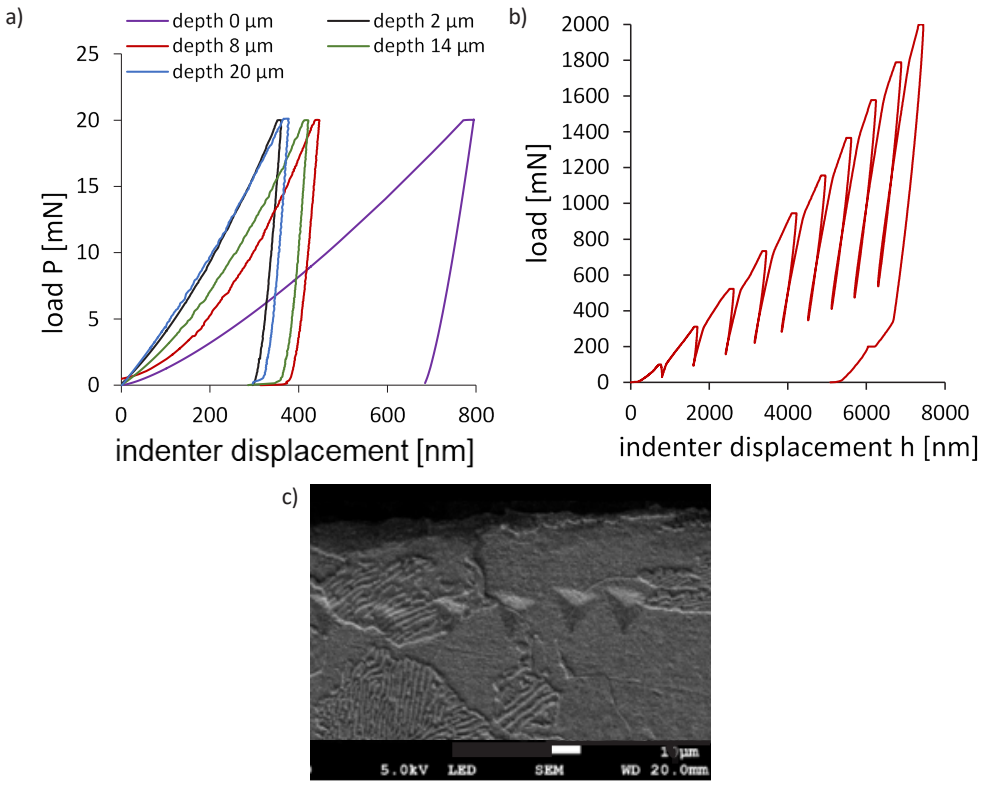

Fig. 6.6. Load-displacement curves obtained from the test performed on the cross-section of ground surface layers (a), and the curve obtained in multiload mode on the surface of steel ground to a depth of 2 µm (b). (c) shows indents in a ferrite grain after the nanoindentation test on the cross-section of steel ground to a depth of 20 µm

Source: based on own research results

Table 6.1

Values characterizing surface layers after grinding to different depths, obtained in the nanoindentation test

	h_c (nm)	ρ_{GND} x 10^{14} (m^{-2})	H_{ISE} (GPa)	ρ_{SSD} x10^{15} (m^{-2})	H_0 (GPa)	E^* (GPa)	(s^{-1})	v (nm/s)
depth 0 µm	754.12	0.84	1.44	0.114	1.09	87.9	0.0057	176.06
depth 2 µm	337.64	1.88	7.16	4.716	7.02	334.0	0.0041	3.061
depth 8 µm	419.97	1.51	4.63	1.899	4.46	235.9	0.0037	6.861
depth 14 µm	395.44	1.61	5.22	2.446	5.06	255.0	0.0032	4.607
depth 20 µm	357.12	1.78	6.4	3.740	6.25	345.7	0.0037	3.483

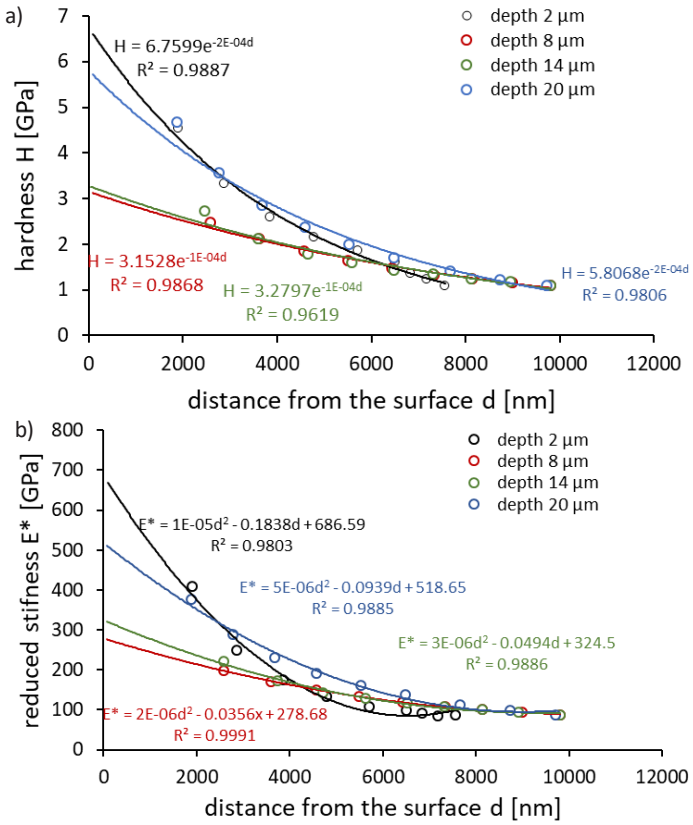

Fig. 6.7. Hardness distribution profiles (a) and stiffness distribution profiles (b) for surface layers after grinding to different depths, determined in the nanoindentation test in multiload mode

Source: based on own research results.

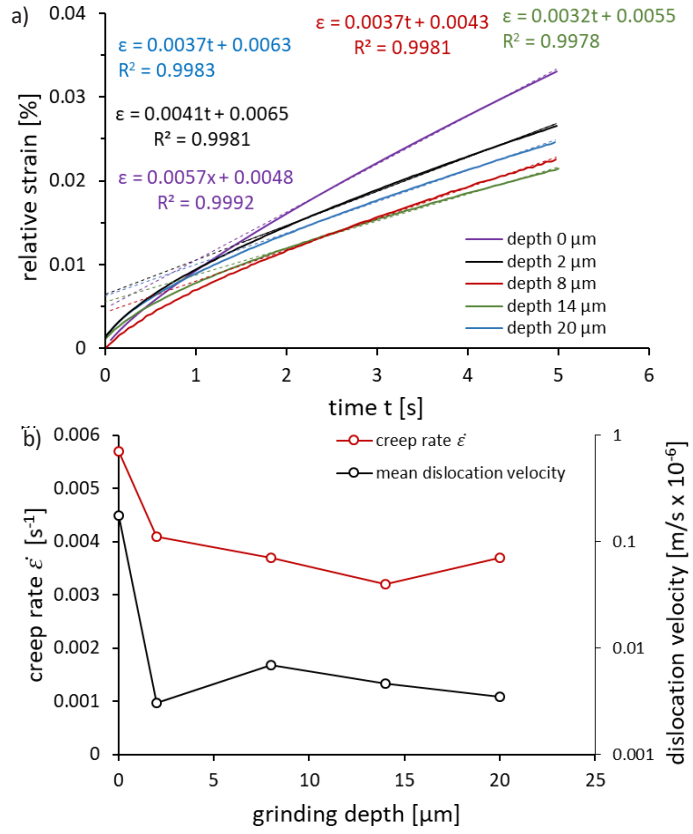

Fig. 6.8. Creep curves under a constant indenter load of 1366 mN (a), and changes in creep rate and average dislocation velocity as a function of grinding depth (b)

Source: based on own research results.

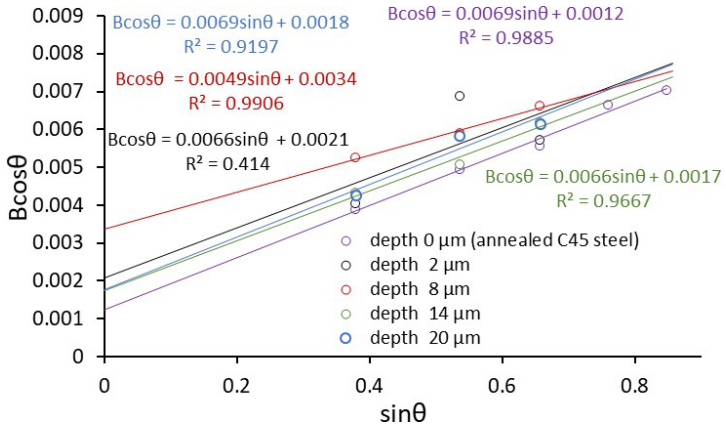

Fig. 6.9. Plots of *Bcosθ* vs. *sinθ* for raw ferrite and after grinding on different depths

Source: based on own research results.

Table 6.2

Microstrain, crystallite size, and residual stress in raw ferrite and after grinding to different depth

	4ε (%)	$a_s \cdot \lambda/L$	L (nm)	E* (GPa)	σ_R (MPa)
annealed ferrite	0.0069	0.0012	128.3333	87.9	151.63
2 µm depth	0.0066	0.0021	73.33333	358.99	592.33
8 µm depth	0.0049	0.0034	45.29412	215.48	263.96
14 µm depth	0.0066	0.0017	90.58824	237.70	392.21
20 µm depth	0.0069	0.0018	85.55556	350.85	605.22

The character of dislocations also contributes to the creep rate. To evaluate the dislocation structure resulting from grinding the steel to different depths, a modified Williamson-Hall analysis was performed. For this purpose, XRD diffractograms were plotted as a function of the diffraction vector $K = 2sin\theta/\lambda$, as shown in Fig. 6.10. Then, similarly to the diffractograms plotted as a function of the 2θ angle, the overlapping peaks were deconvoluted, and the full width at half maximum of the peaks ΔK was determined.

Ferrite has a body-centered cubic (BCC) lattice, which exhibits strong anisotropic properties. The MW-H equation for such materials can be written as follows [126]:

$$\Delta K \cong \frac{a_s}{L} + bM\sqrt{\frac{\pi}{2}\rho}\left(K\bar{C}^{1/2}\right) \tag{6.1}$$

In equation (6.1), ΔK denotes the half-width of the peaks in the diffractogram plotted as a function of the diffraction vector K. M is a dimensionless parameter characterizing the dislocation distribution in the material. ρ and b are the dislocation density and the Burgers vector, respectively, while $\bar{C}$ is the dislocation contrast factor. $\bar{C}$ can be calculated using the following equation [126]:

$$\bar{C} = \bar{C}_{h00}(1 - qH^2) \tag{6.2}$$

In equation (6.2), $\bar{C}_{h00}$ is the average contrast factor for reflections {h00}. $\bar{C}_{h00}$ depends on the contrast coefficient of screw and edge dislocations for reflections {h00}. This coefficient also depends on the proportion of edge and screw dislocations in the dislocation structure. The parameter q indicates the percentage share of screw and edge dislocations in the material structure. In turn, H^2 can be calculated by knowing the Miller indices for the crystallographic planes from which the diffractogram peaks are derived:

$$H^2 = \frac{h^2l^2+h^2k^2+l^2k^2}{(h^2+k^2+l^2)^2} \tag{6.3}$$

The system of equations (6.1) and (6.2) allows for the determination of the parameter q. After substituting equation (6.2) into equation (6.1), one obtains [127]:

$$\frac{(\Delta K-\alpha)^2}{K^2} \cong \beta^2\bar{C}_{h00}(1 - qH^2) \tag{6.4}$$

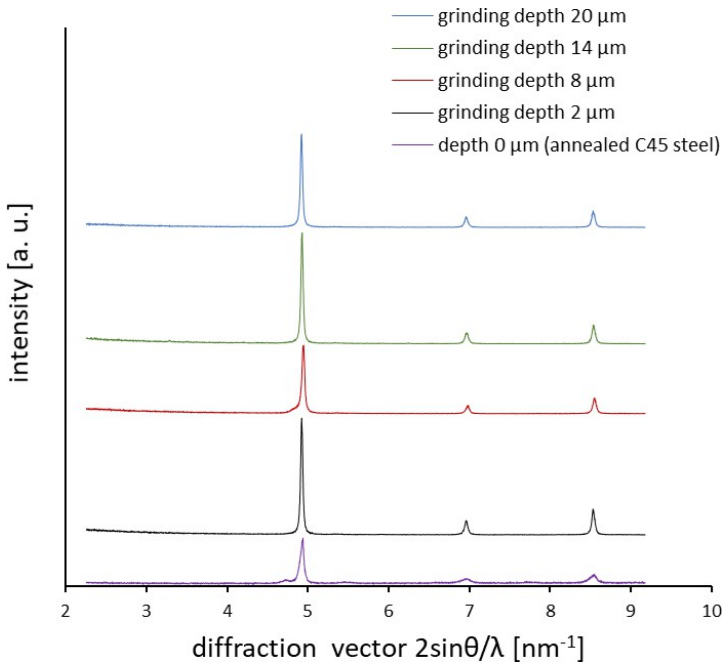

Fig. 6.10. XRD diffractograms as a function of the diffraction vector K

Source: based on own research results.

In equation (6.4), α is the quotient a_s/L and β is the product $bM(\pi\rho/2)^{1/2}$. Assuming in equation (6.4) the linear dependence of the function $(\Delta K\text{-}\alpha)^2/K^2 = f(H^2)$, the parameter $1/q$ can be determined as the point of intersection of the extrapolated line with the H^2 axis. For BCC crystals, the theoretical value of the parameter q for edge dislocations is 1.298, while for screw dislocations the value of this parameter is 2.686. The leverage rule was used to calculate the percentage of screw and edge dislocations in the ferrite grains after grinding. The ends of the lever represent 100% share of screw and edge dislocations, respectively, and the support point of the lever q is determined experimentally as the reciprocal point of intersection of the extrapolated line with the H^2 axis [128]:

$$f^{edge} = \frac{q_{screw}^{th} - q}{q_{screw}^{th} - q_{edge}^{th}} = 1 - f^{screw} \tag{6.5}$$

Fig. 6.11a presents the lines $(\Delta K\text{-}\alpha)^2/K^2 = f(H^2)$, which enable the determination of the q parameter value. The variation of the q parameter as a function of grinding depth is shown in Fig. 6.11b. Using equation (6.5), the percentage of screw and edge dislocations in the surface layers ground to different depths was calculated. The results of these calculations are illustrated in Fig. 6.12. As shown in Fig. 6.12, approximately 68% of the dislocations in normalized ferrite are screw dislocations, while 32% are edge dislocations. The grinding process increases the proportion of edge dislocations in the atomic structure of ferrite, with deeper grinding leading to a higher percentage of edge dislocations. This trend is evident up to a grinding depth of 14 µm. When the grinding depth reaches 20 µm, there is a slight increase in the proportion of screw dislocations compared to the depth of 14 µm. The highest percentage of edge dislocations, 86%, was observed in ferrite ground to a depth of 14 µm.

Figure 6.13 illustrates the microstructure of the surface layer of C45 steel after grinding to different depths. As shown in Fig. 6.13, three distinct zones can be observed in each ground surface layer. X-ray diffraction (XRD) and Energy-dispersive X-ray spectroscopy (EDS) analyses confirm the presence of oxides in the first, near-surface zone. The second zone contains deformed ferrite and pearlite grains, while the third zone maintains its original structure. In the second zone, the spacing between the ferrite and cementite lamellae is significantly reduced compared to the third zone. Metallographic analysis indicates that increasing the grinding depth causes the first zone to thicken, while simultaneously reducing the thickness of the second zone. In the sample ground to a depth of 2 µm, magnetite (Fe_3O_4) is detected in the first zone, whereas in the sample ground to 20 µm, the oxide layer consists of a mixture of magnetite and hematite (Fe_2O_3). This composition suggests that deeper grinding leads to higher surface temperatures during the process. However, the temperature rise remains below the pearlite-to-austenite transformation temperature for C45 steel, which is 1001 K. The rapid heating of the surface layer during grinding could increase the pearlite-to-austenite transformation temperature, but the absence of refined pearlite grains post-grinding suggests that no austenitic transformation occurred. Additionally, the lack of wustite (FeO) indicates that grinding to 2 µm did not elevate the surface temperature above 843 K. The most favorable microstructure in Zone I is observed after grinding to a depth

of 2 µm, as the oxide layer is the thinnest, remains well-adhered to the substrate, does not peel off, and is the most compact. The surface structure of C45 steel post-grinding was analyzed using the Electron Backscatter Diffraction (EBSD) method. The analysis results showed a diverse crystallographic texture (Fig. 6.14a) and a variation in ferrite grain size distribution (Fig. 6.14b) in the surface layers examined. After grinding, the ferrite grains exhibited a reduction in their average size compared to the original structure, a characteristic feature of plastic deformation caused by the grinding process. The crystallographic orientation analysis revealed a preferential grain orientation, indicating the formation of texture during the grinding process. The EBSD analysis also detected both low-angle and high-angle grain boundaries, which point to complex deformation mechanisms at work on the steel surface during grinding.

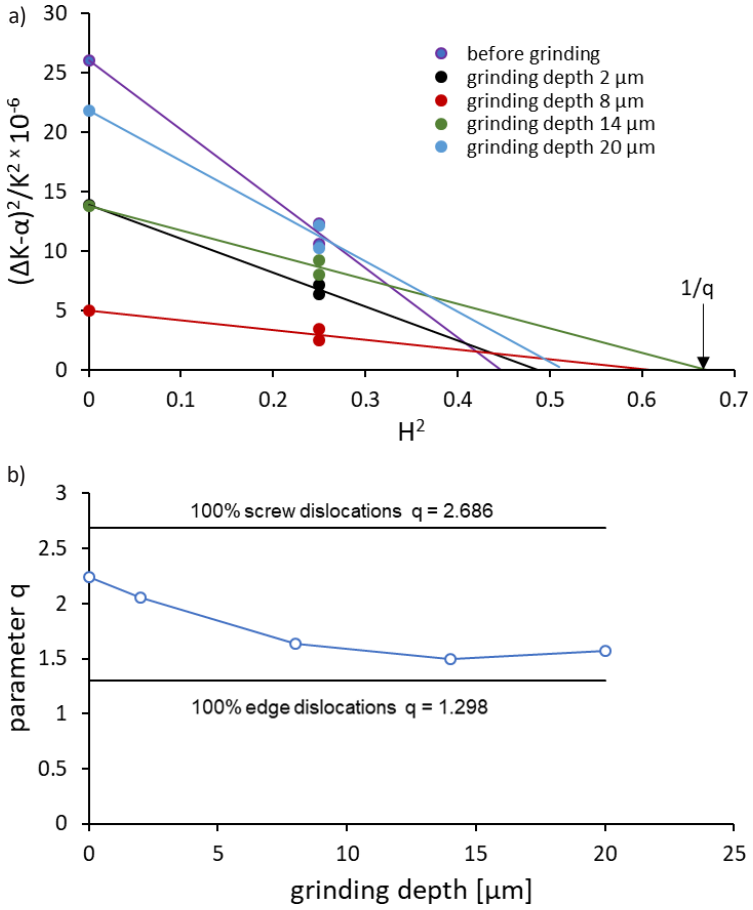

Fig. 6.11. The plot of equation (6) for annealed ferrite and after grinding it to a different depth. The reciprocal of the intersect on the H^2 axis gives $1/q$. (a) and the change in the q parameter value as a function of grinding depth (b)

Source: based on own research results.

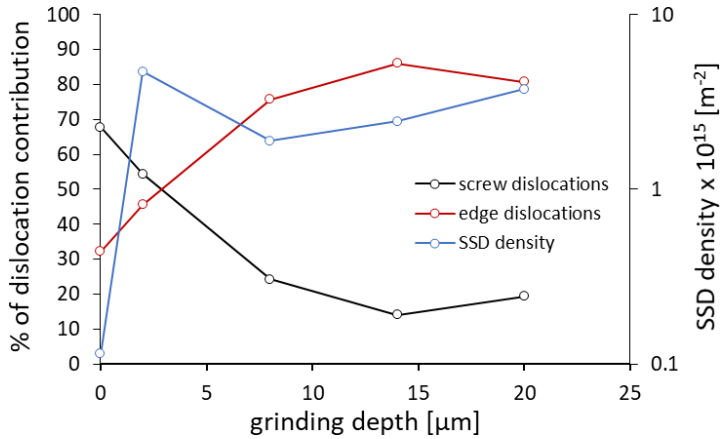

Fig. 6.12. Changes in dislocation density and the percentage of screw and edge dislocations in ferrite after grinding to various depths

Source: based on own research results.

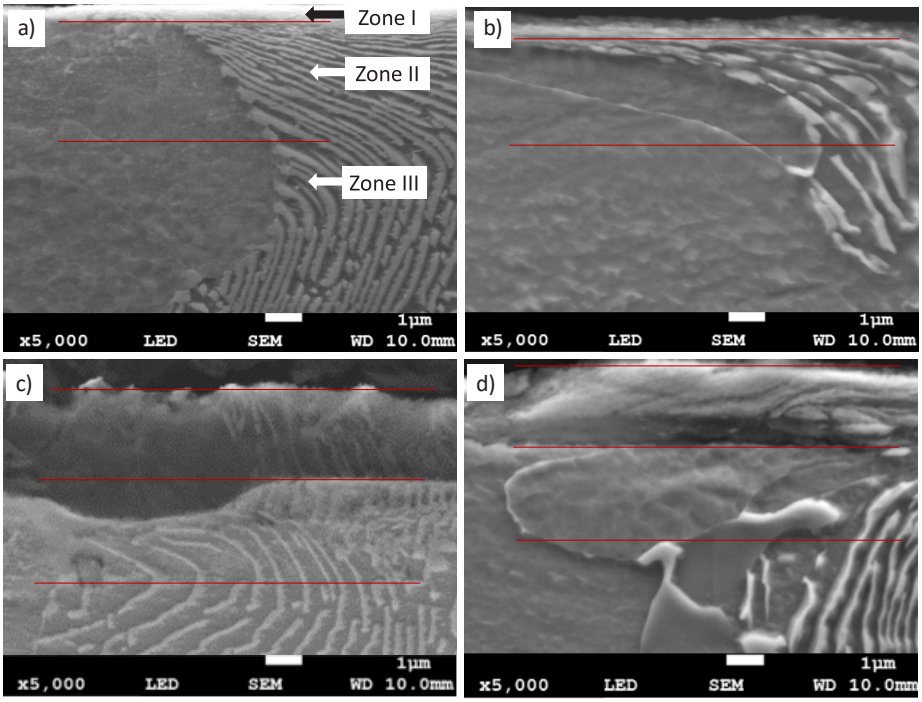

Fig. 6.13. Microstructure of surface layer of the C45 steel after grinding to a depth ranging from 2 µm to 20 µm. Three zones of the surface layer are visible. Microstructure of surface layer after grinding to 2 µm (a), 8 µm (b), 14 µm (c) and 20 µm (d)

Source: based on own research results.

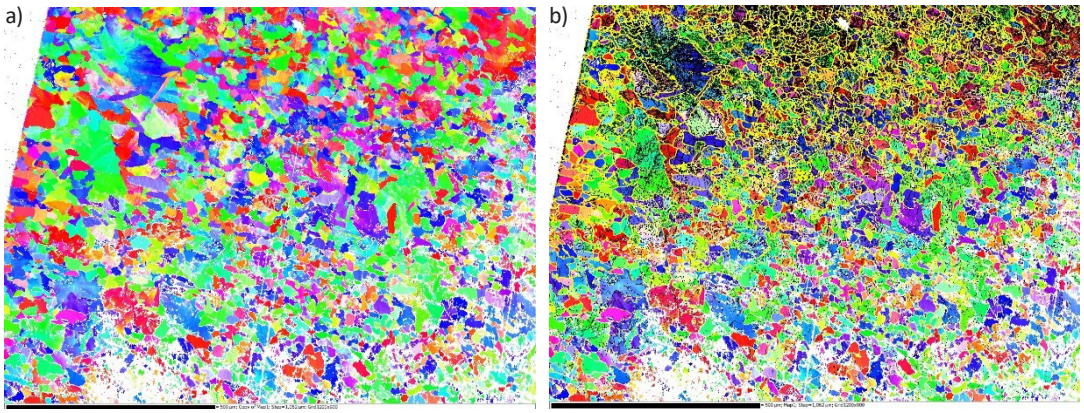

Fig. 6.14. Crystallographic orientation of grains in the surface layer of C45 steel after grinding to a depth of 2 µm (a) and grain and sub-grain boundaries in the surface layer(b)

Source: based on own research results.

To achieve high surface quality, grinding must be carried out under optimal conditions. An important aspect in this context is the minimization of surface roughness. The depth of grinding has a significant impact on the surface quality after grinding and the efficiency of the process. To assess this, a nanoindentation system was used as an atomic force microscope, and scans of the ground surfaces were performed. Surface topographies were obtained using a non-contact mode with a force of 55 mN over an area of 50 × 50 µm. The surface roughness parameter Sa was determined using software included with the device. Figure 10 shows the surface topography of a 50 µm × 50 µm area after grinding to different depths. As shown in Figure 6.15, an increase in grinding depth leads to an increase in surface roughness, expressed by the Sa parameter. During grinding, the workpiece is subjected to tangential and normal forces relative to the ground surface. These forces increase with the increase in grinding depth; however, the normal force rises much faster than the tangential force [129]. The undeformed chip thickness of a single grain increases, which leads to the deterioration of the surface roughness of the workpiece and an increase in normal force. Increasing the chip thickness of a single grain also changes the material removal mechanism. It transitions into a mechanism of friction and ploughing, which further aggravates the surface roughness of the workpiece [130]. As the grinding depth

increases, the temperature of the workpiece also rises, which reduces its yield strength. Lower yield strength leads to greater deformation under tangential and normal forces, which also contributes to increased surface roughness.

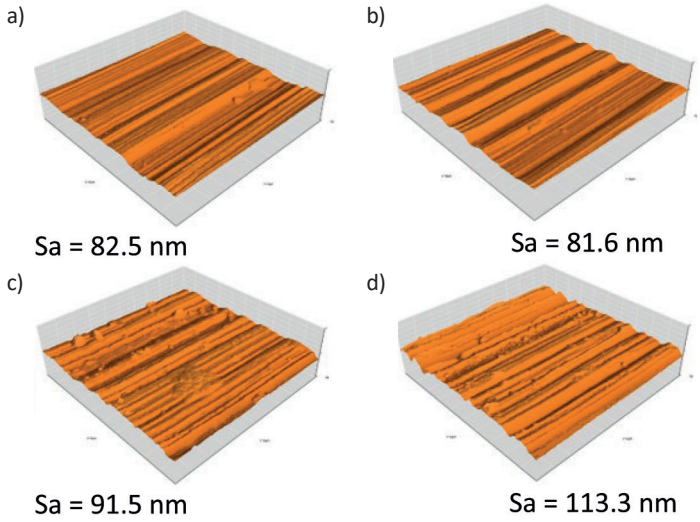

Fig. 6.15. Topographies of surfaces grinded to a depth of 2 µm (a), 8 µm (b), 14 µm (c) and 20 µm (d)

Source: based on own research results.

The results presented indicate that nanoindentation testing is an appropriate tool for characterizing C45 steel, which, while not a new material, has been processed in a novel way. It demonstrates that nanoindentation can successfully be employed to evaluate the mechanical properties of established materials that have undergone innovative processing techniques. This highlights the versatility and effectiveness of nanoindentation in assessing both new materials and those re-engineered through advanced methods. The presented research results demonstrated that the indentation test not only enabled the determination of the hardness and stiffness distribution in the surface layer of ground steel with a thickness of approximately 10 µm, but also facilitated the calculation of dislocation density in the surface layers. In combination with XRD diffractogram analysis, it also allowed for the identification of screw and edge dislocation densities within the atomic structure of ferrite. Furthermore, the determination of the ferrite's stiffness (E*) enabled, in conjunction with Williamson-Hall analysis, the calculation of residual stresses in the surface layer and the assessment of their nature. Moreover, using the indentation system, it was also possible to obtain the topography of the ground layers and, based on this, assess the quality (roughness) of the ground layers.

6.3. Determination of Residual Stresses in Laser-Processed Aircraft Landing Gear Struts

The information presented in this chapter was included in the publication [131]. The laser beam is a chemically clean energy source and can be used, among other things, to shape the properties of the processed surface layer. Rapid heating followed by rapid cooling of the material, depending on the applied laser beam parameters, can alter the microstructure and generate residual stresses, leading to changes in the mechanical properties of the treated surface layer. Compared to conventional hardening, laser hardening does not require the use of toxic coolants, which have a negative impact on the environment. The use of laser hardening also addresses the issue of coolant disposal, significantly reducing production costs. Due to these advantages, lasers are increasingly used in the manufacturing of machine components and equipment [132, 133]. There are numerous literature reports describing the beneficial effects of laser processing on the fatigue failure of various steel grades [134-137]. These reports indicate that the fatigue resistance of laser-treated steel is mainly dependent on the distribution of residual stresses generated by the laser treatment. However, the values and distribution of residual stresses after laser treatment will depend on the parameters of the treatment as well as the size and shape of the workpiece. Additionally, the proper design and placement of laser-treated paths on the surface of the workpiece can contribute to increased fatigue resistance by generating favorable stresses between the molten paths and the base material. There are few studies in the literature that describe the distribution of residual stresses in the areas of unchanged microstructure between the laser-melted paths. The scientific objective of the study [131] was to determine how the state of residual stresses and mechanical

properties after laser melting influence the initiation of fatigue cracks in the eye of the landing gear tie rod made of high-strength 30HGSNA steel. Nanoindentation testing was used to determine residual stresses in the melted material (LT), in the heat-affected zone (HAZ), and in the base metal (BM) located between the melted paths. The landing gear tie rod consisted of two parts: the main part, made of a seamless tube with a wall thickness of 6.5 mm, and the eye. The main part of the tie rod was welded to the eye with a butt weld (Fig. 6.16). Fatigue tests simulating the stresses during aircraft landing showed that the tie rod without laser treatment of the eye endured 503 simulated landings and fractured at the eye (Fig. 6.17b). In contrast, the tie rod with laser treatment of the eye, as shown in Fig. 6.15, withstood 1701 simulated landings before fracturing at the weld between the eye and the sleeve of the tie rod (Fig. 6.17a). To explain the high fatigue resistance of the laser-treated tie rod, indentation tests were performed on the cross-section of the eye. Measurements were taken before annealing and after stress-relief annealing along two lines shown in Fig. 6.18a. The test locations on the cross-sections corresponded to the areas of highest stress during fatigue tests (Fig. 6.18b).

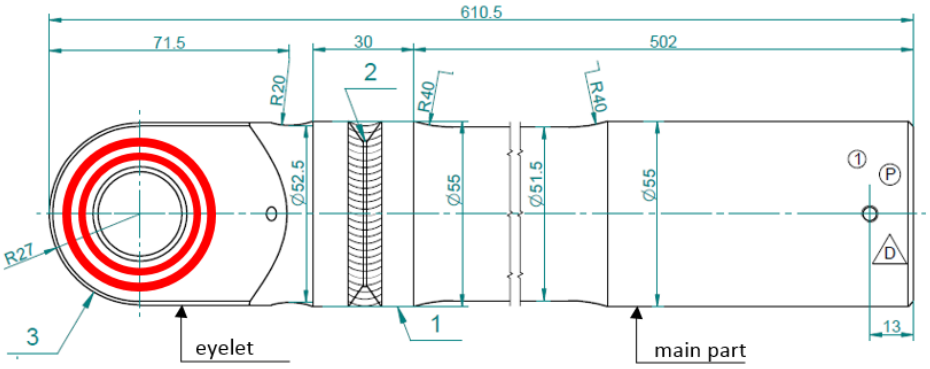

Fig. 6.16. Shape and dimensions of the aircraft landing gear tie rod. The red areas indicate laser-melted paths

Source: based on own research results [131].

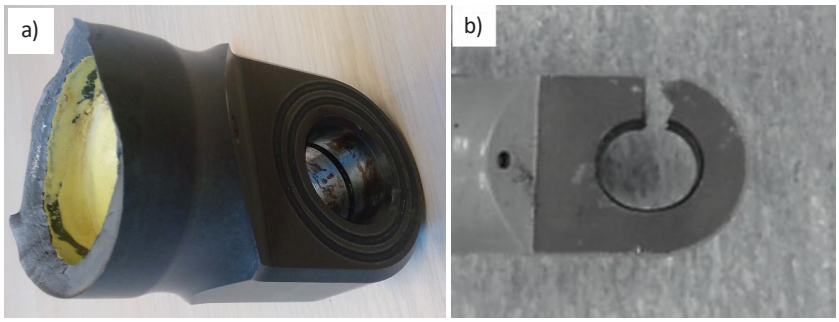

Fig. 6.17. View of the landing gear lug subjected to laser treatment (a) and the untreated lug (b) after fatigue testing

Source: based on own research results [131].

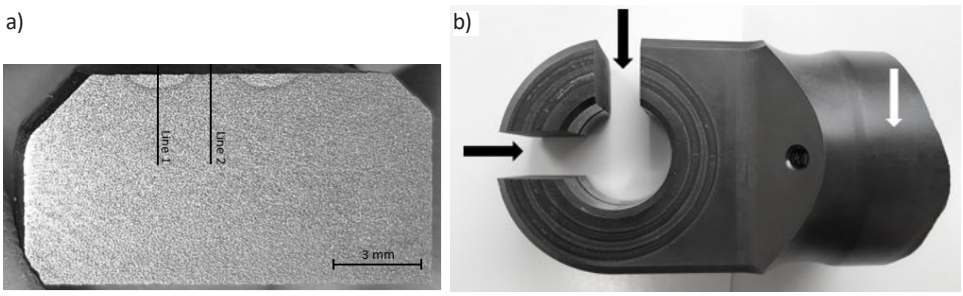

Fig. 6.18. Cross-sectional view of the lug of the aircraft tie rod with marked lines along which the indentation test was performed (a) and a view of the tie rod with sample collection points for testing (b)

Source: based on own research results [131].

Since fatigue crack initiation usually occurs on the surface of the material or just below it, it was crucial to determine the material properties as close to the surface as possible. On the other hand, due to the laser melting depth

of approximately 800 µm, it was also necessary to conduct tests at greater depths relative to the surface. Therefore, both the indentation test on the laser-melted surface with increasing load ranging from 100 mN to 20 N (multiload) and measurements along the cross-section lines shown in Fig. 6.18a were performed. Fig. 6.19 shows the hardness distribution changes in the laser-melted track, while Fig. 6.20 illustrates the hardness distribution changes in the material between two laser-melted tracks. Both figures also indicate the hardness of the material before laser treatment, which was 6 GPa. As shown in Figs. 6.19 and 6.20, laser melting significantly increased the material's hardness, while the material between the two melted tracks only experienced a slight change in hardness.

In turn, Fig. 6.21 shows changes in surface elasticity, meaning the changes in the proportion of elastic deformation work of the material relative to the total deformation work performed during the indentation test (see Fig. 5.15) in the laser-remelted track, while Fig. 6.22 presents the changes in the elasticity of the material located between the two remelted tracks. Both figures also indicate the material elasticity before laser treatment, which was 18%. As shown in Figs.

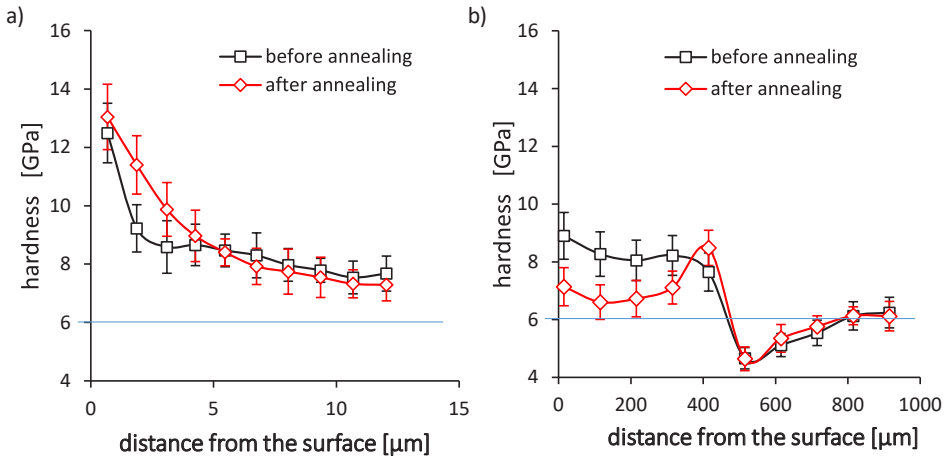

Fig. 6.19. Hardness distribution profiles in the laser-treated (LT) path before and after stress-relief annealing, in the range from 0 to 13 µm (multiload) (a), and in the range from 15 µm to 915 µm performed on a cross-section (b). Error bars represent ± standard deviation from five measurements

Source: based on own research results [131].

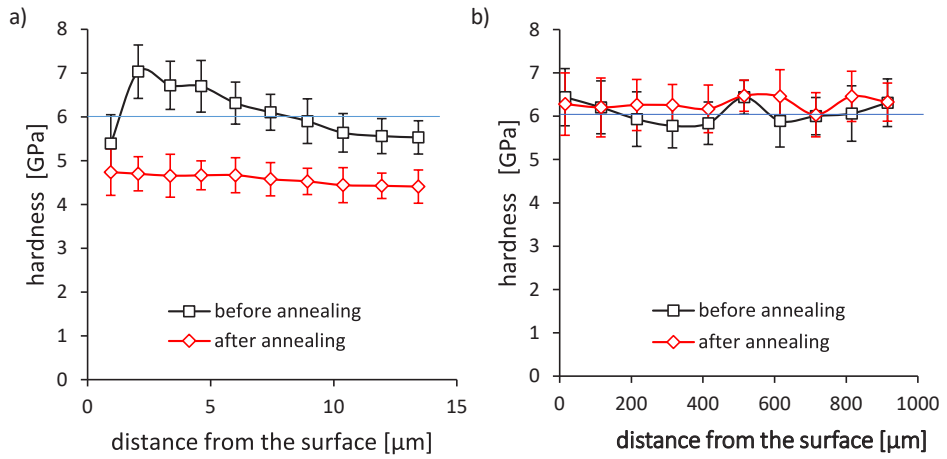

Fig. 6.20. Hardness distribution profiles in the material between the laser-treated paths (BM) before and after stress-relief annealing, in the range from 0 to 13 µm (multiload) (a), and in the range from 15 µm to 915 µm performed on a cross-section (b). Error bars represent ± standard deviation from five measurements

Source: based on own research results [131].

Figures 6.21 and 6.22, laser remelting significantly increased the material's elasticity, and the material located between the two remelted tracks also exhibited increased elasticity compared to the native material.

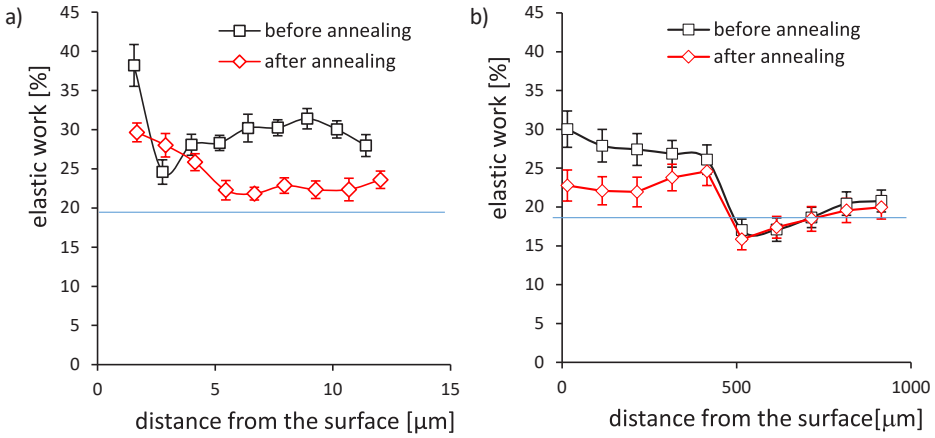

Fig. 6.21. Profiles of material elasticity distribution in the laser remelted LT track before and after stress-relief annealing in the range from 0 to 13 µm (multiload) (a) and in the range from 15 µm to 915 µm, taken on the cross-section (b). Error bars represent ± the standard deviation from five measurements

Source: based on own research results [131].

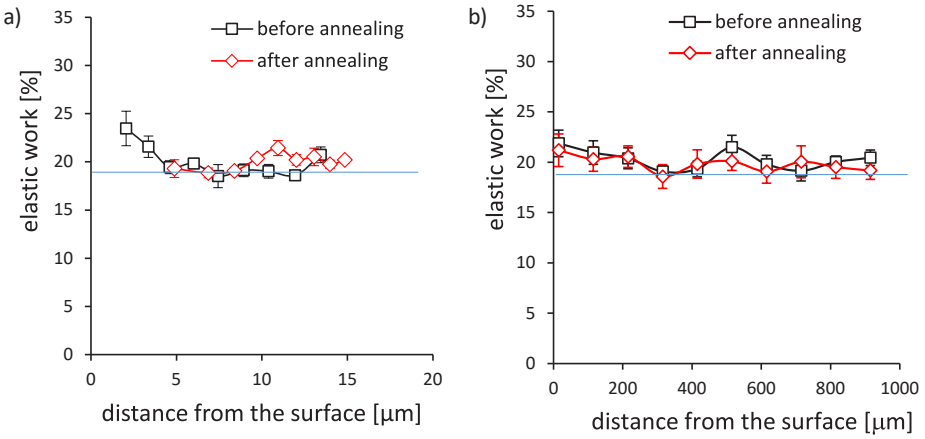

Fig. 6.22. Profiles of material elasticity distribution between the remelted BM tracks before and after stress-relief annealing in the range from 0 to 13 µm (multiload) (a) and in the range from 15 µm to 915 µm, taken on the cross-section (b). Error bars represent ± the standard deviation from five measurements

Source: based on own research results [131].

Next, using equation (5.60), residual stresses were determined both in the laser-remelted track and in the material with unchanged structure located between the two remelted tracks (see Fig. 5.21). Figures 6.23 and 6.24 present the residual stress distribution profiles in the laser-remelted material and in the material located between the two laser-remelted tracks.

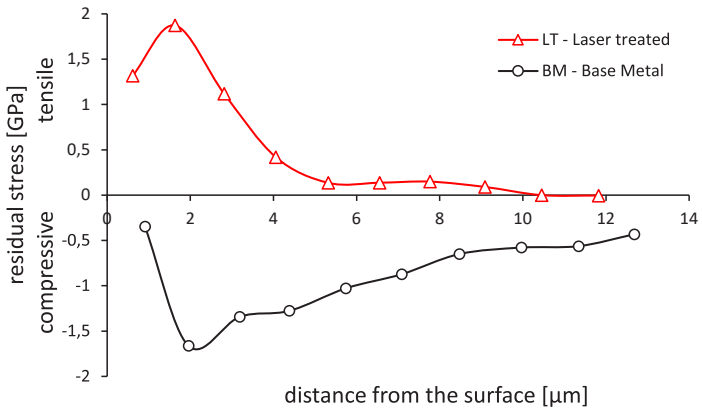

Fig. 6.23. Profiles of residual stress distribution along “line 1” (LT) and “line 2” (BM) at a distance from the surface in the range from 1 µm to 13 µm

Source: based on own research results [131].

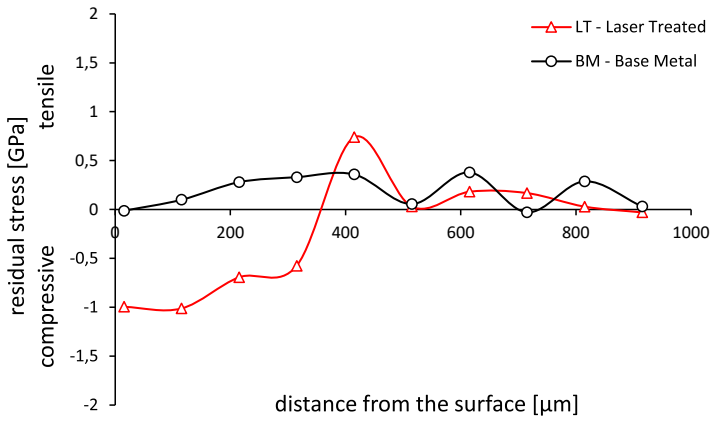

Fig. 6.24. Profiles of residual stress distribution along "line 1" (LT) and "line 2" (BM) at a distance from the surface in the range from 15 µm to 915 µm

Source: based on own research results [131].

As shown in Figs. 6.23 and 6.24, in the laser-remelted material at depths up to 4 µm, significant tensile residual stresses in the range of 0.42–1.87 GPa are present. At depths of 11–360 µm, the stresses are compressive in nature. Conversely, in the material located between the remelted tracks, the situation is reversed: significant compressive stresses occur near the surface, while deeper layers exhibit tensile stresses. From the presented research results, it can be inferred that the high compressive stresses, up to 1.6 GPa, present near the surface of the material between the two laser-remelted tracks, inhibited the initiation of fatigue cracks. On the other hand, in the laser-remelted material, the high tensile stresses near the surface, up to 1.87 GPa, did not lead to rapid fatigue crack initiation, because the material at that location was characterized by high hardness and elasticity, which compensated for the effects of the tensile stresses.

This section emphasizes that the nanoindentation method can successfully be used to characterize 30HGSNA steel, which, although it has been used in industry for many years, has been processed in a new way through laser surface treatment. The nanoindentation test not only allowed for determining the hardness of the laser-remelted areas of the aircraft landing gear struts and the areas on the surface of the struts located between the remelted zones, but also enabled the determination of residual stress distributions from the surface into the material and the identification of the nature (compressive or tensile) of these stresses.

Moreover, the nanoindentation test enabled the determination of the elastic properties of the surface. While there is no strict definition of elastic properties for a material, this term is commonly used in materials engineering. In the case of the indentation test, the elastic properties of the material were determined by measuring the work of the material's elastic response during unloading from the indenter and calculating its percentage contribution to the total work of the material's deformation (elastic-plastic) during the test. Another advantage of the nanoindentation test is the ability to very precisely select the area in which the material is characterized, in this case including laser-remelted material, the heat-affected zone, and the areas between the remelted tracks.

All of this makes the nanoindentation test an effective method for characterizing laser-processed metallic materials, especially in the context of their resistance to wear caused by fatigue.

6.4. Characterization of Al_2O_3 Layers Produced by Micro-Arc Oxidation (MAO) for their Cavitation Load Resistance

The information presented in this chapter has been published in [138].

Aluminum alloys are widely used in machinery and equipment construction due to their advantages, including low density, good strength, and excellent corrosion resistance in humid environments. For these reasons, aluminum alloys are extensively employed in the aerospace industry [139–142], in the construction of high-speed vessels [143, 144], and in the automotive industry [145–147]. However, many machine and equipment components made from aluminum alloys exhibit low resistance to tribological wear and low resistance to cavitation erosion. These shortcomings of aluminum alloys often limit their application. To improve the tribological properties and cavitation

erosion resistance of aluminum alloys, various protective coatings are used [148, 149]. One of the most promising methods for producing protective coatings is micro-arc oxidation (MAO), which allows for the creation of ceramic Al_2O_3 coatings on aluminum alloys that provide high hardness. It is known that the properties of protective coatings depend on the production parameters and the phase composition of the coating [150–152]. However, there is no consensus on which mechanical properties provide the best cavitation erosion resistance for the coating. For example, Jafarzadeh et al. [153] demonstrated that higher hardness did not correlate with increased cavitation erosion resistance in thermally sprayed Al_2O_3 + TiO_2 coatings. According to these authors, discontinuities in the microstructure were more important for cavitation erosion resistance than the hardness of the coatings. In contrast, Zou et al. [154] studied Al-Si alloys produced by selective laser melting (SLM). They found that the higher hardness of the alloys, achieved by adjusting production parameters, provided better resistance to cavitation erosion.

There are also examples in the literature of materials with greater cavitation erosion resistance due to better surface elastic properties, as determined by nanoindentation testing. For example, the authors of [155] indicated that solution treatment slightly decreased the hardness of high-nitrogen austenitic stainless steel but significantly increased its elasticity, which in turn improved its resistance to cavitation loading. The authors attributed the greater cavitation resistance of the steel with higher elastic properties to the surface's ability to absorb the energy generated by collapsing bubbles. Cheng et al. [156] studied the cavitation resistance of MAO coatings made from 2124 aluminum alloy. They found that cavitation erosion was caused by the brittle cracking of the MAO coating. This conclusion suggests that greater resistance to brittle cracking, expressed by a higher critical stress intensity factor, should provide better cavitation resistance. Another parameter described in the literature that characterizes the cavitation erosion resistance of both bulk materials and coatings is the hardness-to-elastic modulus ratio (H/E). This ratio describes the material's resistance to elastic deformation. However, when considered in isolation, this parameter does not seem sufficient for evaluating cavitation erosion resistance. This conclusion is supported by the observation in [156] that the cavitation erosion resistance of MAO coatings was inversely proportional to their H/E ratio.

Since cavitation loading occurs cyclically, the literature also provides information on the relationship between cavitation erosion resistance and fatigue strength. Generally, higher fatigue strength ensures greater cavitation erosion resistance. However, the tensile residual stresses introduced by the MAO process may be a key factor in reducing fatigue strength and, consequently, lowering cavitation erosion resistance, as they accelerate crack growth [157].

Based on the reviewed literature, it cannot be conclusively stated which mechanical properties of MAO coatings provide the best cavitation erosion resistance. Therefore, the scientific goal of the study [138] was to determine which mechanical properties of MAO coatings ensure the highest cavitation erosion resistance. To assess the impact of mechanical properties on the cavitation resistance of two MAO coatings with different phase structures, a cavitation test, a nanoindentation test, and a scratch test were conducted. The MAO coatings were produced on two aluminum alloys: 5056 and 7075. The coating on the 5056 alloy consisted entirely of the γ- Al_2O_3 phase. This coating had a white color and was labeled WC. The coating on the 7075 alloy consisted of 19.7% α- Al_2O_3 phase and 80.3% γ- Al_2O_3 phase. This coating had a dark color and was labeled BC. Both coatings and the 5056 alloy, which served as a reference material, were subjected to cavitation loading using a magnetostrictive system for a maximum period of 780 minutes.

The cavitation tests allowed for the determination of cavitation erosion behavior, including cumulative mass loss over time and the rate of mass loss. From these curves, single-value parameters characterizing the cavitation resistance of the materials under cavitation loading were determined. These parameters included the incubation period (τ_{inc}), i.e., the time after which measurable material losses due to cavitation erosion began, the inverse of the maximum cumulative erosion rate $(MCER)^{-1}$, the time at which the maximum mass loss rate occurred (τ_{MCER}), and the R parameter, which is the inverse of the relative area (compared to the reference material) under the cumulative mass loss curve over the 0–420 minute period.

In the nanoindentation test, hardness (H), longitudinal elastic modulus (E), and the percentage of elastic work during total deformation work (W_{el}) were determined. Using equation (5.67), critical stress intensity factors (K_{IC}) for the produced coatings were also calculated (Figs. 6.25 and 6.26). A scratch test was also performed. Figure 6.27 shows the surfaces of the MAO coatings and the 5056 aluminum alloy after the scratch test, where the normal force increased from 0 N to 1.5 N. White arrows indicate the locations of cracks in the MAO coatings. For the BC coating, a crack initiated at a load of P_{cr} = 996 mN, running parallel to the scratch groove. For the WC coating, cracking occurred at a higher load of P_{cr} = 1150 mN and developed within the scratch groove. Additionally, delamination occurred in the WC coating at a load of P_{del} = 1500 mN (black arrow in Fig. 6.27). In the case of the 5056 aluminum alloy, no cracking occurred during the scratch test. Only plastic grooving was observed for the reference material.

Figure 6.28 presents the changes in scratch depth and coefficient of friction recorded during the scratch test: 0.047–0.32 for the WC coating and 0.057–0.24 for the BC coating. For the 5056 aluminum alloy, the coefficient

of friction ranged from 0 to 0.65. The greatest penetration depth was observed for the 5056 alloy, while the MAO coatings exhibited the least penetration depth.

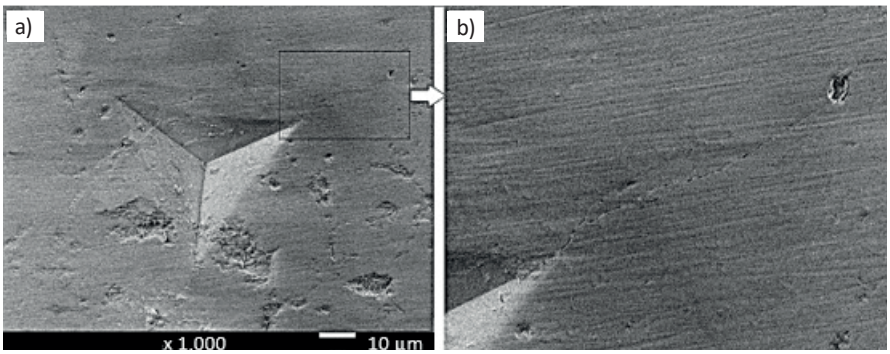

Fig. 6.25. View of the nanoindentation imprint for the BC coating (a) and a magnified view of the crack (b)

Source: reproduced with permission from [138].

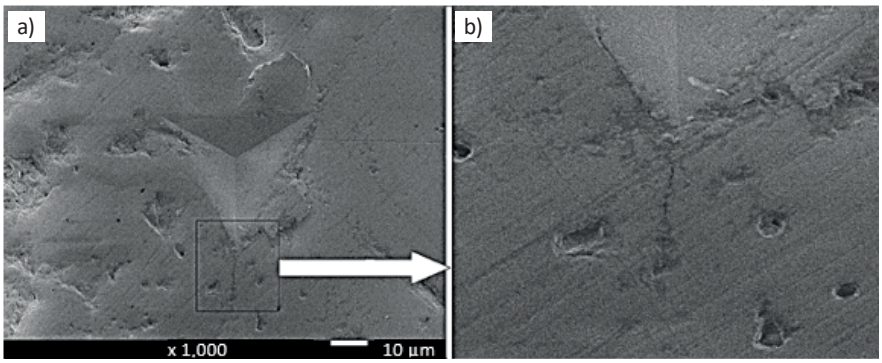

Fig. 6.26. View of the nanoindentation imprint for the WC coating (a) and a magnified view of the crack (b)

Source: reprodu permission from [138].

The parameters describing cavitation resistance and characterizing the mechanical properties of MAO coatings, determined in the indentation and scratch tests, are summarized in Table 6.3. Based on the data collected in this table, graphs were created to illustrate the relationship between the materials' properties and their cavitation resistance (Figs. 6.29–6.31). The results indicate a monotonic relationship between the cavitation resistance of the tested materials, expressed both by the $(MCER)^{-1}$ index and the R index, and their hardness, H/E ratio, and surface elasticity (W_{el}). On the other hand, no correlation was observed between cavitation erosion resistance and fracture toughness, expressed by the K_{IC} coefficient. In this case, cavitation erosion resistance is inversely proportional to fracture toughness. It can also be concluded that the cavitation erosion resistance of MAO coatings depends on the continuity of the microstructure, characterized by less variability in the coefficient of friction in the scratch test.

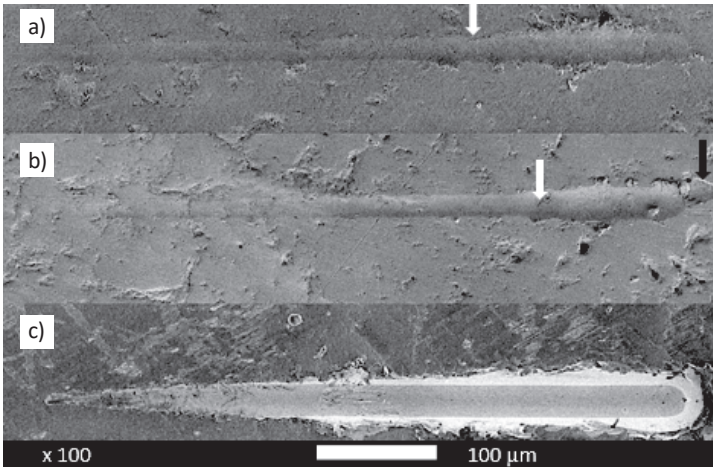

Fig. 6.27. View of the scratch on the surface of the BC coating (a), the WC coating (b), and the 5056 aluminum alloy (c)

Source: reproduced with permission from [138].

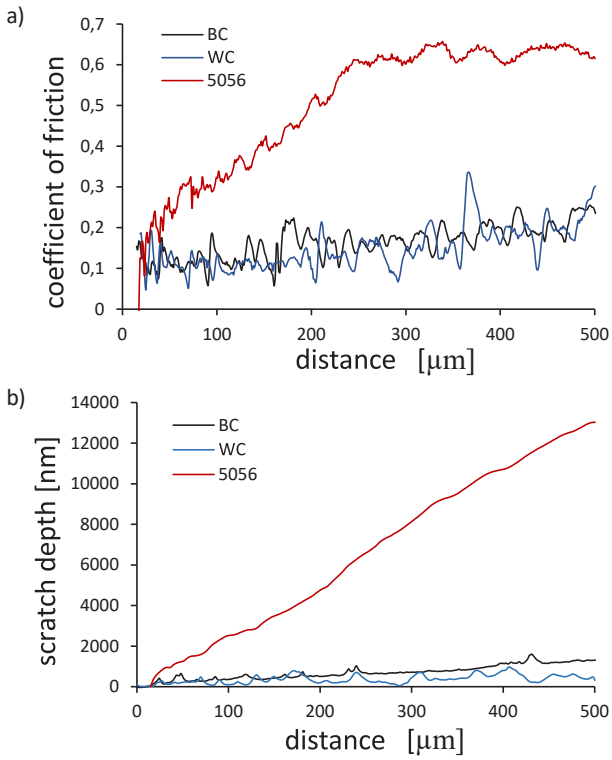

Fig. 6.28. Coefficient of friction as a function of the indenter's path (a) and scratch depth as a function of the indenter's path (b)
Source: own work based on [138].

Table 6.3

Parameters describing cavitation resistance and characterizing the mechanical properties of MAO coatings determined in the indentation and scratch tests [138].

	R [-]	$(MCER)^{-1}$ [min/mg]	τ_{inc} [min]	τ_{MCER} [min]	H [GPa]	E [GPa]	K_{IC} [MPa·m$^{1/2}$]	P_{cr} [N]	P_{del} [N]	W_{el} [%]
WC	2,68	20	70	150	8,25	151,75	7,78	1,150	1,5	39,6
BC	3,98	32,25	80	120	9,84	143,69	4,82	0,996	-	44,5
5056	1	11,49	0	240	1,18	71	27*	-	-	25,7

Based on [158] for a similar aluminum alloy 5083
Source: own work based on [138].

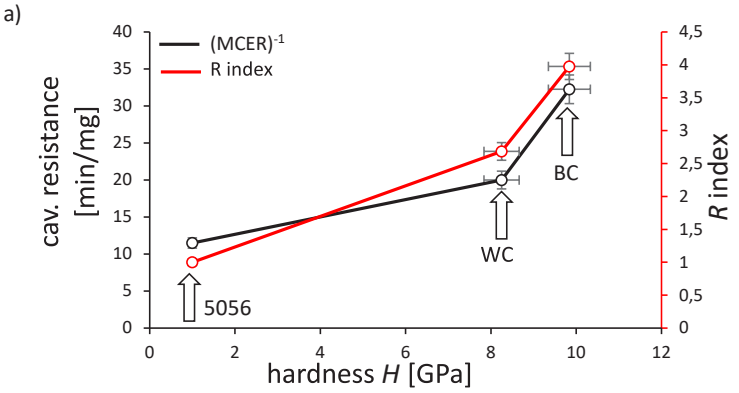

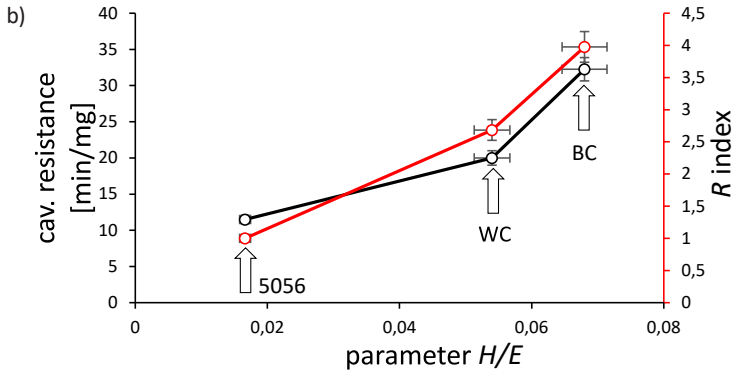

Fig. 6.29. Changes in cavitation erosion resistance as a function of surface hardness (a) and as a function of the H/E ratio (b). Error bars represent ± the standard deviation of the measurements

Source: own work based on [138].

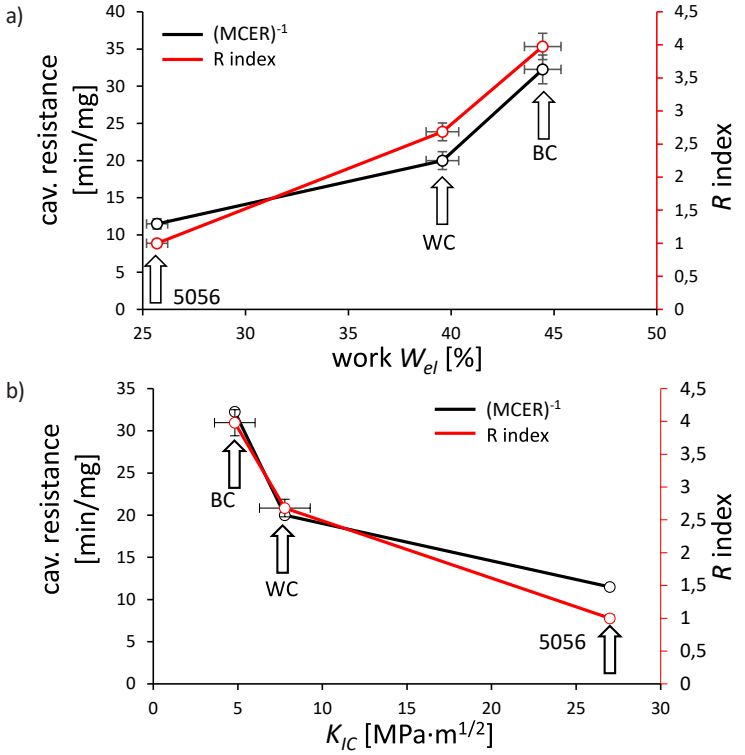

Fig. 6.30. Changes in cavitation erosion resistance as a function of the elastic properties of the eroded surface (W_{el}) (a) and as a function of the K_{IC} coefficient (b). Error bars represent ± the standard deviation of the measurements

Source: own work based on [138].

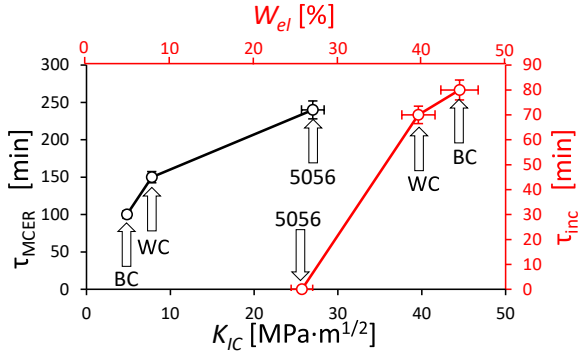

Fig. 6.31. The influence of the K_{IC} coefficient on the time at which the material begins to erode at the maximum rate, and the relationship between the elastic deformation work (W_{el}) and the incubation period. Error bars represent ± the standard deviation of the measurements

Source: own work based on [138].

The cavitation erosion resistance of MAO coatings also depends to a greater extent on their resistance to delamination under cavitation loading, and to a lesser extent on their resistance to cracking under such loading.

The presented results indicate that the indentation test and the scratch test can successfully be used to characterize the cavitation resistance of Al_2O_3 coatings produced on aluminum alloys using modern Micro Arc Oxidation technology. The use of the nanoindentation test as a research tool not only allowed for the determination of commonly used surface engineering parameters, such as H/E or H^3/E^2, which are used to describe the wear resistance of various engineering materials, but also enabled the determination of the stress intensity factor (K_{IC}) for the produced coatings and the correlation of this property with their resistance to cavitation-induced loads. Additionally, the elastic deformation work (W_{el}) of the Al_2O_3 ceramic was used to characterize the cavitation resistance of the produced surface layers, which was also determined in the same experiment as the other properties, such as hardness, contact stiffness, or stress intensity factor. This demonstrates that the indentation test is a highly efficient research tool. Using the same testing setup, a scratch test was also conducted, which allowed for the characterization of both the coefficient of friction, which depended on the density and continuity of the Al_2O_3 structure, as well as the cohesive strength of the coating itself and the adhesive strength of the coating to the substrate.

6.5. Characterization of Composite Coatings Based on Carbon Nanowalls–Polydopamine–Polyzwitterion

The information presented in this chapter has been published in [159]. The development of medical therapies for diseases or disorders related to mental or neurodegenerative conditions, such as Parkinson's disease, attention deficit disorder (ADD), or schizophrenia, requires the use of precise and cost-effective tools for in situ measurement of dopamine concentration in synaptic gaps and the interstitial fluid of nervous tissue [160]. Two main types of sensors are used for measuring dopamine concentration: fluorescence sensors and electrochemical sensors for neurotransmitters and neuromodulators. The greatest advantage of electrochemical sensors for neurotransmitters and neuromodulators is their very high temporal resolution compared to fluorescence sensors [160]. Moreover, this detection method does not require the introduction of carefully designed viral vectors (e.g., adenoviruses) capable of expressing desired fluorescent markers into the tissue. However, the most critical drawback of electrochemical sensors is their relatively low spatial resolution [160], which unfortunately does not allow for precise imaging of transmission and modulation of individual neurons. A potential solution to this problem is the development of sensitive microelectrodes that could fulfill this task [161]. Therefore, it is necessary to develop miniaturized electrode materials with very high affinity for the sensory molecule, i.e., high sensitivity and selectivity, low detection limit, and resistance to biofilm deposition. Promising materials for producing sensitive microelectrodes include polymers such as polydopamine (PDA) and polyzwitterions (PZ). Dopamine can be polymerized on various surfaces using oxidative polymerization or electropolymerization [162, 163]. Polyzwitterions are well known for their antifouling properties [164, 165], i.e., their ability to resist adsorption of various biomolecules and prevent biofilm formation on the surface.

The objective of the study [159] was to demonstrate that hybrid PDA/PZ coatings improve the sensory properties of electrodes for use in sensors for detecting dopamine in neutral environments and bovine serum solutions. The synthesis of hybrid PDA/PZ thin films via electropolymerization was proposed for the first time in the described study. The synthesis method involved the incorporation of sulfobetaine methacrylate (SBMA) into the PDA matrix in a one-step electropolymerization process. The substrate for the PDA/PZ electrode was boron-doped carbon nanowalls (BCNW), deposited on silicon using chemical vapor deposition (CVD). The structural features of regular BCNW and modified BCNW/PDA/PZ electrodes were studied using scanning electron microscopy (SEM), Fourier-transform infrared spectroscopy (FT-IR), X-ray photoelectron spectroscopy (XPS), as well as nanoindentation tests. Fig. 6.32 shows SEM images of the tested composites.

The thickness of the PDA/PZ coating, as estimated by atomic force microscopy (AFM), was 51 nm, while the thickness of the PDA coating was only 6 nm. However, the latter value falls within the experimental error range and is therefore approximate. To better understand the relationship between the chemical and surface properties of functionalized BCNW, nanoindentation tests were conducted in static, scratch, and impact modes. The load-displacement curves showed that the carbon nanowalls (BCNW) had the lowest stiffness and hardness, which increased after the electropolymerization of PDA and PZ (Table 6.4, Fig. 6.33). PDA increased the stiffness of the carbon nanowalls by approximately 2-fold, and the hybrid PDA/PZ coating could increase this stiffness by as much as 7.3-fold. Furthermore, the slope of the time-deformation (creep) curves was the lowest for BCNW/PDA/PZ among the tested

materials, indicating that the BCNW/PDA/PZ composites had the highest creep resistance (Fig. 6.34). Finally, the final penetration depth, h_r, in this experiment was 376 nm for BCNW/PDA/PZ compared to 698 nm for BCNW alone, and the plastic deformation work, W_{pl}, during indentation was the lowest for the hybrid composite. These observations clearly suggest that the hybrid coating has more cross-linking than the PDA coating. These cross-links are likely caused by electrostatic interactions between the amphiphilic PZ molecules and π-cation interactions. This is consistent with the predicted phenomenon of zwitterionic monomers being incorporated into the coating during the electropolymerization process.

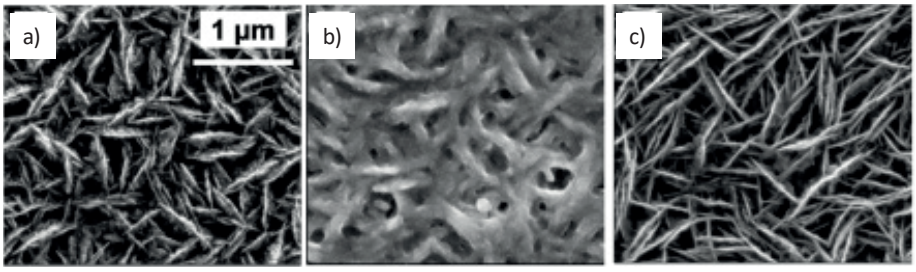

Fig. 6.32. Microstructure of boron-doped carbon nanowalls (BCNW) deposited on a Si substrate (a), polydopamine deposited on BCNW (PD/BCNW) (b), and polyzwitterion deposited on PD/BCNW (PZ/PD/BCNW) (c)

Source: reproduced with permission from [159].

Table. 6.4

Nanomechanical properties calculated based on the load-displacement curves shown in Fig. 6.32

	BCNW	BCNW/PDA	BCNW/PDA/PZ
stiffness E [GPa]	6.89	12.48	50.28
hardness H [GPa]	0.67	0.79	1.48
depth h_e [nm]	178	106	35
depth h_r [nm]	520	475	341
work W_{el} [nJ]	0.74	0.45	0.18
work W_{pl} [nJ]	0.95	0.93	0.46

Source: own work based on [159].

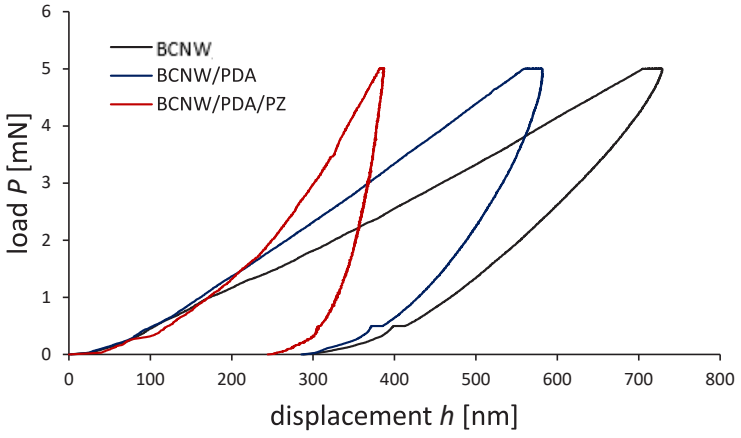

Fig. 6.33. $P = f(h)$ curves of the tested coatings

Source: own work based on [159].

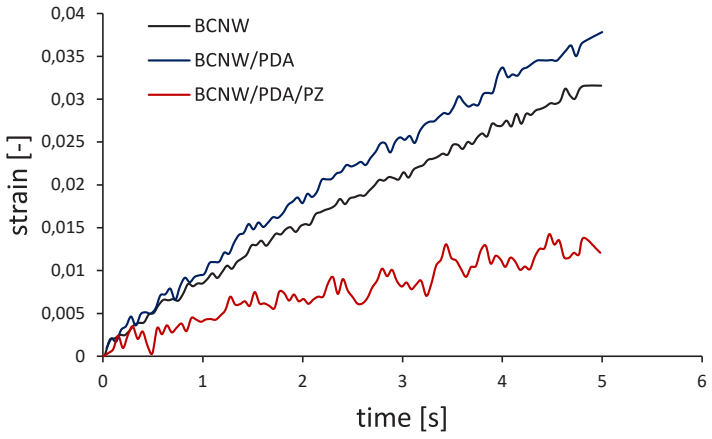

Fig. 6.34. Creep curves of the coatings under a 5 mN load

Source: own work based on [159].

The effect of increased hardness is also evident in the scratch tests (Fig. 6.35). For the BCNW coating, the indenter load of 100 mN is reached at a depth of approximately 1.35 µm, whereas for the BCNW/PDA/PZ coating, it is only 0.85 µm. Additionally, the friction force of the modified BCNW increases more rapidly with depth and reaches about 130 mN, nearly twice as high compared to the BCNW coating. These observations suggest that the PDA/PZ modification strengthens the BCNW structure and enhances its scratch resistance. This feature is advantageous for biosensors operating in liquid flow conditions, where abrasion and wear caused by fluid friction may lead to damage over time.

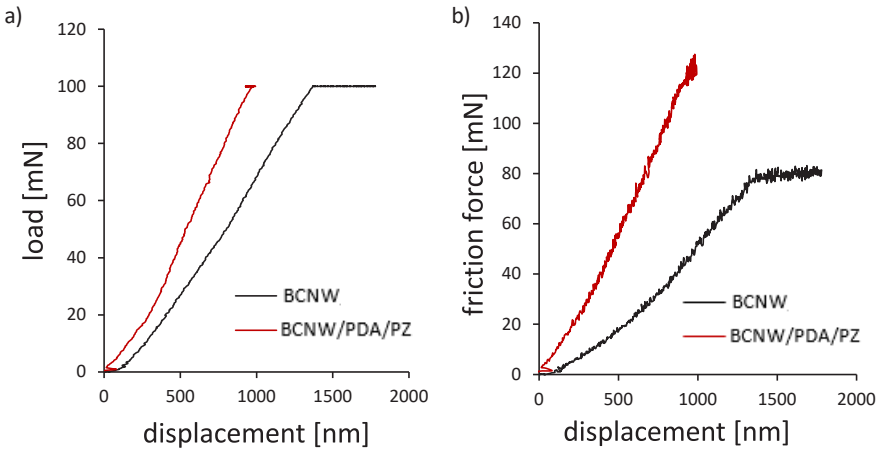

Fig. 6.35. Changes in normal force (a) and friction force (b) during the scratch test

Source: own work based on [159].

Impact tests involved striking the indenter on the tested coating and maintaining a 5 mN force for 5 seconds, after which the load was immediately removed. After 2 seconds, the cycle was repeated. A total of 10 cycles were performed (Fig. 6.36). The tests revealed several important correlations between the mechanical properties and the structure of the functionalized BCNW electrodes. The BCNW coating exhibited swelling after each impact, as shown in Fig. 6.37, with a large deformation plateau accompanied by smaller oscillations around the plateau. Additionally, the plateau value decreases after the fifth impact, and the deformation rate drops almost to zero, suggesting permanent deformation of the carbon nanowalls. However, by the tenth impact, the plateau rises again, and the deformation rate is slightly above zero, which may be associated with stress relaxation through a cracking mechanism.

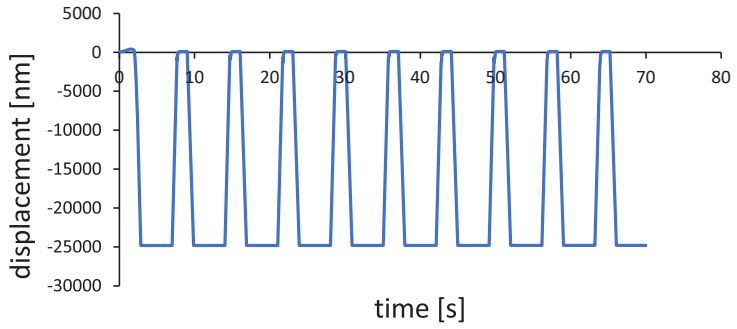

Fig. 6.36. Impact load cycles for the tested coatings

Source: own work based on [159].

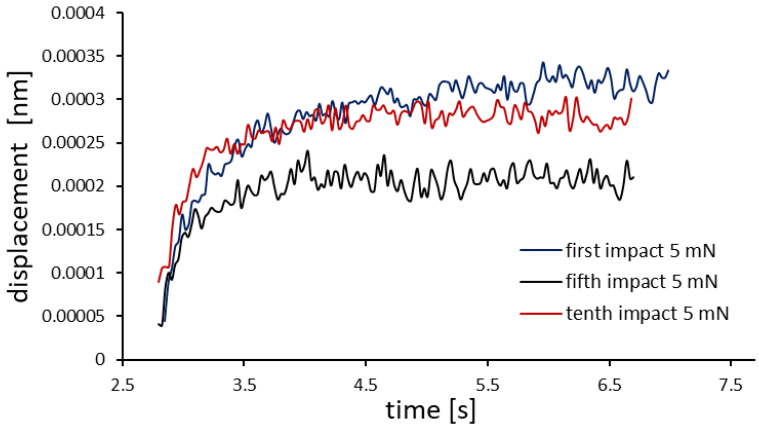

Fig. 6.37. Changes in indenter displacement after impact loading during successive strikes on the BCNW coating

Source: own work based on [159].

A different response to the impact (Fig. 6.38) was observed for the functionalized BCNW (only BCNW/PDA/PZ is shown in the figure, but the response for BCNW/PDA is identical). Instead of swelling, there are oscillations around the zero-deformation axis, regardless of the number of impacts. The interpretation of this behavior is that after coating the BCNW, the internal spaces between the walls are reduced or eliminated, leaving no room for the carbon nanowalls to swell. In other words, the carbon nanowalls are forced to oscillate around their equilibrium because the coating has altered their geometry, preventing swelling. This observation provides further evidence that PDA and PZ significantly alter the surface properties of BCNW, as also reflected in the electrochemical test results.

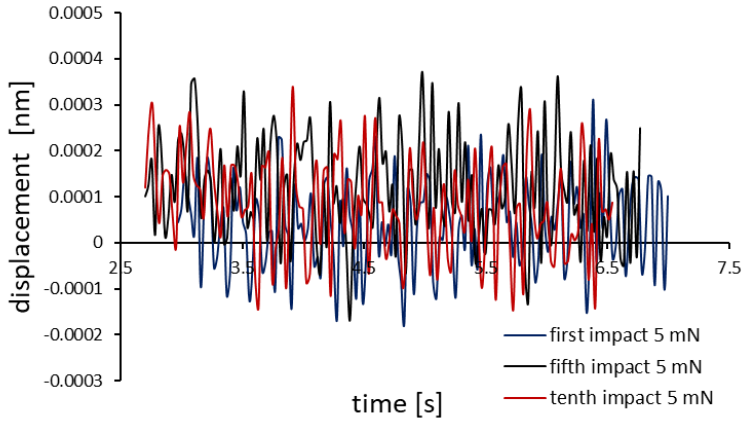

Fig. 6.38. Changes in indenter displacement after impact loading during successive strikes on the BCNW/PDA/PZ composite

Source: own work based on [159].

The results of the presented studies indicate that the nanoindentation test and the scratch test can also be successfully used in characterizing newly developed carbon-based materials, such as carbon nanowalls and carbon-polymer

composites, intended for medical sensor applications. The research presented in the study [159] demonstrated that zwitterions can be incorporated into the PDA structure through co-electropolymerization with dopamine on the surface of BCNW. FTIR and XPS studies suggest that this process most likely occurs through non-covalent electrostatic and π-cation interactions, leading to a higher density of cross-linking bonds compared to pure polydopamine. Nanoindentation studies, in turn, indicate that the hybrid coating exhibits increased stiffness, hardness, and scratch resistance of BCNW, reflecting the higher density of cross-linking bonds. In summary, the use of contact mechanics in characterizing newly developed composite materials has complemented other research methods and expanded research capabilities.

6.6. Characterization of Laser-Modified Polydopamine Deposited on TiO_2 Nanotubes

Polydopamine (PDA) and melanin-based materials represent a vast research topic in the fields of materials engineering, electrochemistry, photochemistry, and electronics, with many promising applications in each of these areas [166-168]. Despite the rich chemistry of PDA [169-171], associated with amine-catechol-quinone interactions and the potential for creating various physical structures, including π-π stacking, π-cation, or aryl-aryl linkages, there are many procedures for modifying its structure at various levels. These procedures can include monomer modification at the synthesis level [172-174], direct modification of functional groups [175], or the incorporation of other chemical entities into the PDA matrix, such as transition metals [176, 177] or organic molecules [159, 163, 178], during oxidative or electropolymerization processes.

The proposed modifications aim to expand the application of PDA across a wide range of areas, including supercapacitors [179], protection from photocorrosion [180], fluorescence generation [181], flexible electronics, and biomedicine, including biosensing [182]. However, one of the most serious issues limiting its applications is PDA's poor mechanical properties, which are related to high surface roughness and agglomeration. This issue is particularly critical in electrochemical applications and colorimetric sensing [183].

A proposed improvement in this area was laser modification of PDA, which resulted in partial graphitization of the polymer with covalent bonding between PDA units [184]. This modification led to a hundredfold increase in scratch resistance, surpassing the values achieved by quartz and TiO_2 under the applied scratching parameters. Initially, the rough layer with high surface roughness was transformed into a uniform 37 nm film without agglomerated PDA nanoparticles. More importantly, the most desirable properties of PDA, such as high adhesiveness and biofouling resistance related to the catechol functionality, were preserved.

Laser-graphitized PDA (lgPDA) can be considered part of the class of LIG (laser-induced graphene/graphite) materials, which are particularly promising for electronic and electrochemical applications [185-187]. The goal of LIG-ation is to transform a poorly conductive organic polymer into a highly conductive carbon-based layer, typically nitrogen-doped. From an electrochemical perspective, such treatment facilitates charge transfer at the electrode-electrolyte interface.

In the study [188], electropolymerized PDA was modified using a pulsed Nd:YAG laser with wavelengths of 365 nm and 532 nm and varying pulse parameters. Titanium dioxide (TiO_2) nanotubes were selected as the substrate for PDA deposition (prior to laser graphitization) for several reasons. First, TiO_2 is a well-studied semiconductor with a high bandgap, prone to photosensitization by dyes or PDA. Second, nanotubes exhibit nanomicroporous morphology, resulting in high PDA loading. Therefore, it serves as a reasonable platform for studying PDA-semiconductor interactions. Partial graphitization was confirmed using several techniques, including XPS, Raman scattering, nanoindentation, contact angle measurements, and electrochemical studies. Graphitization was modeled at the molecular level using a reactive molecular dynamics approach. Wavelength-resolved photoelectrochemistry and quantum efficiency measurements were performed to elucidate the mechanism of enhanced absorption and photocurrent generation in the visible range.

The nanoindentation test was performed on the surface of TiO_2 nanotubes (TNT) as well as nanotubes with dopamine deposited on them (TNT_PDA) and laser-modified dopamine (TNT_IgPDA). The tests were conducted using a Berkovich indenter with a maximum load of 0.4 mN. The loading rate of the indenter was 0.1 mN/s. Once the maximum load was reached, it was maintained for 5 seconds, and then the load was reduced at a rate of 0.1 mN/s. Measurements were taken at the same location, and the described cycle was repeated 10 times. After each cycle, the hardness and stiffness of the surface were determined using the Oliver-Pharr method.

The elastic properties of the surface were also characterized by the elastic work during the unloading of the indenter. This work was calculated as the area under the unloading curve, i.e., the curve P = f(h), where P is the indenter load and h is its displacement in the tested material. Hardness, stiffness, and elastic work were all calculated using NanoTest Ventage nanoindenter software.

In each load cycle, the creep rate of the nanotubes at a constant maximum load was also determined. The creep rate was calculated based on the curve $\Delta h/h = \varepsilon = f(t)$, where Δh is the penetration depth increment of the indenter at a constant maximum load, and t is the time at the constant maximum load. The creep rate $d\varepsilon/dt$ was determined in the steady state, where $\Delta h/h$ was a linear function of time t.

Considering that graphitization significantly alters the mechanical properties of PDA, a series of repetitive nanoindentation experiments were conducted to verify whether the PDA deposited on the surface of TiO_2 nanotubes exhibits the same behavior (Figures 6.39-6.42). It is easy to observe that the hardness of the TNT_lgPDA heterostructure is the highest among the studied samples, and its decay with consecutive loading is slower compared to the pristine nanotubes. Elastic work during indentation is markedly higher for both pristine and laser-treated PDA, indicating that more energy is required for deformation to occur. A similar trend was observed for stiffness (Young's modulus). Finally, the creep rate (i.e., the slope of deformation with respect to time during indentation) decreased after modification with either PDA or lgPDA. In summary, the phenomenon of increased hardness after laser modification was confirmed in the case of PDA deposited on the surface of TiO_2 nanotubes. However, its influence on other mechanical properties appears to be negligible in the studied system. Presumably, the PDA itself causes the major changes in the mechanical properties of the TNT electrode compared to the subsequent laser treatment.

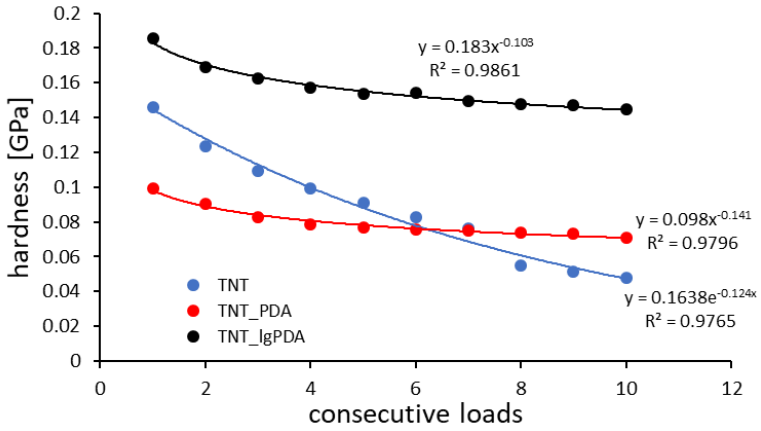

Fig. 6.39. Changes in the hardness of TiO_2 nanotubes (TNT), TiO_2 nanotubes with deposited polydopamine (TNT_PDA), and laser-modified polydopamine deposited on TiO_2 nanotubes (TNT_lgPDA) during successive indentation cycles

Source: own work based on [188].

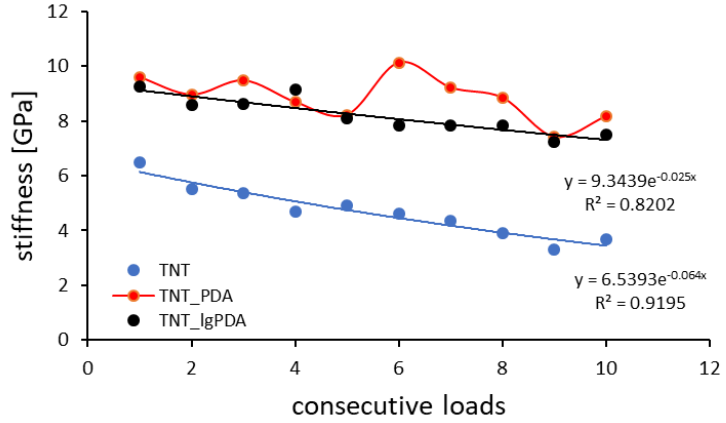

Fig. 6.40. Changes in the stiffness of TiO_2 nanotubes (TNT), TiO_2 nanotubes with deposited polydopamine (TNT_PDA), and laser-modified polydopamine deposited on TiO_2 nanotubes (TNT_lgPDA) during successive indentation cycles

Source: own work based on [188].

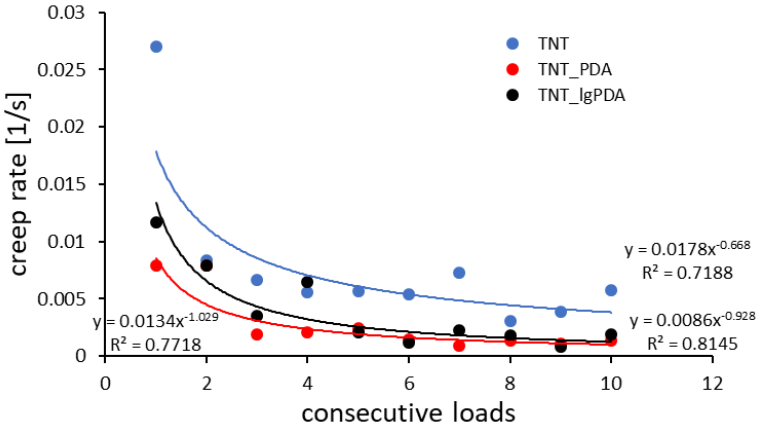

Fig. 6.41. Changes in the creep rate of TiO_2 nanotubes (TNT), TiO_2 nanotubes with deposited polydopamine (TNT_PDA), and laser-modified polydopamine deposited on TiO_2 nanotubes (TNT_lgPDA) during successive indentation cycles

Source: own work based on [188].

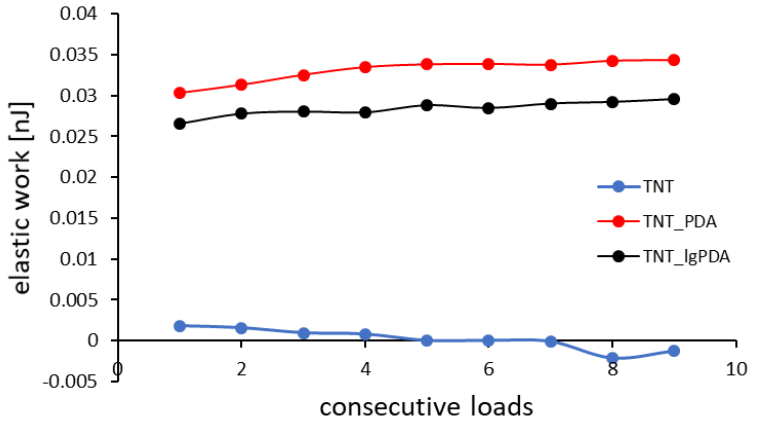

Fig. 6.42. Changes in elastic work of TiO_2 nanotubes (TNT), TiO_2 nanotubes with deposited polydopamine (TNT_PDA), and laser-modified polydopamine deposited on TiO_2 nanotubes (TNT_lgPDA) during successive indentation cycles

Source: own work based on [188].

As the presented results indicate, the nanoindentation test can successfully be used to characterize the properties of laser-modified polydopamine deposited on TiO_2 nanotubes. This method allowed for the evaluation of changes in hardness, stiffness, creep rate, and elastic properties of laser-modified polydopamine deposited on TiO_2 nanotubes, depending on successive loading and unloading cycles of the indenter. Additionally, it enabled comparison of these changes with those observed in polydopamine before laser modification and with the properties of the substrate itself, namely TiO_2 nanotubes. Thus, it is a valuable research tool that can be used to determine the properties of newly designed materials and can effectively complement other research methods used in Materials Engineering.

7. Conclusion

The theoretical foundations describing the behavior of a material in the range of its elastic deformation during indentation by a spherical indenter were first described by Hertz. In later years, many methods of measuring material hardness utilizing contact mechanics were developed. The earliest methods for measuring material hardness used concentrated forces applied to indenters of various shapes, and the resistance of the material being tested was measured. This resistance was termed the hardness of the material. However, each of the proposed methods defined hardness differently, making the methods incomparable. Although conversion tables were developed to translate hardness values from one scale to another, the physical meaning of hardness remained different. For example, Brinell proposed defining material hardness as the ratio of the applied force on a spherical indenter to the area of the spherical impression left in the material after unloading. Meyer, on the other hand, suggested determining hardness as the ratio of the applied force to the projected area of the spherical cap of the impression on the material surface after unloading.

Later, other indenter shapes were proposed. For example, Smith and Sandland introduced the Vickers method, which utilized a square-based pyramid indenter with a 136° apex angle to eliminate difficulties in measuring the impression left by a spherical indenter. Similar to Brinell, they suggested calculating hardness based on the surface area of the impression after unloading, derived from the indenter's geometry. However, this approach did not account for the fact that the shape of the plastically deformed material after unloading was no longer the same as the indenter's shape due to the elastic deformation of the material's volume during unloading. Knoop introduced an indenter shaped like a rhombic-based pyramid, where the ratio of the longer to shorter diagonal was 7:1, with vertex angles of 172° for the long edge and 130° for the short edge. This shape allowed for a more precise measurement of the longer diagonal and, thus, a more accurate hardness measurement.

Similarly, in the Vickers method, the impression area was calculated based on the indenter's shape. However, Knoop was the first to observe phenomena like "pile-up" and "sink-in" effects in some materials, while others exhibited neither. The Rockwell brothers proposed another method, where hardness was determined based on the depth the indenter penetrated under a constant load, measured after unloading. Depending on the material, different indenters were used, such as a 120° diamond cone or steel balls of varying diameters, with loads ranging from 15 kgf to 150 kgf. The main advantage of the Rockwell hardness tester was the ability to display the hardness value directly, avoiding the tedious calculations required by other hardness testing methods.

In the 1970s, Martens proposed measuring hardness using a sharp indenter, such as the one used in the Vickers method. Hardness in this method was determined by dividing the maximum load applied to the indenter by the lateral surface area of the indenter, corresponding to the depth to which it penetrated at maximum load. Unlike the Vickers method, hardness here depended on both the elastic and plastic deformation of the material at maximum load. Finally, in the 1980s, the indentation method was introduced, allowing not only for hardness measurements but also for determining stiffness and other mechanical properties, as described in this monograph.

The development of this method was made possible by theoretical research by Sneddon in the 1940s and 1950s. Similar to the Martens method, the indentation technique involves continuous measurement of the force applied to and removed from the indenter, along with the corresponding indenter displacement. Various indenter loads and shapes can be used, with sharp indenters replaced by conical ones when needed. This approach allowed the application of Sneddon's equations for determining hardness and stiffness for different sharp indenter shapes. The most common indenter shape in this method is the one proposed by Berkovich, due to its ease of manufacture. Indenter loads can range from nN to pN, allowing for the determination of hardness in thin coatings or small phase precipitates. On the other hand, loads up to tens of newtons enable macroscopic property measurements.

This method can be used to characterize all types of engineering materials, and thanks to theoretical advancements, it can also model mechanical properties. Modern indenters allow for other types of material testing, such as scratch tests, dynamic load tests, or wear resistance testing on micro-scale surfaces. Another valuable feature of indentation tests is the ability to map larger areas to determine the distribution of mechanical properties across a material's surface.

This monograph has allowed for the systematization and deepening of knowledge about contact mechanics-based research techniques. The research findings using the indentation system show that the objectives of this study have been achieved. It has been demonstrated that contact mechanics, particularly the nanoindentation test, is a useful method for characterizing both newly developed materials and those processed in new and different ways. Using this research tool, it is possible to characterize laser-modified polydopamine deposited on TiO_2 nanotubes, as well as composites consisting of carbon nanowalls, polydopamine, and polyzwitterion. Additionally, it can be applied to classic materials like C45 steel, ground in such a way as to enhance the surface layer's mechanical properties through strain hardening, or laser-treated 30HGSNA steel used in aircraft landing gear components. It has also been shown that this technique can be used to characterize materials produced with new technologies such as Micro Arc Oxidation or bacterial cellulose.

References

[1] Hertz H. Ueber die Berührung fester elastischer Körper. Journal für die reine und angewandte Mathematik 1882; 92: 156–171.
[2] Hertz H. On hardness, Verh. Ver. Beförderung Gewerbe Fleisses 1882; 61: 410.
[3] Sneddon I.N. Note on a boundary value problem of Reissner and Sagoci. Journal of Applied Physics 1947; 18(1): 130–132.
[4] Sneddon I.N. Boussinesq's problem for a rigid cone. Mathematical Proceedings of the Cambridge Philosophical Society. Cambridge University Press, Cambridge 1948: 492–507.
[5] Johnson K.L., Kendall K., Roberts A.D., Tabor D. Surface energy and the contact of elastic solids. Proceedings of the Royal Society of London. A. Mathematical and Physical Sciences 1971; 324(1558): 301–313.
[6] Derjaguin B.V., Muller V.M., Toporov Y.P. Effect of contact deformations on the adhesion of particles. Journal of Colloid and Interface Science 1975; 53(2): 314–326.
[7] Muller V.M., Derjaguin B.V., Toporov Y.P. On two methods of calculation of the force of sticking of an elastic sphere to a rigid plane. Colloids and Surfaces 1983; 7(3): 251–259.
[8] Tabor D. Surface forces and surface interactions. Journal of Colloid and Interface Science 1977; 58(1): 2–13.
[9] Muller V.M., Yushchenko V.S., Derjaguin B.V. On the influence of molecular forces on the deformation of an elastic sphere and its sticking to a rigid plane. Journal of Colloid and Interface Science 1980; 77(1): 91–101.
[10] Greenwood J.A. Adhesion of elastic spheres. Proceedings of the Royal Society of London. Series A: Mathematical, Physical and Engineering Sciences 1997; 453(1961): 1277–1297.
[11] Feng J. Contact behavior of spherical elastic particles: a computational study of particle adhesion and deformations. Colloids and Surfaces A: Physicochemical and Engineering Aspects 2000; 172: 175–198.
[12] Maugis D. Adhesion of spheres: the JKR-DMT transition using a dugdale model. Journal of Colloid and Interface Science 1992; 150(1): 243–269.
[13] Dugdale D.S. Yielding of steel sheets containing slits. Journal of the Mechanics and Physics of Solids 1960; 8(2): 100–104.
[14] Lennard-Jones J.E. Cohesion. Proceedings of the Physical Society 1931; 43(5): 461.
[15] Johnson K.L., Greenwood J.A. An adhesion map for the contact of elastic spheres. Journal of Colloid and Interface Science 1997; 192(2): 326–333.
[16] Zheng Z., Yu J. Using the Dugdale approximation to match a specific interaction in the adhesive contact of elastic objects. Journal of Colloid and Interface Science 2007; 310(1): 27–34.
[17] Hanaor D.A.H., Gan Y., Einav I. Static friction at fractal interfaces. Tribology International 2016; 93: 229–238.
[18] Hyun S., Robbins M. Elastic contact between rough surfaces: effect of roughness at large and small wavelengths. Tribology International 2007; 40: 1413–1422.
[19] Greenwood J., Williamson J. Contact of nominally flat surfaces. Proceedings of the Royal Society of London (A) 1966; 295: 300–319.
[20] Johnson K.L. Contact mechanics. Cambridge University Press, Cambridge 1985.
[21] Mikić B.B. Thermal contact conductance; theoretical considerations. International Journal of Heat and Mass Transfer 1974; 17(2): 205–214.
[22] Leighton M., Rahmani R., Rahnejat H. Surface-specific flow factors for prediction of friction of cross-hatched surfaces, Surface Topography: Metrology and Properties 2016; 4: 025002.
[23] Jedynak R. Exact and approximate solutions of the infinite integrals of the asperity height distribution for the Greenwood–Williamson and the Greenwood–Tripp asperity contact models. Tribology International 2019; 130: 206–215.

[24] Peklenik J. Paper 24: new developments in surface characterization and measurements by means of random process analysis. Proceedings of the Institution of Mechanical Engineers, Conference Proceedings 1967; 182(11): 108–126.
[25] Leighton M., Morris N., Gore M., Rahmani R., Rahnejat H., King P.D. Boundary interactions of rough non-Gaussian surfaces. Proceedings of the Institution of Mechanical Engineers, Part J: Journal of Engineering Tribology 2016; 230(11): 1359–1370.
[26] Leighton M., Morris N., Rahmani R., Rahnejat H. Surface specific asperity model for prediction of friction in boundary and mixed regimes of lubrication. Meccanica 2017; 52(1): 21–33.
[27] Greenwood J.A., Tripp J.H. The contact of two nominally flat rough surfaces. Proceedings of the Institution of Mechanical Engineers 1970; 185(1): 625–633.
[28] Sneddon I.N. The relation between load and penetration in the axisymmetric boussinesq problem for a punch of arbitrary profile. International Journal of Engineering Science 1965; 3(1): 47–57.
[29] Berkovich E. Three faceted diamond pyramid for micro-hardness testing. Industrial Diamond Review 1951; 11(127): 129.
[30] Meyer E. Untersuchungen über härteprüfung und härte. Julius Springer 1909.
[31] Tabor D. The Hardness of Metals. Oxford University Press Academic, Oxford 2023.
[32] Low S., Germak A., Knott A., Machado R., Song J. Developing definitions of conventional hardness tests for use by National Metrology Institutes. Measurement: Sensors 2021; 18: 1096.
[33] Barbato G., Desogus S. Problems in the measurement of Vickers and Brinell indentations. Measurement 1986; 4(4): 137–147.
[34] Ellis R., Knott A., Herrmann K. Verification of image analysis systems for measuring Brinell indentations. Proceedings of XVIII IMEKO World Congress, Rio de Janeiro, Brazil 2006.
[35] International Bureau of Weights, Measures. Guide to the expression of uncertainty in measurement. DIANE Publishing 1993.
[36] Herrmann K., Polzin T. Neue Richtlinien zur Ermittlung der Unsicherheit von Haertemessungen (New guidelines to the determination of the uncertainty of hardness measurements). Technisches Messen 2005; 72(5): 325–333.
[37] Xintao X., Zhongyu W., Yongsheng G. Estimation of non-statistical uncertainty using fuzzy-set theory. Measurement Science and Technology 2000; 11(4): 430.
[38] Hessling J.P. A novel method of evaluating dynamic measurement uncertainty utilizing digital filters. Measurement Science and Technology 2009; 20(5): 11.
[39] Rebouca P., Cavalcante T., Albuquerque V., Tavares J. Brinell and Vickers hardness measurement using image processing and analysis techniques. Journal of Testing and Evaluation 2010; 38: 88–94.
[40] Leyi G., Wei Z., Jing Z., Songling H. Mechanics analysis and simulation of material Brinell hardness measurement. Measurement 2011; 44(10): 2129–2137.
[41] Smith R.M., Sandland G. An accurate method of determining the hardness of metals, with particular reference to those of a high degree of hardness., Proceedings of the Institution of Mechanical Engineers 1923; 1: 623–641.
[42] Knoop F., Peters C.G., Emerson W.B. A sensitive pyramidal-diamond tool for indentation measurements. Journal of Research of the National Bureau of Standards 1939; 23: 22.
[43] Ben Ghorbal G., Tricoteaux A., Thuault A., Louis G., Chicot D. Comparison of conventional Knoop and Vickers hardness of ceramic materials. Journal of the European Ceramic Society 2017; 37(6): 2531–2535.
[44] Chicot D., Mercier D., Roudet F., Silva K., Staia M.H., Lesage J. Comparison of instrumented Knoop and Vickers hardness measurements on various soft materials and hard ceramics. Journal of the European Ceramic Society 2007; 27(4): 1905–1911.
[45] Gong J., Guan Z. Load dependence of low-load Knoop hardness in ceramics: a modified PSR model. Materials Letters 2001; 47(3): 140–144.
[46] Gong J., Wang J., Guan Z. A comparison between Knoop and Vickers hardness of silicon nitride ceramics. Materials Letters 2002; 56(6): 941–944.
[47] Kehl G.L. The Principles of Metallographic Laboratory Practice, 3rd ed. McGraw-Hill 1949.
[48] Rockwell H.M., Rockwell S.P. "Hardness-Tester", U.S. Patent 1,294,171, 1919.
[49] Chinn R.E. Hardness, bearings, and the rockwells: this is the story of the men behind one of the greatest metallurgical innovations of the 20th Century. Advanced Materials & Processes 2009; 167: 29–31.
[50] Roa S., Sirena M. A finite element analysis of conical indentation in elastic-plastic materials: on strain energy based strategies for an area-independent determination of solids mechanical properties. International Journal of Mechanical Sciences 2021; 207: 106651.
[51] Chen H., Cai L.X., Li C. An elastic-plastic indentation model for different geometric indenters and its applications, Materials Today Communications 2020; 25: 101440.

[52] Li X., Li Z., Ren L.L., Gao S.T., Xu G.F., Tao X.F. Anisotropic distribution of residual strain around conical nanoindentation in silicon. Materials Letters 2014; 137: 389–392.
[53] Bhushan B., Kulkarni A.V., Bonin W., Wyrobek J.T. Nanoindentation and picoindentation measurements using a capacitive transducer system in atomic force microscopy. Philosophical Magazine A: Physics of Condensed Matter, Structure, Defects and Mechanical Properties 1996; 74(5): 1117–1128.
[54] Pethica J. Microhardness tests with penetration depths less than ion implanted layer thickness. [In:] V. Ashworth, W.A. Grant, R.P.M. Procter (eds.). Ion implantation into metals. Pergamon 1982: 147–156.
[55] Fischer-Cripps A.C. The IBIS handbook of nanoindentation. Fischer-Cripps Laboratories, Forestville, NSW 2009.
[56] Fischer-Cripps A.C. Nanoindentation testing. [In:] A.C. Fischer-Cripps (ed.). Nanoindentation. Springer, New York, NY 2011: 21–37.
[57] Menčík J. Uncertainties and errors in nanoindentation. [In:] N. Jiri (ed.). Nanoindentation in Materials Science (chapter 3). IntechOpen, Rijeka 2012.
[58] Richmond O., Morrison H.L., Devenpeck M.L. Sphere indentation with application to the Brinell hardness test. International Journal of Mechanical Sciences 1974; 16(1): 75–82.
[59] Hill R., Storakers B., Zdunek A.B. A theoretical study of the Brinell hardness test. Proceedings of the Royal Society of London Series A 1989; 423: 301–330.
[60] Tirupataiah Y., Sundararajan G. On the constraint factor associated with the indentation of work-hardening materials with a spherical ball. Metallurgical Transactions A 1991; 22(10): 2375–2384.
[61] Taljat B., Zacharia T., Kosel F. New analytical procedure to determine stress-strain curve from spherical indentation data. International Journal of Solids and Structures 1998; 35(33): 4411– 4426.
[62] Beghini M., Bertini L., Fontanari V. Evaluation of the stress–strain curve of metallic materials by spherical indentation. International Journal of Solids and Structures 2006; 43(7): 2441–2459.
[63] Patel D.K., Kalidindi S.R. Correlation of spherical nanoindentation stress-strain curves to simple compression stress-strain curves for elastic-plastic isotropic materials using finite element models. Acta Materialia 2016; 112: 295–302.
[64] Tabor D. A simple theory of static and dynamic hardness. Proceedings of the Royal Society of London. Series A. Mathematical and Physical Sciences 1948; 192(1029): 247–274.
[65] Hertz H. Miscellaneous papers. Macmillan 1896.
[66] Wang Z., Jin X., Keer L.M., Wang Q. Numerical methods for contact between two joined quarter spaces and a rigid sphere. International Journal of Solids and Structures 2012; 49(18): 2515– 2527.
[67] Hernández-Gómez L.H., Pava-Chipol J.F., Trejo-Valdez M., Torres-Torres C., Fernández J.A.B., Urriolagotia-Sosa G., Miguel C.R.T.S., Urriolagotia-Calderón G. Strain measurements exhibited by a steel prosthesis protected with au nanoparticles. [In:] A. Öchsner, H. Altenbach (eds.). Design and computation of modern engineering materials. Springer International Publishing, Cham, New York 2014: 107–120.
[68] Johnson K.L. The correlation of indentation experiments. Journal of the Mechanics and Physics of Solids 1970; 18(2): 115–126.
[69] The mathematical theory of plasticity. R. Hill. The Clarendon Press. Oxford. 1951. 356 pp. 90 figures. 35s. net. The Aeronautical Journal 1951; 55(490): 659–660.
[70] Moharrami N., Bull S.J. A comparison of nanoindentation pile-up in bulk materials and thin films. Thin Solid Films 2014; 572: 189–199.
[71] Oliver W.C., Pharr G.M. An improved technique for determining hardness and elastic modulus using load and displacement sensing indentation experiments. Journal of Materials Research 1992; 7(6): 1564–1583.
[72] Mc Elhaney K.W., Vlassak J.J., Nix W.D. Determination of indenter tip geometry and indentation contact area for depth-sensing indentation experiments. Journal of Materials Research 1998; 13(5): 1300–1306.
[73] Bolshakov A., Pharr G.M. Influences of pileup on the measurement of mechanical properties by load and depth sensing indentation techniques. Journal of Materials Research 1998; 13(4): 1049–1058.
[74] Hay J.L., Olive W.C., Bolshakov A., Pharr G.M. Using the ratio of loading slope and elastic stiffness to predict pile-up and constraint factor during indentation. MRS Online Proceedings Library (OPL) 1998; 522: 101.
[75] Oliver W.C., Pharr G.M. Measurement of hardness and elastic modulus by instrumented indentation: advances in understanding and refinements to methodology. Journal of Materials Research 2004; 19(1): 3–20.
[76] Mesarovic S., Fleck N. Spherical indentation of elastic–plastic solids. Proceedings of The Royal Society A Mathematical Physical and Engineering Sciences 1999; 455: 2707–2728.
[77] Field J.S., Swain M.V. A simple predictive model for spherical indentation. Journal of Materials Research 1993; 8(2): 297–306.

[78] Lim H., Hale L.M., Zimmerman J.A., Battaile C.C., Weinberger C.R. A multi-scale model of dislocation plasticity in α-Fe: incorporating temperature, strain rate and non-Schmid effects. International Journal of Plasticity 2015; 73: 100–118.
[79] Arsenlis A., Parks D.M. Crystallographic aspects of geometrically-necessary and statistically-stored dislocation density. Acta Materialia 1999; 47(5): 1597–1611.
[80] Peierls R. The size of a dislocation. Proceedings of the Physical Society 1940; 52(1): 34.
[81] Qiu X., Huang Y., Nix W.D., Hwang K.C., Gao H. Effect of intrinsic lattice resistance in strain gradient plasticity. Acta Materialia 2001; 49(19): 3949–3958.
[82] Durst K., Backes B., Franke O., Göken M. Indentation size effect in metallic materials: modeling strength from pop-in to macroscopic hardness using geometrically necessary dislocations. Acta Materialia 2006; 54(9): 2547–2555.
[83] Taylor G.I. Plastic strain in metals. Journal of the Institute of Metals 1938; 62: 18.
[84] Lilleodden E.T., Zimmerman J.A., Foiles S.M., Nix W.D. Atomistic simulations of elastic deformation and dislocation nucleation during nanoindentation. Journal of the Mechanics and Physics of Solids 2003; 51(5): 901–920.
[85] Cheng L., Xia X., Yu W., Scriven L.E., Gerberich W.W. Flat-punch indentation of viscoelastic material. Journal of Polymer Science Part B: Polymer Physics 2000; 38(1): 10–22.
[86] Ting T. The contact stresses between a rigid indenter and a viscoelastic half-space. Journal of Applied Mechanics 1966; 33(4): 845–854.
[87] Kutty T.R.G., Ganguly C., Sastry D.H. Development of creep curves from hot indentation hardness data. Scripta Materialia 1996; 34(12): 1833–1838.
[88] Sakai M., Shimizu S. Indentation rheometry for glass-forming materials. Journal of Non- Crystalline Solids 2001; 282(2): 236–247.
[89] Hammer E.W. Symposium on internal stresses in metals and alloys: organized by The Institute of Metals. 485 pages, 14 × 22 cm., drawings, illustrations and tables. London, The Institute of Metals, 1948. Price, 42s, Journal of The Franklin Institute-engineering and Applied Mathematics 1949; 247: 526–527.
[90] Tsui T.Y., Oliver W.C., Pharr G.M. Influences of stress on the measurement of mechanical properties using nanoindentation. Part I. Experimental studies in an aluminum alloy. Journal of Materials Research 1996; 11(3): 752–759.
[91] Kese K.O., Li Z.C., Bergman B. Influence of residual stress on elastic modulus and hardness of soda-lime glass measured by nanoindentation. Journal of Materials Research 2004; 19(10): 3109–3119.
[92] Chou W.J., Yu G.P., Huang J.H. Effect of heat treatment on the structure and properties of ion- plated TiN films. Surface and Coatings Technology 2003; 168(1): 43–50.
[93] Huang J.H., Ma C.H., Chen H. Effect of Ti interlayer on the residual stress and texture development of TiN thin films. Surface and Coatings Technology 2006; 200(20): 5937–5945.
[94] Underwood J.H. Residual-stress measurement using surface displacements around an indentation. Experimental Mechanics 1973; 13(9): 373–380.
[95] Roberts S.G., Lawrence C.W., Bisrat Y., Warren P.D., Hills D.A. Determination of surface residual stresses in brittle materials by Hertzian indentation: theory and experiment. Journal of the American Ceramic Society 1999; 82(7): 1809–1816.
[96] Chaudhri M.M., Phillips M.A. Quasi-static indentation cracking of thermally tempered soda-lime glass with spherical and Vickers indenters. Philosophical Magazine A 1990; 62(1): 1–27.
[97] Lee Y.H., Dongil K. Residual stresses in DLC/Si and Au/Si systems: application of a stress relaxation model to the nanoindentation technique. Journal of Materials Research 2002; 17: 901–906.
[98] Swadener J.G., Taljat B., Pharr G.M. Measurement of residual stress by load and depth sensing indentation with spherical indenters. Journal of Materials Research 2001; 16(7): 2091–2102.
[99] Lawn B.R., Evans A.G., Marshall D.B. Elastic/plastic indentation damage in ceramics: the median/radial crack system. Journal of the American Ceramic Society 1980; 63(9–10): 574–581.
[100] Lawn B. Indentation fracture [In:] B. Lawn. Fracture of brittle solids. Cambridge University Press, Cambridge 1993: 249–306.
[101] Fischer-Cripps A.C. Elastic-plastic indentation stress fields. [In:] F.F. Ling (ed.), Introduction to contact mechanics. Springer US, Boston, MA 2007: 137–150.
[102] Palmqvist S. A method to determine the toughness of brittle materials, especially hard metals. Jernkontorets Annaler 1957; 141: 303–307.
[103] Palmqvist S. Occurrence of crack formation during Vickers indentation as a measure of the toughness of hard materials. Archiv für das Eisenhüttenwesen 1962; 33(9): 629–634.
[104] Feng Y., Zhang T. Determination of fracture toughness of brittle materials by indentation, Acta Mechanica Solida Sinica 2015; 28(3): 221–234.

[105] Laugier M.T. Palmqvist indentation toughness in WC-Co composites. Journal of Materials Science Letters 1987; 6(8): 897–900.
[106] Ouchterlony F. Stress intensity factors for the expansion loaded star crack. Engineering Fracture Mechanics 1976; 8(2): 447–448.
[107] Dukino R., Swain M. Comparative measurement of fracture toughness with Berkovich and Vickers indenters. Journal of the American Ceramic Society 2005; 75: 3299–3304.
[108] Field J.S., Swain M.V., Dukino R.D. Determination of fracture toughness from the extra penetration produced by indentation-induced pop-in. Journal of Materials Research 2003; 18(6): 1412–1419.
[109] Loubet J., Lucas B., Oliver W. [In:] D.T. Smith (ed.).NIST Special Publication 896. Conference Proceedings: International Workshop on Instrumented Indentation 1995: 31–34.
[110] Bower A.F., Fleck N.A., Needleman A., Ogbonna N., Enderby J.E. Indentation of a power law creeping solid. Proceedings of the Royal Society of London. Series A: Mathematical and Physical Sciences 1997; 441(1911): 97–124.
[111] Sekler J., Steinmann P.A., Hintermann H.E. The scratch test: different critical load determination techniques. Surface and Coatings Technology 1988; 36(1): 519–529.
[112] Randall N.X. The current state-of-the-art in scratch testing of coated systems. Surface and Coatings Technology 2019; 380: 125092.
[113] Klemm D., Kramer F., Moritz S., Lindström T., Ankerfors M., Gray D., Dorris A. Nanocelluloses: a new family of nature-based materials. Angewandte Chemie International Edition 2011; 50(24): 5438–5466.
[114] Brown R.M.J. Bacterial cellulose. Ellis Horwood, Chichester, UK 1989.
[115] Gatenholm P., Klemm D. Bacterial nanocellulose as a renewable material for biomedical applications. MRS Bulletin 2010; 35: 208–213.
[116] Pang M., Huang Y., Meng F., Zhuang Y., Liu H., Du M., Ma Q., Wang Q., Chen Z., Chen L., Cai T., Cai Y. Application of bacterial cellulose in skin and bone tissue engineering. European Polymer Journal 2020; 122: 109365.
[117] Beaumont M., König J., Opietnik M., Potthast A., Rosenau T. Drying of a cellulose II gel: effect of physical modification and redispersibility in water. Cellulose 2017; 24: 1199–1209.
[118] Stanisławska A., Staroszczyk H., Szkodo M. The effect of dehydration/rehydration of bacterial nanocellulose on its tensile strength and physicochemical properties. Carbohydrate Polymers 2020; 236: 116023.
[119] Stanisławska A. Biomaterials and implants in cardiac and vascular surgery – review. Advances in Materials Science 2014; 14(3): 5–17.
[120] A. Stanisławska, M. Szkodo, H. Staroszczyk, K. Dawidowska, M. Kołaczkowska, P. Siondalski, Effect of the ex situ physical and in situ chemical modification of bacterial nanocellulose on mechanical properties in the context of its potential applications in heart valve design, International Journal of Biological Macromolecules 269 (2024) 131951.
[121] Bardin J.A., Eisen E.A., Tolbert P.E., Hallock M.F., Hammond S.K., Woskie S.R., Smith T.J., Monson R.R. Mortality studies of machining fluid exposure in the automobile industry V: a case-control study of pancreatic cancer. American Journal of Industrial Medicine 1997; 32(3): 240–247.
[122] Alonso U., Ortega N., Sanchez J.A., Pombo I., Izquierdo B., Plaza S. Hardness control of grind- hardening and finishing grinding by means of area-based specific energy. International Journal of Machine Tools and Manufacture 2015; 88: 24–33.
[123] Uhlmann E., Lypovka P., Hochschild L., Schröer N. Influence of rail grinding process parameters on rail surface roughness and surface layer hardness. Wear 2016; 366–367: 287–293.
[124] Heinzel C., Bleil N. The use of the size effect in grinding for work-hardening. CIRP Annals 2007; 56(1): 327–330.
[125] Szkodo M., Chodnicka-Wszelak K., Deja M., Stanisławska A., Bartmański M. The Influence of the depth of cut in single-pass grinding on the microstructure and properties of the C45 steel surface layer. Materials 2020; 13(5): 1040.
[126] Á. Révész, T. Ungár, A. Borbély, J. Lendvai, Dislocations and grain size in ball-milled iron powder, Nanostructured Materials 7(7) (1996) 779-788.
[127] F. HajyAkbary, J. Sietsma, A.J. Böttger, M.J. Santofimia, An improved X-ray diffraction analysis method to characterize dislocation density in lath martensitic structures, Materials Science and Engineering: A 639 (2015) 208-218.
[128] Z. Cong, Y. Murata, Dislocation Density of Lath Martensite in 10Cr-5W Heat-Resistant Steels, Materials Transactions 52(12) (2011) 2151-2154.
[129] H. Matsui, H. Kimura, A mechanism of the "unexpected {110} slip" observed in BCC metals deformed at low temperatures, Scripta Metallurgica 7(9) (1973) 905-913.
[130] V. Vitek †, Core structure of screw dislocations in body-centred cubic metals: relation to symmetry and interatomic bonding, Philosophical Magazine 84(3-5) (2004) 415-428.

[131] Szkodo M., Bień A., Stanisławska A. Laser beam as a precision tool to increase fatigue resistance in an eyelet of undercarriage drag strut. International Journal of Precision Engineering and Manufacturing-Green Technology 2022; 9(1): 175–190.
[132] Woo W.S., Lee C.M. A study on the optimum machining conditions and energy efficiency of a laser-assisted fillet milling. International Journal of Precision Engineering and Manufacturing- Green Technology 2018; 5(5): 593–604.
[133] Lee C.M., Woo W.S., Baek J.T., Kim E.J. Laser and arc manufacturing processes: a review. International Journal of Precision Engineering and Manufacturing 2016; 17(7): 973–985.
[134] Černý I., Sís J., Fatigue strength of laser hardened 42CrMo4 steel considering effects of compressive residual stresses on short crack growth. Procedia Engineering 2014; 74: 417–420.
[135] Božić Ž., Schmauder S., Wolf H. The effect of residual stresses on fatigue crack propagation in welded stiffened panels. Engineering Failure Analysis 2018; 84: 346–357.
[136] McDaniels R.L., White S.A., Liaw K., Chen L., McCay M.H., Liaw P.K. Effects of a laser surface processing induced heat-affected zone on the fatigue behavior of AISI 4340 steel. Materials Science and Engineering: A 2008; 485(1): 500–507.
[137] De la Cruz P., Odén M., Ericsson T. Effect of laser hardening on the fatigue strength and fracture of a B–Mn steel. International Journal of Fatigue 1998; 20(5): 389–398.
[138] Szkodo M., Stanisławska A., Komarov A., Bolewski Ł. Effect of MAO coatings on cavitation erosion and tribological properties of 5056 and 7075 aluminum alloys. Wear 2021; 474–475:
[139] Deng Y., Ye R., Xu G., Yang J., Pan Q., Peng B., Cao X., Duan Y., Wang Y., Lu L., Yin Z. Corrosion behaviour and mechanism of new aerospace Al–Zn–Mg alloy friction stir welded joints and the effects of secondary Al3ScxZr1–x nanoparticles. Corrosion Science 2015; 90: 359–374.
[140] Deng Y., Peng B., Xu G., Pan Q., Yin Z., Ye R., Wang Y., Lu L. Effects of Sc and Zr on mechanical property and microstructure of tungsten inert gas and friction stir welded aerospace high strength Al–Zn–Mg alloys. Materials Science and Engineering: A 2015; 639: 500–513.
[141] Goebel J., Ghidini T., Graham A.J. Stress-corrosion cracking characterisation of the advanced aerospace Al–Li 2099-T86 alloy. Materials Science and Engineering: A 2016; 673: 16–23.
[142] Xu L., Yu X., Hui L., Zhou S. Fatigue life prediction of aviation aluminium alloy based on quantitative pre-corrosion damage analysis. Transactions of Nonferrous Metals Society of China 2017; 27(6): 1353–1362.
[143] Magoga T., Aksus S., Cannon S., Ojeda R., Thomas G. Identification of slam events experienced by a high-speed craft. Ocean Engineering 2017; 140: 309–321.
[144] Orłowski M., Bastien C., Razmkhah O., McCartan S. Design methodology for crash occupant protection in cabin design of the high speed vessel. Marine Structures 2017; 51: 1–20.
[145] Boutar Y., Naïmi S., Mezlini S., da Silva L.F.M., Ben Sik Ali M. Characterization of aluminium one-component polyurethane adhesive joints as a function of bond thickness for the automotive industry: fracture analysis and behavior. Engineering Fracture Mechanics 2017; 177: 45–60.
[146] Shin J., Kim T., Kim D., Kim D., Kim K. Castability and mechanical properties of new 7xxx aluminum alloys for automotive chassis/body applications. Journal of Alloys and Compounds 2017; 698: 577–590.
[147] Ram S.C., Chattopadhyay K., Chakrabarty I. High temperature tensile properties of centrifugally cast in-situ Al-Mg-2Si functionally graded composites for automotive cylinder block liners. Journal of Alloys and Compounds 2017; 724: 84–97.
[148] Kamal Jayaraj R., Malarvizhi S., Balasubramanian V. Optimizing the micro-arc oxidation (MAO) parameters to attain coatings with minimum porosity and maximum hardness on the friction stir welded AA6061 aluminium alloy welds. Defence Technology 2017; 13(2): 111–117.
[149] Hou G., An Y., Zhao X., Zhou H., Chen J., Li S., Liu X., Deng W. Improving interfacial, mechanical and tribological properties of alumina coatings on Al alloy by plasma arc heat- treatment of substrate. Applied Surface Science 2017; 411: 53–66.
[150] Wang P., Wu T., Xiao Y.T., Pu J., Guo X.Y. Effects of Ce(SO4)2 concentration on the properties of micro-arc oxidation coatings on ZL108 aluminum alloys. Materials Letters 2016; 182: 27–31.
[151] Wang P., Wu T., Xiao Y.T., Zhang L., Pu J., Cao W.J., Zhong X.M. Characterization of micro- arc oxidation coatings on aluminum drillpipes at different current density. Vacuum 2017; 142: 21–28.
[152] Tran Q.P., Kuo Y.C., Sun J.K., He J.L., Chin T.S. High quality oxide-layers on Al-alloy by micro- arc oxidation using hybrid voltages. Surface and Coatings Technology, Part A 2016; 303: 61–67.
[153] Jafarzadeh K., Valefi Z., Ghavidel B. The effect of plasma spray parameters on the cavitation erosion of Al2O3–TiO_2 coatings. Surface and Coatings Technology 2010; 205(7): 1850–1855.

[154] Zou J., Zhu Y., Pan M., Xie T., Chen X., Yang H. A study on cavitation erosion behavior of AlSi10Mg fabricated by selective laser melting (SLM). Wear 2017; 376–377: 496–506.
[155] Qiao Y., Chen J., Zhou H., Wang Y., Song Q., Li H., Zheng Z. Effect of solution treatment on cavitation erosion behavior of high-nitrogen austenitic stainless steel. Wear 2019; 424–425: 70–77.
[156] Cheng F., Jiang S., Liang J. Cavitation erosion resistance of microarc oxidation coating on aluminium alloy. Applied Surface Science 2013; 280: 287–296.
[157] Dejun K., Hao L., Jinchun W. Effects of micro arc oxidation on fatigue limits and fracture morphologies of 7475 high strength aluminum alloy. Journal of Alloys and Compounds 2015; 650: 393–398.
[158] Bucci R.J., Center A.T., Nordmark G., Starke J.E.A. selecting aluminum alloys to resist failure by fracture mechanisms, ASM handbook. University of Virginia, Department of Materials Science and Engineering, Virginia 1996.
[159] Olejnik A., Ficek M., Szkodo M., Stanisławska A., Karczewski J., Ryl J., Dołęga A., Siuzdak K., Bogdanowicz R. Tailoring diffusional fields in zwitterion/dopamine copolymer electropolymerized at carbon nanowalls for sensitive recognition of neurotransmitters. ACS Nano 2022; 16(8): 13183–13198.
[160] Leopold A.V., Shcherbakova D.M., Verkhusha V.V. Fluorescent biosensors for neurotransmission and neuromodulation: engineering and applications. Frontiers in Cellular Neuroscience 2019; 13: 474.
[161] Shen M., Qu Z., DesLaurier J., Welle T.M., Sweedler J.V., Chen R. Single synaptic observation of cholinergic neurotransmission on living neurons: concentration and dynamics. Journal of the American Chemical Society 2018; 140(25): 7764–7768.
[162] Li S., Wang H., Young M., Xu F., Cheng G., Cong H. Properties of electropolymerized dopamine and its analogues. Langmuir 2019; 35(5): 1119–1125.
[163] Almeida L.C., Frade T., Correia R.D., Niu Y., Jin G., Correia J.P., Viana A.S. Electrosynthesis of polydopamine-ethanolamine films for the development of immunosensing interfaces. Scientific Reports 2021; 11(1): 2237.
[164] Neitzel A.E., De Hoe G.X., Tirrell M.V. Expanding the structural diversity of polyelectrolyte complexes and polyzwitterions. Current Opinion in Solid State and Materials Science 2021; 25(2): 100897.
[165] Laschewsky A., Rosenhahn A. Molecular design of zwitterionic polymer interfaces: searching for the difference. Langmuir 2019; 35(5): 1056–1071.
[166] P. Palladino, F. Bettazzi, S. Scarano, Polydopamine: surface coating, molecular imprinting, and electrochemistry—successful applications and future perspectives in (bio)analysis, Analytical and Bioanalytical Chemistry 411(19) (2019) 4327-4338.
[167] Z. Jin, L. Yang, S. Shi, T. Wang, G. Duan, X. Liu, Y. Li, Flexible Polydopamine Bioelectronics, Advanced Functional Materials 31(30) (2021) 2103391.
[168] N. Bisht, N. Dwivedi, A. Khosla, D.P. Mondal, A.K. Srivastava, C. Dhand, Review—Recent Advances in Polydopamine-based Electrochemical Biosensors, Journal of The Electrochemical Society 169(10) (2022) 107505.
[169] J. Liebscher, R. Mrówczyński, H.A. Scheidt, C. Filip, N.D. Hădade, R. Turcu, A. Bende, S. Beck, Structure of Polydopamine: A Never-Ending Story?, Langmuir 29(33) (2013) 10539-10548.
[170] M.L. Alfieri, L. Panzella, S.L. Oscurato, M. Salvatore, R. Avolio, M.E. Errico, P. Maddalena, A. Napolitano, M. D'Ischia, The Chemistry of Polydopamine Film Formation: The Amine-Quinone Interplay, Biomimetics, 2018.
[171] M. d'Ischia, A. Napolitano, V. Ball, C.-T. Chen, M.J. Buehler, Polydopamine and Eumelanin: From Structure–Property Relationships to a Unified Tailoring Strategy, Accounts of Chemical Research 47(12) (2014) 3541-3550.
[172] S. Li, H. Wang, M. Young, F. Xu, G. Cheng, H. Cong, Properties of Electropolymerized Dopamine and Its Analogues, Langmuir 35(5) (2019) 1119-1125.
[173] T. Marchesi D'Alvise, S. Sunder, R. Hasler, J. Moser, W. Knoll, C.V. Synatschke, S. Harvey, T. Weil, Preparation of Ultrathin and Degradable Polymeric Films by Electropolymerization of 3-Amino-l-tyrosine, Macromolecular Rapid Communications 44(16) (2023) 2200332.
[174] W. Cao, H. Mao, N.C. McCallum, X. Zhou, H. Sun, C. Sharpe, J. Korpanty, Z. Hu, Q.Z. Ni, M.D. Burkart, M.D. Shawkey, M.R. Wasielewski, N.C. Gianneschi, Biomimetic pheomelanin to unravel the electronic, molecular and supramolecular structure of the natural product, Chemical Science 14(15) (2023) 4183-4192.
[175] R. Mrówczyński, R. Markiewicz, J. Liebscher, Chemistry of polydopamine analogues, Polymer International 65(11) (2016) 1288-1299.
[176] Z. Wang, Y. Zou, Y. Li, Y. Cheng, Metal-Containing Polydopamine Nanomaterials: Catalysis, Energy, and Theranostics, Small 16(18) (2020) 1907042.
[177] X. Han, F. Tang, Z. Jin, Free-standing polydopamine films generated in the presence of different metallic ions: the comparison of reaction process and film properties, RSC Advances 8(33) (2018) 18347-18354.
[178] E. Chalmers, H. Lee, C. Zhu, X. Liu, Increasing the Conductivity and Adhesion of Polypyrrole Hydrogels with Electropolymerized Polydopamine, Chemistry of Materials 32(1) (2020) 234-244.

[179] L. Yang, X. Guo, Z. Jin, W. Guo, G. Duan, X. Liu, Y. Li, Emergence of melanin-inspired supercapacitors, Nano Today 37 (2021) 101075.
[180] A. Corani, A. Huijser, T. Gustavsson, D. Markovitsi, P.-Å. Malmqvist, A. Pezzella, M. d'Ischia, V. Sundström, Superior Photoprotective Motifs and Mechanisms in Eumelanins Uncovered, Journal of the American Chemical Society 136(33) (2014) 11626-11635.
[181] P. Yang, S. Zhang, X. Chen, X. Liu, Z. Wang, Y. Li, Recent developments in polydopamine fluorescent nanomaterials, Materials Horizons 7(3) (2020) 746-761.
[182] L.C. Almeida, R.D. Correia, A. Marta, G. Squillaci, A. Morana, F. La Cara, J.P. Correia, A.S. Viana, Electrosynthesis of polydopamine films - tailored matrices for laccase-based biosensors, Applied Surface Science 480 (2019) 979-989.
[183] R. Ren, G. Cai, Z. Yu, Y. Zeng, D. Tang, Metal-Polydopamine Framework: An Innovative Signal-Generation Tag for Colorimetric Immunoassay, Analytical Chemistry 90(18) (2018) 11099-11105.
[184] K. Lee, M. Park, K.G. Malollari, J. Shin, S.M. Winkler, Y. Zheng, J.H. Park, C.P. Grigoropoulos, P.B. Messersmith, Laser-induced graphitization of polydopamine leads to enhanced mechanical performance while preserving multifunctionality, Nature Communications 11(1) (2020) 4848.
[185] T.-S.D. Le, H.-P. Phan, S. Kwon, S. Park, Y. Jung, J. Min, B.J. Chun, H. Yoon, S.H. Ko, S.-W. Kim, Y.-J. Kim, Recent Advances in Laser-Induced Graphene: Mechanism, Fabrication, Properties, and Applications in Flexible Electronics, Advanced Functional Materials 32(48) (2022) 2205158.
[186] H. Wang, Z. Zhao, P. Liu, X. Guo, Laser-Induced Graphene Based Flexible Electronic Devices, Biosensors, 2022.
[187] A.V. Shokurov, C. Menon, Laser-Induced Graphene Electrodes for Electrochemistry Education and Research, Journal of Chemical Education 100(6) (2023) 2411-2417.
[188] A. Olejnik, K. Polaczek, M. Szkodo, A. Stanisławska, J. Ryl, K. Siuzdak, Laser-Induced Graphitization of Polydopamine on Titania Nanotubes, ACS Applied Materials & Interfaces 15(45) (2023) 52921-52938.

Advanced Characterization of Engineering Materials using Indentation Techniques

The first part of the monograph presents the theoretical foundations of contact mechanics. Subsequently, a Hertzian contact model is introduced to describe the relationship between the load applied to a spherical indenter and the resulting displacement. Non-Hertzian models that incorporate adhesion forces are then outlined. Two models accounting for adhesive interactions between a spherical indenter and a substrate are discussed: the Johnson-Kendall-Roberts (JKR) model, which considers the balance between the stored elastic energy and the surface energy loss between the spherical indenter and the flat surface, and the Derjaguin-Muller-Toporov (DMT) model of elastic contact. The JKR model accounts for contact pressure and adhesion forces acting solely within the contact zone, whereas the DMT model also considers attractive forces outside the contact area. The subsequent section presents models for nominally flat surfaces with surface roughness. The Greenwood and Williamson (GW) theory is described, which assumes that surface asperity heights follow a Gaussian distribution and their deformation is governed by Hertzian mechanics, as well as the theory proposed by Greenwood and Tripp. A mathematical description of the deformation behavior of a material in contact with a conical indenter, as developed by Sneddon, is also included. The following chapter reviews various methods for measuring material hardness, including Brinell, Meyer, Vickers, Knoop, Martens, and Rockwell techniques. The indentation method for hardness determination is then addressed. This section includes an analysis of stresses and deformations occurring in the material during penetration by spherical and sharp indenters, the procedures for determining material hardness and stiffness, and a discussion of the size effect observed at small indentation depths. Additionally, methods for determining the dislocation density and mobility in the material are described. Furthermore, the determination of the strain hardening coefficient, the critical stress intensity factor, and residual stresses associated with indentation testing are presented. The chapter also contains information regarding the scratch test method. The final chapter presents the results of scientific studies co-authored by the author, as well as original, unpublished research conducted using indentation techniques.

Zaawansowana charakterystyka materiałów inżynierskich z wykorzystaniem techniki indentacji

W pierwszej części pracy przedstawiono teoretyczne podstawy mechaniki kontaktu. Omówiono model kontaktu Hertza opisujący zależność pomiędzy obciążeniem przyłożonym do kulistego wgłębnika i jego przemieszczeniem. W dalszej części przedstawiono modele niehertzowskie, w których uwzględnia się siły adhezji. Przedstawiono dwa modele uwzględniające adhezyjne przyciąganie sferycznego wgłębnika i podłoża, to jest model Johnson, Kendall i Roberts JKR, wykorzystujący równowagę pomiędzy zmagazynowaną energią sprężystą a utratą energii powierzchniowej pomiędzy kulistym wgłębnikiem i powierzchnią płaską, oraz model sprężystego kontaktu Derjaguin-Muller-Toporov DMT. Model JKR uwzględnia wpływ nacisku kontaktowego i adhezji tylko wewnątrz obszaru kontaktu, natomiast model DMT uwzględnia dodatkowo siły przyciągania występujące pomiędzy ciałami, które oddziaływają także poza strefą kontaktu. W dalszej części przedstawiono modele dla płaskich powierzchni uwzględniające ich chropowatość. Opisano teorię Greenwooda i Williamsona GW, która zakłada, że wysokości nierówności mają rozkład gaussowski, a odkształcenie nierówności jest opisane modelem Hertza oraz teorie Greenwood i Tripp. Następnie zaprezentowano matematyczny opis odkształcania materiału przy jego kontakcie z wgłębnikiem w kształcie stożka przedstawiony przez Sneddona. W kolejnym rozdziale przedstawiono różne metody pomiaru twardości materiałów. Omówiono pomiar twardości metodą Brinella, Meyera, Vickersa, Knoopa, Martensa i Rockwella. Następny rozdział opisuje metodę indentacji. Przedstawiono w nim naprężenia i odkształcenia w materiale podczas penetracji przez kulisty i ostry wgłębnik, sposoby określania twardości i sztywności materiału, opisano efekt skali występujący dla małych przemieszczeń wgłębnika a także sposób wyznaczania gęstości dyslokacji występujących w materiale i ich mobilności. Rozdział ten opisuje także sposób wyznaczania współczynnika umocnienia odkształceniowego, krytycznego współczynnika intensywności naprężeń a także naprężeń własnych przy wykorzystaniu testu indentacji. W rozdziale tym zawarto również informacje o teście zarysowania. Ostatni rozdział przedstawia wyniki prac naukowych, w których autorka jest współautorem a także wyniki badań własnych jeszcze nieopublikowanych, które zostały uzyskane za pomocą indentera.